MULTICOMPONENT OPTIMAL CONTROL OF CONTAMINATION FLOWS IN POROUS MEDIA AND APPLICATIONS

KHAN ENAET HOSSAIN

A DISSERTATION SUBMITTED TO THE FACULTY OF GRADUATE STUDIES
IN PARTIAL FULFILMENT OF THE REQUIREMENTS
FOR THE DEGREE OF
DOCTOR OF PHILOSOPHY

GRADUATE PROGRAM IN MATHEMATICS AND STATISTICS
YORK UNIVERSITY
TORONTO, ONTARIO

May 2026

Abstract

In this thesis, we first develop a robust and efficient PDE-constrained optimal control model for nonlinear multicomponent contamination flows of groundwater in porous media. The proposed approach simultaneously integrates environmental and economic objectives. A splitting-based improved upwind finite difference scheme is proposed to discretize the governing nonlinear PDE system, ensuring stability and accuracy in the presence of advection and chemical reactions. The resulting high- dimensional PDE-constrained optimization problem is solved using a Differential Evolution algorithm. Numerical experiments on a rectangular geometric aquifer demonstrate the effectiveness of our model. Numerical investigation on more realistic aquifers further validate that the proposed model achieves significant contamination reduction while maintaining cost-effective remediation.

Next, we focus on the development of a parallel DE-PDE optimization control for multicomponent groundwater contamination systems. To efficiently solve the resulting high-dimensional optimization of contamination control, a parallel Differential Evolution (DE)-PDE algorithm is designed by distributing population evaluations across multiple processes on the Message Passing Interface (MPI) system, where the contaminant PDE algorithm is developed for solving the forward problems of advection-dominated contaminant flow on processors. Numerical experiments validate the developed parallel DE-PDE optimization algorithm and demonstrate its efficacy for solving the multicomponent contamination control. The parallel technique integrated with advanced numerical PDE methods is essential for achieving scalable, efficient,

and practical solutions to control multicomponent reactive transport contamination flow. Finally, we develop a multi-control strategy optimization framework for multicomponent Groundwater contamination management, designed to balance environmental performance with economic cost feasibility including the injection reduction cost at the boundary and the pumping control cost at wells. The objective function is proposed for three key components: concentration matching at observation locations, pollutant reduction at injection sites, and pumping-related operational costs at the wells. This multi-control framework provides efficient and practical remediation strategies for multicomponent contamination flows in porous media. Numerical experiments for multicomponent pollution flow on hypothetical rectangular and L-shaped aquifers show that the proposed multi-control framework plays a critical role in shaping optimal control strategies and improving remediation outcomes. Furthermore, implementation of the parallel DE PDE algorithm for the multi-control model significantly reduces computational time and improves convergence behaviour.

Acknowledgements

Acknowledgements

First and foremost, I would like to express my deepest gratitude to my supervisors, Professor Dong Liang and Associate Professor Hongmei Zhu, for their invaluable guidance, continuous support, and insightful discussions throughout my Ph.D. journey. Their expertise, patience, and encouragement have played a fundamental role in shaping this research and in helping me overcome numerous academic challenges. I feel truly fortunate to have had the opportunity to work under their mentorship.

I would also like to sincerely thank my Ph.D. committee members, Professor Michael Chen and Professor Xin Gao, for their constructive feedback, thoughtful suggestions, and valuable insights. Their comments have significantly contributed to improving the quality and depth of this work.

My heartfelt appreciation goes to my beloved wife, Ayesha Akter, for her unwavering support, understanding, and encouragement throughout this journey. Her patience and constant motivation have been a source of strength during the most challenging moments of my Ph.D.

I am deeply grateful to my parents for their unconditional love, sacrifices, and continuous prayers. Their belief in me has been the foundation of all my achievements. I would also like to thank my brother, sister-in-law, sisters and brothers-in-law for their encouragement, support, and constant inspiration. Their presence in my life has always provided me with strength and motivation.

Finally, I would like to acknowledge all friends, colleagues, and well-wishers who have supported me in various ways during my Ph.D. journey. Their encouragement and companionship have made this experience both meaningful and memorable.

Table of Contents

Abstract **ii**

Page

Abstract ii

Acknowledgements **iv**

Acknowledgements iv

Table of Contents **vi**

List of Tables **ix**

List of Figures **xiii**

1 Introduction **1**

1.1 Background and Literature Review 1

1.2 Research Contribution 7

2 Developing PDE-constrained Optimal Control of Multicomponent Contamination Flows in Porous Media **12**

2.1 Introduction 12

2.2 Mathematical Model of Multicomponent Pollution Control 13

2.2.1 Flow Equation 14

2.2.2 Multicomponent Concentration Transport Equations 15
2.2.3 Multicomponent Optimal Control Model 16
2.3 Discrete Multicomponent Optimal Control Model 19
2.3.1 Splitting Improved Upwind Scheme for Multicomponent Flow Equations 19
2.3.2 Discrete Multicomponent Optimal Control Model 24
2.3.3 Optimization Algorithm 24
2.4 Numerical Experiments 28

3 The Parallel DE-PDE Multicomponent Pollution Optimal Control Approach for Contamination Flows in Porous Media 48
3.1 Introduction 48
3.2 Mathematical Model of Multicomponent Pollution Optimal Control 49
3.2.1 Groundwater Flow and Multicomponent Transport Mathematical Model 50
3.2.2 Multicomponent Contamination Optimal Control Model 51
3.3 Discrete Multicomponent Pollution Optimal Control Model 55
3.3.1 Numerical Scheme for Governing Equations 55
3.3.2 Discrete Multicomponent Pollution Optimal Control Model 57
3.4 Parallel DE-PDE Algorithm for Multicomponent Contamination Control . . 58
3.4.1 MPI Parallel System 58
3.4.2 Parallel DE–PDE Optimization algorithm 59
3.5 Numerical Experiments 65

4 A Multi-Control Strategy Optimization Framework for Reactive Groundwater Contamination in Porous Media 97
4.1 Introduction 97
4.2 Mathematical Model of Multicomponent Pollution Control 98
4.2.1 Multicomponent Mathematical Model 98

4.2.2 Multi-control Strategy Optimal Control Model 100
4.3 Discrete Multicomponent Pollution Optimal Control Model 106
4.3.1 Numerical Scheme For Multicomponent Contamination Equations . . 106
4.3.2 Discrete Multicomponent Pollution Optimal Control Model 109
4.3.3 Parallel DE-PDE Multicomponent Optinization Implementation . . . 110
4.4 Numerical Experiments 110

5 Summery & Future work **146**

conclusion **146**

Bibliography **150**

List of Tables

2.1 Physical and chemical parameters used in the numerical simulations. 29

2.2 Numerical simulations-optimization results of Mg^{2+} and Cl^{-} when observation concentration at the lowest point of injection rates range for the objective function f_1. 38

2.3 Numerical simulations-optimization results of Mg^{2+} and Cl^{-} when observation concentration at the middle point of injection rates range for the objective function f_1. 39

2.4 Numerical simulations-optimization results of Mg^{2+} and Cl^{-} injection rates for different water heads for the objective function f_1. 41

2.5 Numerical simulations-optimization results of Mg^{2+} and Cl^{-} injection rates for different water heads for the objective function $f_1 + f_2$. 42

2.6 Numerical simulations-optimization results of Mg^{2+} and Cl^{-} injection rates for different noises for the objective function f_1. 43

2.7 Numerical simulations-optimization results of Mg^{2+} and Cl^{-} injection rates for different time for the objective function $f_1 + f_2$. 44

3.1 Paralle DE-PDE Performance Summary for the objective function f_1. . . . 67

3.2 Injected location case description. 71

3.3 Numerical simulations-optimization outcomes of Mg^{2+} and Cl^{-} injection rates across different locations for the objective function f_1 evaluated with 10 parallel processors. 71
3.4 The values of the cost function coefficients. 74
3.5 Paralle DE-PDE Performance Summary for the objective function $f_1 + f_2$. . 75
3.6 Numerical simulations-optimization results of Mg^{2+}, Ca^{2+} and Cl^{-} injection rates for different hydraulic heads for the objective function $f_1 + f_2$ evaluated with 10 parallel processors. 79
3.7 Numerical simulations-optimization results of Mg^{2+}, Ca^{2+} and Cl^{-} injection rates for different cost coefficient penalty for the objective function $f_1 + f_2$ evaluated with 10 parallel processors. 82
3.8 Numerical simulations-optimization results of Mg^{2+}, Ca^{2+} and Cl^{-} injection rates for different cost coefficient penalties for the objective function f_1,$f_1 + f_2$, and $f_1 + f_3$ evaluated with 10 parallel processors. 84
3.9 The case description. 87
3.10 Numerical simulations-optimization results of Mg^{2+}, Ca^{2+} and Cl^{-} injection rates for the objective function f_1 evaluated with 10 parallel processors. . . 88
3.11 Numerical simulations-optimization results of Mg^{2+}, Ca^{2+} and Cl^{-} injection rates for the objective function $f_1 + f_3$ evaluated with 10 parallel processors. 89

4.1 Physical and chemical parameters used in the numerical simulations. 114
4.2 Injection locations case description. 115
4.3 Numerical simulations-optimization results of Mg^{2+}, Ca^{2+} and Cl^{-} reduction rates for different injection location for the objective function f_1 evaluated with 10 parallel processors. 115
4.4 The values of the cost function coefficients. 117

4.5 Numerical simulations-optimization results of Mg^{2+}, Ca^{2+} and Cl^{-} reduction rates for extraction well locations for the objective function $f_1 + f_2$ evaluated with 10 parallel processors. 119
4.6 Numerical simulations-optimization results of Mg^{2+}, Ca^{2+} and Cl^{-} reduction rates for different hydraulic heads for the objective function $f_1 + f_2$ evaluated with 10 parallel processors. 121
4.7 Observation locations description. 124
4.8 Numerical optimization results of reduction rates for SO_4^{2-}, Na^{-}, Ca^{2+}, Fe^{3+} and Cl^{-} under different protected-zone configurations for the objective function f_1 evaluated with 10 parallel processors. 124
4.9 Observation locations description. 127
4.10 Optimal reduction rates of multicomponent ions SO_4^{2-}, Na^{-}, Ca^{2+}, Fe^{3+} and Cl^{-} for shallow and deep observation locations based on objective f_1 with 5 parallel processors. 127
4.11 Observation locations description. 128
4.12 Optimal reduction rates of multicomponent ions SO_4^{2-}, Na^{-}, Ca^{2+}, Fe^{3+} and Cl^{-} under different pumping-well configurations based on objective f_1 evaluated with 10 parallel processors. 128
4.13 Optimized injection rates of Na^{+},SO_4^{2-}, Ca^{-},Fe^{3+} and Cl^{-} for different objective functions f_1, $f_1 + f_2'$, and $f_1 + f_3$ evaluated with 10 parallel processors. 132
4.14 Optimal reduction rates of multicomponent ions Na^{+},SO_4^{2-}, Ca^{-},Fe^{3+} and Cl^{-} for varying left-boundary hydraulic heads based on objective f_1 evaluated with 10 parallel processors. 135
4.15 Pumping well locations description. 137

4.16 Numerical simulations-optimization results of ion reduction rates Na^{+},SO_4^{2-}, Ca^{-},Fe^{3+} and Cl^{-} for varying pumping-well locations using objective function $f_1 + f_3$ with 5 parallel processors. 138

List of Figures

2.1 The staggered mesh where • represents $(x_{i+\frac{1}{2}}, y_j)$ and ♦ represents (x_i, y_j), the nodes for $C_{\alpha,i+\frac{1}{2},j}$ and $H_{i,j}$ respectively. 20

2.2 The domain of aquifer. 30

2.3 Concentration profiles of contamination Cl^- with different component injection rates after 4^{rd}, 8^{th} and 14^{th} months respectively. 31

2.4 Concentration profiles of contamination Mg^{2+} for different component injection rates after 4^{rd}, 8^{th} and 14^{th} months respectively. 32

2.5 Concentration profiles of contamination CO_3^{2-} for different component injection rates after 4^{rd}, 8^{th} and 14^{th} months respectively. 33

2.6 Concentration profiles of contamination Cl^- due to the discontinuous injections at different time. 34

2.7 Concentration profiles of contamination Mg^{2+} due to the discontinuous injections at different time. 35

2.8 Concentration profiles of contamination CO_3^{2-} due to the discontinuous injections at different time. 37

2.9 The domain of aquifer for Example 3. 42

2.10 Concentration distributions of pollutant Cl^- at different time. Left column with maximum injection rates; Right column with optimal injection rates obtained by the optimal control approach. 45

2.11 Concentration distributions of pollutant Mg^{2+} at different time. Left column with maximum injection rates; Right column with optimal injection rates obtained by the optimal control approach. 47

3.1 Hypothetical rectangular vertical aquifer. 65
3.2 Parallel DE-PDE performance metrics: (a) Time reduction, (b) Speedup, and (c) Efficiency. 68
3.3 Parallel DE-PDE performance metrics: (a) Time reduction, (b) Speedup. . . 76
3.4 Hypothetical vertical aquifer. 86
3.5 Concentration distributions of Cl^{-} at different time: Left column with maximum injection rates; Right column with optimal injection rates 91
3.6 Concentration distributions of Mg^{2+} at different time: Left column with maximum injection rates; Right column with optimal injection rates 93
3.7 Concentration distributions of Ca^{2+} at different time: Left column with maximum injection rates; Right column with optimal injection rates 95

4.1 Hypothetical rectangular vertical aquifer. 111
4.2 Hypothetical L-Shape vertical aquifer. 134
4.3 Concentration distributions: Left column with minimum reduction rates and minimum pumping rate; Right column with optimal reduction rates and optimal pumping rate. 141
4.4 Concentration distributions at well locations: Left column with minimum reduction rates and minimum pumping rate; Right column with optimal reduction rates and optimal pumping rate. Horizontal part of graphs show the space in x-direction and vertical part represent time. 142

Chapter 1

Introduction

1.1 Background and Literature Review

Groundwater constitutes the largest accessible source of fresh water and plays a fundamental role in sustaining domestic, agricultural, and industrial activities worldwide. However, modern scientific studies indicate that many critical aquifers are experiencing severe depletion and contamination, leading to reduced streamflow, vegetation loss, drying of springs, declining groundwater levels, and land degradation [7, 18]. The primary drivers of groundwater contamination are anthropogenic activities, including industrial discharge, agricultural runoff, mining operation, and improper waste disposal, which introduce a wide range of pollutants into the subsurface environment [31, 120, 121]. As global population growth continues to increase the demand for freshwater resources, groundwater systems are subjected to escalating pressure, making their protection and sustainable management increasingly critical [34, 77]. A major challenge in groundwater management arises from the complex behaviour of contaminants within aquifer systems [60]. In realistic scenarios, pollutants rarely occur as single isolated species; instead, they exist as multiple interacting chemical components whose transport and transformation processes are strongly coupled through physical flow mechanisms and geochemical reactions [4, 10]. Once introduced into the subsurface, these contaminants

can persist for long periods due to the slow velocity of groundwater flow and the nonlinear interactions between advection, diffusion, dispersion, and chemical reactions [1, 80]. This multicomponent nature significantly increases the complexity of predicting contaminant migration and designing effective remediation strategies.

Groundwater flow and contaminant transport in porous media are commonly described using partial differential equation (PDE) models [32]. The flow field is typically governed by a parabolic PDE derived from mass conservation law and Darcy's law, which characterizes the movement of groundwater through the porous medium. Based on this flow field, contaminants transport is described by a set of convection–diffusion–reaction equations that account for advection, hydrodynamic dispersion, molecular diffusion, and chemical reactions [78, 103].

In realistic aquifer systems, contaminants rarely exist as single species; instead, they occur as multiple interacting components. These multicomponent systems involve complex chemical processes such as mineral dissolution–precipitation and intra-aqueous reactions, leading to strongly coupled and nonlinear transport behavior [111, 116]. As a result, the governing equations form a system of interconnected nonlinear PDEs that are significantly more challenging to analyze and simulate.

However, many traditional groundwater models rely on simplified assumptions, such as single-species transport or linearized dynamics, which fail to capture these nonlinear interactions and feedback mechanisms [22, 118]. To overcome these limitations, there is a growing need for advanced modeling frameworks that can simultaneously represent coupled flow, multicomponent reactive transport, and control processes such as pollutant injection and extraction [38, 79]. A comprehensive multicomponent groundwater contamination model integrates Darcy-based flow, multi-ion transport, and nonlinear reaction kinetics, while incorporating spatial heterogeneity and boundary-driven processes, providing a realistic and robust representation of aquifer systems [24, 87].

In many natural aquifer systems, chemical reactions rarely occur under instantaneous equi-

librium conditions; instead, they are often governed by kinetic mechanisms due to limited reactive surface area, heterogeneous flow fields, and finite residence times of chemical species [76]. Under such conditions, equilibrium-based models may lead to inaccurate predictions of contaminant behavior, particularly in regions with strong concentration gradients such as near injection or extraction wells. Kinetically controlled reaction models provide a more realistic representation of geochemical processes by explicitly accounting for reaction rates and transient chemical dynamics over time. In the context of multicomponent groundwater contamination, reactions are generally classified into geochemical equilibrium reactions [30, 50, 109] and kinetically controlled precipitation–dissolution processes [40, 43, 94]. Although the application of reactive transport modeling in watershed-scale studies remains relatively limited, it has proven to be a powerful framework for capturing the complex interplay between physical transport and nonlinear chemical reactions. The successful representation of such multicomponent reactive systems relies on the formulation of time-dependent, coupled nonlinear partial differential equations (PDEs) [28, 72, 91]. So a good groundwater model integrates groundwater flow governed by Darcy's law, multi-ion advection–dispersion transport, and nonlinear kinetic reactions describing mineral dissolution and precipitation, thereby providing a comprehensive and physically consistent framework for simulating contaminant transport and transformation in porous media.

In groundwater contamination management, the formulation of an appropriate objective function is a critical component of any optimization framework, as it defines the criteria by which remediation strategies are evaluated and compared [2]. Unlike forward simulation, which only predicts contaminant behavior, optimization requires a quantitative measure that links model outputs to management goals. An effective objective function must therefore capture both environmental performance and practical considerations, enabling the identification of control strategies that achieve desired outcomes under physical and operational constraints. The formulation of objective function that simultaneously captures environmental perfor-

mance and economic feasibility is essential in PDE-constrained groundwater contamination control problems [8, 53]. In this context, the concentration-matching component represents a fundamental measure of remediation effectiveness, as it quantifies the discrepancy between simulated contaminant concentrations obtained from the governing flow and transport equations and the desired or allowable observed concentration levels at monitoring locations. This component ensures that the designed control strategy satisfies environmental regulations and protects sensitive regions of the aquifer [52, 68]. However, focusing solely on concentration reduction often leads to unrealistic solutions that require excessively high treatment efforts. Achieving environmental protection goals in groundwater systems requires the identification of optimal contaminant management strategies that satisfy regulatory constraints while minimizing economic costs. This naturally leads to a PDE-constrained optimal control problem [17], in which both environmental and economic factors are integrated within a unified framework. To address the limitations of purely concentration-based objectives, a reduction or abatement cost component is incorporated to account for the operational expenses associated with pollutant removal at injection locations. This component reflects the practical reality that achieving higher levels of contaminant reduction typically requires more advanced treatment technologies and greater resource consumption, resulting in increased cost [63].

Accordingly, the objective function includes both an environmental penalty term, which quantifies concentration deviations at sensitive monitoring locations [95], and a flexible, piecewise-defined abatement cost function [23, 41] that captures technological thresholds, economic scaling effects, and nonlinear reduction penalties. The inclusion of this cost component introduces an essential trade-off between environmental objectives and economic feasibility, preventing overly aggressive control strategies and promoting balanced, realistic, and implementable solutions [29, 48].

Among available remediation techniques, groundwater pumping plays a key role in plume

containment by inducing hydraulic gradients and enhancing contaminant removal [6, 15]. In practical remediation systems, groundwater extraction through pumping wells is one of the most widely used techniques for plume containment and mass removal [54]. Pumping induces hydraulic gradients that alter flow patterns, enhance advective transport toward extraction wells, and reduce contaminant migration toward sensitive regions. However, pumping is energy-intensive and can become economically infeasible if used excessively [19, 84]. Therefore, incorporating pumping-related costs into the modeling framework is essential to ensure realistic and sustainable remediation strategies. This integrated approach enables a balance between contaminant reduction and operational efficiency, leading to practical and cost-effective groundwater management solutions [13, 96].

Therefore, modern groundwater management approaches increasingly emphasize the integration of economic considerations into physically based models [37, 92]. By incorporating energy and operational costs associated with pumping, it becomes possible to balance remediation performance with resource efficiency. This integrated perspective ensures that optimal strategies do not rely solely on aggressive hydraulic control but instead achieve a compromise between contaminant reduction and cost-effectiveness [81]. Such an approach is essential for developing sustainable and implementable groundwater remediation designs in real-world applications.

From a practical and computational perspective, numerical techniques play a fundamental role in solving the governing partial differential equations that describe groundwater flow and contaminant transport in porous media [25]. Among the available approaches, the finite difference method has been widely adopted due to its simplicity, efficiency, and suitability for discretizing convection–diffusion equations [21]. However, the coupled and multidimensional nature of groundwater flow and reactive transport models often leads to large-scale, high-dimensional systems that are computationally demanding to solve directly.

To address these challenges, operator splitting techniques have been developed as an effective

strategy for improving computational efficiency [55]. The splitting scheme decomposes the original multidimensional problem into a sequence of lower-dimensional subproblems, typically reducing a two-dimensional system into a set of one-dimensional problems that can be solved iteratively [59, 98]. This approach enables the use of fast and efficient one-dimensional solvers at each step, significantly reducing computational cost while maintaining numerical stability. In addition, the splitting framework can be combined with higher-order discretization schemes to enhance solution accuracy. In particular, the second-order improved upwind finite difference method is employed to discretize the transport equations [64, 118], effectively reducing numerical diffusion and preventing nonphysical oscillations that often arise in convection-dominated problems. The integration of operator splitting with improved upwind schemes, therefore, provides a robust and efficient numerical framework for simulating groundwater flow and multicomponent transport processes in porous media, ensuring both computational efficiency and high solution fidelity.

Various optimization methods have been applied to groundwater management problems, including gradient-based algorithms [69, 108], linear and nonlinear programming methods, and evolutionary algorithms [3, 16]. Gradient-based methods can be efficient when derivative information is available and the objective function is smooth, but they often struggle with nonconvex optimization landscapes and complex nonlinear constraints. Evolutionary algorithms, on the other hand, provide robust global optimization capabilities without requiring gradient information. Among these methods, the Differential Evolution (DE) algorithm has gained considerable attention due to its simplicity, strong global search capability, and effectiveness in solving nonlinear and high-dimensional optimization problems [88].

Despite these advantages, applying evolutionary algorithms to PDE-constrained groundwater optimization problems remains computationally expensive because each candidate solution requires a full numerical simulation of the groundwater flow and transport system [45]. For realistic aquifer models with fine spatial and temporal discretizations, this computational

cost can become prohibitive. Parallel computing offers an effective way to address this challenge by distributing the computational workload across multiple processors [36, 39]. Because evolutionary algorithms evaluate individuals in a population independently, they are particularly well suited for parallelization [33, 35]. The DE algorithm can be parallelized into subpopulation [20, 62, 104], into mutation strategy [56, 82] as well as parameter control [86, 115]. By combining parallel optimization techniques with efficient numerical solvers for the governing PDE system, it becomes possible to significantly reduce computational time while maintaining high solution accuracy.

1.2 Research Contribution

This thesis develops a comprehensive and scalable computational framework for multicomponent groundwater contamination control in porous media. The work integrates physically realistic PDE modelling of flow and reactive transport with advanced numerical methods, optimization techniques, and high-performance (HPC) computing. By combining accurate simulation, economically meaningful objective functions, and efficient parallel DE-PDE optimization strategies, the research addresses key challenges in modelling, computation, and practical implementation of groundwater remediation. The main contributions of this thesis are summarized as follows:

In the first part, we develop a robust and efficient PDE-constrained optimal control model for multicomponent groundwater contamination in porous media, designed to address the challenges of nonlinear reactive transport under realistic environmental conditions. We formulate a multicomponent optimal control model in which contaminant injection is applied along the upper boundary of the domain, and the corresponding injection rates are treated as control variables to be optimized. The model integrates groundwater flow governed by Darcy's law with multicomponent advection–dispersion–reaction transport equations, enabling the simulation of interacting chemical species within porous media. The model

incorporates nonlinear kinetic reactions, allowing for a realistic representation of mineral dissolution–precipitation processes and transient geochemical dynamics. The objective function consists of two primary components: the concentration-matching term f_1, which measures the discrepancy between simulated contaminant concentrations and observed contaminant concentrations at monitoring locations, and the abatement cost term f_2, which represents the operational cost associated with reducing contaminant levels at injection boundary locations. As a result, this optimization model provides a reliable foundation for analyzing multicomponent transport and designing efficient PDE-constrained groundwater optimal strategies. We introduce a splitting improved upwind finite difference scheme for the accurate and stable discretization of the governing multicomponent PDE system. The splitting technique separates the multidimensional problem into a sequence of lower-dimensional subproblems. This approach significantly reduces computational complexity and allows the use of efficient one-dimensional solvers at each step while preserving the coupling structure of the original system. To accurately resolve advection-dominated transport and avoid nonphysical oscillations, a second-order improved upwind finite difference method is employed for spatial discretization. Further, we integrate the proposed multicomponent PDE algorithm with a Differential Evolution (DE) algorithm to solve the resulting high-dimensional optimization control. The DE algorithm approach enables efficient global search and robust convergence, facilitating the identification of optimal control strategies under complex system dynamics. In the numerical experiments, we address the performance of multi-component contaminant transport problems involving the chemical reaction affection. We illustrate the impact of precipitation reaction. We then apply the PDE-constrained optimization framework to a hypothetical rectangular aquifer to find the optimal injection rates that minimize concentration deviation at observation sites and reduce the emission reduction costs. Finally, the linked simulation-optimization model is extended to a realistic aquifer with complex geometry as well as the discontinuous contamination at the injection rates. We

present the discontinuous optimal injection rates along with their respective reduction rates. Furthermore, we compare the concentration distribution contour with optimal injection rates and without optimal injection rates. This work has been published in [45].

In the second part, we develop a problem-specific parallel DE-PDE optimization algorithm for efficiently solving the computationally intensive optimization problem arising from multicomponent groundwater contamination control. The importance of this approach lies in the fact that each generation DE evaluation requires the numerical solution of a coupled nonlinear groundwater flow and multicomponent reactive transport system, making the optimization prohibitively expensive in a sequential setting, particularly for high-resolution discretizations and large populations. To address this challenge, the proposed parallel DE-PDE algorithm tightly integrates the DE and PDE algorithms in parallel and exploits its population-based structure by distributing candidate control variables, such as injection rates, across multiple processors over Message Passing Interface (MPI). Each processor independently evaluates a subset of candidate solutions by solving the governing PDE system, performing mutation, crossover, and selection operations, and computing the corresponding objective function values linked to concentration constraints and cost components. The updated parallel workers processor results are sent to the master processor. This customized parallelization preserves the robustness and global search capability of the DE-PDE system while significantly reducing computational time. In addition, we employ a stable and accurate PDE numerical solver to simulate multicomponent groundwater flow and contaminant transport in the DE-PDE approach. We consider the objective function to consist of the concentration-matching term f_1, and the piecewise-defined abatement cost function f_2'. A couple of numerical experiments validate the effectiveness of the parallel DE-PDE optimization algorithm for the multicomponent groundwater contamination control model. The first experiment demonstrates the performance of the parallel DE-PDE optimization algorithm by quantifying time reduction, speedup, and efficiency as functions of the number of CPUs for a three-component con-

tamination system governed by the concentration-matching objective f_1. In the subsequent experiment, we consider a four-component continuous contamination injection system in a hypothetical rectangular aquifer to investigate the influence of hydraulic head differences on optimal injection rates, while also analyzing the impact of varying penalty levels in the abatement cost function. The final example solved by the parallel DE-PDE optimization algorithm investigates a realistic aquifer with discontinuous top-boundary injection, highlighting the critical roles of injection placement, protected zones, and time-dependent control in achieving effective contamination reduction, while demonstrating clear advantages of optimal strategies over the maximum and optimal injection rates contamination contours.

In the third part, we develop a multi-control optimal strategy for multicomponent contamination problems. In particular, a pumping cost function f_3 is incorporated into the optimization framework to determine optimal pumping rates while accounting for the energy and operational costs of groundwater extraction. The resulting multi-control objective function integrates the concentration least squares error f_1, the piecewise abatement cost f_2' for determining optimal reduction rates, and the pumping cost f_3. Unlike conventional smooth cost formulations, the piecewise structure captures multiple treatment regimes and reflects technological thresholds, where different levels of reduction correspond to distinct cost behaviours. This combined formulation balances contaminant reduction with treatment and pumping efforts, preventing excessive reliance on energy-intensive pumping while maintaining effective control of groundwater contamination at injection locations. Furthermore, we implement a boundary treatment strategy formulated in terms of reduction rates at injection locations. The model regulates the concentration reduction at the boundary through reduction rates and pumping rates at extraction wells, which describes more realistic control strategies, while the multi-control optimization is subject to PDEs of groundwater flow and contaminant transport. To efficiently solve the resulting high-dimensional optimization model, the developed parallel DE-PDE algorithm is used for solving the multicomponent contamination multi-control

system. A sequence of numerical experiments is presented to evaluate the effectiveness of the proposed multi-control optimal strategy model. In the first experiment, we investigate the influence of reduction rates within a four-contaminant optimal control model, examining different injection locations and the effect of well placement on contaminant concentrations under the objectives f_1 and f_2'. In the next experiment, we examine more complex chemical reactions with six contaminant components, evaluating optimal reduction rates for small and large protected zones, comparing deep and shallow protection zones, and assessing the impact of optimal pumping rates on well placement. Finally, we analyze the combined impact of optimal reduction and pumping rates in an L-shaped aquifer under f_1, f_2', and f_3, accounting for varying hydraulic head conditions and pumping well locations, and assess performance by comparing worst-case and optimal strategies through contamination contours.

This thesis is organized as follows. Chapter 1 provides the background and a review of the relevant literature, and outlines the main research contributions of this work. In Chapter 2, we present the development of a PDE-constrained optimal control model for multicomponent contaminant transport in porous media. This chapter also introduces the proposed numerical solution strategy, where a splitting-based improved upwind finite difference method is employed for solving the governing PDE system, and a Differential Evolution algorithm is used to address the associated optimization problem. Numerical experiments are conducted to validate the accuracy and effectiveness of the proposed approach. In Chapter 3, we develop a problem-specific parallel DE–PDE optimization algorithm for multicomponent contamination control, which significantly enhances computational efficiency for solving the linked simulation–optimization model. In Chapter 4, we further develop the framework of the multi-control optimal strategy for multicomponent groundwater contamination management, incorporating more realistic control mechanisms and objective functions. Finally, Chapter 5 summarizes the main findings of the thesis and presents future research directions based on the insights gained from this study.

Chapter 2

Developing PDE-constrained Optimal Control of Multicomponent Contamination Flows in Porous Media

2.1 Introduction

Groundwater plays a vital role in water supply systems, but increasing population and industrial activities have led to serious contamination and depletion issues [61, 77, 112]. Understanding contaminant transport and developing effective control strategies are therefore essential [10, 102]. PDE-constrained simulation–optimization models provide a powerful framework for groundwater management by integrating physical processes with decision-making [12, 113]. These approaches have been applied to minimize contaminant concentrations and remediation costs [27, 118, 124]. However, most existing studies focus on single-contaminant flows. In multicomponent flows, the flow and transport processes are governed by coupled nonlinear PDEs involving advection, diffusion, and chemical reactions, leading to increased complexity [49, 89].

In this chapter, we develop a PDE-constrained optimal control model for multicomponent groundwater contamination flows in porous media. A novel multicomponent contamination optimization model is developed with a composite objective function balancing concentration matching and abatement cost by considering the pollution injected from the boundary. After that, we introduce a splitting improved upwind finite difference scheme to discrete the governing multicomponent PDE system. Then, we integrate PDE DE approach for efficiently solving the resulting high-dimensional optimization problem of multicomponent contamination control. Finally, a series of numerical experiments are conducted to evaluate the performance of the proposed control model. The numerical experiments begin by analyzing multicomponent contaminant transport in the presence of chemical reactions, with particular emphasis on the role of precipitation processes. The proposed PDE-constrained optimization model is subsequently implemented on a hypothetical rectangular aquifer to compute optimal injection rates that jointly reduce concentration deviation and abatement cost. The study is then extended to a more realistic aquifer characterized by complex geometry and discontinuous pollution at the injection locations. We numerically investigate the developed model by analyzing the flow simulation and identifying the optimal injection rates. The developed optimal control model is evaluated by comparing concentration distributions obtained with and without control, demonstrating the effectiveness of the proposed approach.

2.2 Mathematical Model of Multicomponent Pollution Control

We start to present the coupled system of nonlinear PDE equations that govern multicomponent contamination flows in porous media.

2.2.1 Flow Equation

The water head is usually described in terms of pressure as

$$h = \frac{P}{\rho g} + z, \tag{2.1}$$

where h is the water head $[L]$, P is the dynamic pressure $[ML^{-1}T^{-2}]$, while ρ is the fluid density $[ML^{-3}]$. Also, g is acceleration $[LT^{-2}]$ due to gravity, and z is the elevation $[L]$ above the datum. Where L represents the unit of length, M stands for the mass unit, and T represents the time unit.

The Darcy's law in porous media is given as [11, 40, 65],

$$\mathbf{u} = -K\left(\nabla h + \rho g \eta\right), \tag{2.2}$$

where $\mathbf{u}$ is the Darcy's velocity of the flow. K is hydraulic conductivity $[LT^{-1}]$, can be described by $K = \frac{k\rho g}{\mu}$, where k represents the permeability $[L^2]$, and μ represents the viscosity $[ML^{-1}T^{-1}]$ of the fluid. The variable η is used to indicate the direction of flow. When the flow is in a horizontal direction, η equals 0, and when the flow is in a vertical direction, η equals 1. The groundwater flow equation is given as

$$S_s \frac{\partial h}{\partial t} = \nabla.\left[K\left(\nabla h + \rho g \eta\right)\right], \tag{2.3}$$

where S_s is the specific storage $[L^{-1}]$.

2.2.2 Multicomponent Concentration Transport Equations

The equations of continuity refer to multi-component concentration transports. The multi-component transport equations can be expressed as follows [40, 65].

$$\frac{\partial(\phi c_\alpha)}{\partial t} + \nabla.\,(\mathbf{u}c_\alpha - D\nabla c_\alpha) = \mathbf{R}_\alpha(\mathbf{c}), \quad \alpha = 1, 2, \ldots, n_c, \tag{2.4}$$

where c_α is the concentration $[ML^{-3}]$ for α species, $\alpha = 1, 2, \ldots, n_c$, n_c is the number of species and $\mathbf{c} = (c_1, c_2, \ldots, c_{n_c})$. The diffusion is D. $\mathbf{R}_\alpha(\mathbf{c})$ is the multicomponent chemical reaction $[ML^{-3}T]$ that describes the mineral precipitation-dissolution reactions and the intra-aqueous reactions.

We consider horizontal flow within the aquifer. We introduce pollution rates at the top part boundary of the domain by the Neumann boundary condition; and there is no source or sink within the domain. Therefore, the coupled system of multi-component contamination flows can be expressed as follows

$$S_s\frac{\partial h}{\partial t} - \nabla.(K\nabla h) = 0, \tag{2.5}$$

$$\mathbf{u} = -K\nabla h, \tag{2.6}$$

$$\frac{\partial(\phi c_\alpha)}{\partial t} + \nabla.(\mathbf{u}c_\alpha - D\nabla c_\alpha) = \mathbf{R}_\alpha(\mathbf{c}), \quad \alpha = 1, 2, \ldots, n_c, \tag{2.7}$$

and the initial conditions are

$$h(x, y, 0) = h_0(x, y, 0), \quad (x, y) \in \Omega, \tag{2.8a}$$

$$c_\alpha(x, y, 0) = c_{\alpha_0}(x, y, 0), \quad \alpha = 1, 2, \ldots, n_c, \quad (x, y) \in \Omega, \tag{2.8b}$$

and the Dirichlet and Neumann boundary conditions for the water head are given as

$$h(a_x, y, t) = h_{left}(y, t), \quad h(b_x, y, t) = h_{right}(y, t), \tag{2.9a}$$

$$\frac{\partial h}{\partial y}(x,t) = 0, \quad (x,y) \in \text{the top and bottom boundaries of } \Omega. \tag{2.9b}$$

Let the first group of concentrations, c_β, $\beta = 1, 2, ..., n_e$, represents the concentrations of the existing components, and let the second group of concentrations, c_γ, $\gamma = n_e + 1, n_e + 2, ..., n_c$, represents the concentrations of the injected components. The boundary conditions of concentrations are given as

$$\frac{\partial c_\beta}{\partial x}(y,t) = 0, \quad \frac{\partial c_\beta}{\partial y}(x,t) = 0, \quad (x,y) \in \partial\Omega, \quad \beta = 1, 2, ..., n_e, \tag{2.10a}$$

$$\frac{\partial c_\gamma}{\partial y}(x,t) = -P_{\gamma_l}, on\ \Gamma_l, l = 1, 2, ..., n_s, \quad \frac{\partial c_\gamma}{\partial x} = 0, \frac{\partial c_\gamma}{\partial y} = 0, \quad \text{on} \quad \partial\Omega \backslash \cup\, \Gamma_l, \tag{2.10b}$$

where $\gamma = n_e+1, n_e+2, ..., n_c$. The Γ_l, where $l = 1, 2, ..., n_s$, represent the segments located on the upper part boundary of the domain where the pollutions are injected into the aquifer. P_{γ_l}, where $l = 1, 2, ..., n_s$, are the injection rates for the γ's pollutant on Γ_l. $\partial\Omega \backslash \cup\, \Gamma_l$ represents the rest boundary $\partial\Omega$ except $\cup\Gamma_l$.

2.2.3 Multicomponent Optimal Control Model

The goal of the mathematical model of optimal control of multicomponent contamination is to find optimal injection rates that can bring simulated concentrations as close as possible to the permissible environmental concentrations at the observation sites, while minimizing the abatement costs associated with contamination injections.

For a single-component contamination problem, a simulation-optimization model linking sewage disposal at injected wells and global purification costs was proposed for practical management purposes [8, 73, 124]. To achieve both environmental and economic benefits, it is possible to minimize single-species concentration deviations caused by pollution at well points while also reducing total emission abatement costs [118]. We consider the multicomponent optimal control model with the boundary injection treatment described as follows.

$$\min_{\{P_{\gamma_l}\}} f(\mathbf{P}_{\gamma_l}) = \min_{\{P_{\gamma_l}\}} \Big\{ \sum_{s=1}^{n_{ob}} \sum_{\gamma=n_e+1}^{n_c} \int_0^T \omega_{\gamma_s} \Big[c_{\gamma_s}(\mathbf{P}_{\gamma_l}, t) - c^*_{\gamma_s}(t) \Big]^2 dt + \sum_{l=1}^{n_s} \sum_{\gamma=n_e+1}^{n_c} \int_0^T \omega_2 A_{\gamma_l}(r_{\gamma_l}) dt \Big\} \tag{2.11}$$

subject to

$$\text{The governing system of PDEs:} \quad (2.5) - (2.10), \tag{2.12}$$

$$c^{min}_{\gamma_s} \le c_{\gamma_s} \le c^{max}_{\gamma_s}, \quad s = 1, 2, ..., n_{ob}, \ \gamma = n_e + 1, n_e + 2, ..., n_c, \tag{2.13}$$

$$P^{min}_{\gamma_l} \le P_{\gamma_l} \le P^{max}_{\gamma_l}, \quad l = 1, 2, ..., n_s, \ \gamma = n_e + 1, n_e + 2, ..., n_c, \tag{2.14}$$

where $\mathbf{P}_{\gamma_l} = \{P_{\gamma_l};\ l = 1, 2, ..., n_s,\ \gamma = n_e + 1, n_e + 2, ..., n_c\}$.

The objective function $f(\mathbf{P}_{\gamma_l})$ contains the overall fitness between the simulated concentration c_{γ_s} and the observed concentration $c^{ob}_{\gamma_s}$ and the abatement costs as follows

$$\begin{aligned} f(\mathbf{P}_{\gamma_l}) &= f_1(\mathbf{P}_{\gamma_l}) + f_2(\mathbf{P}_{\gamma_l}) \\ &= \sum_{s=1}^{n_{ob}} \sum_{\gamma=n_e+1}^{n_c} \int_0^T \omega_{\gamma_s} \Big[c_{\gamma_s}(\mathbf{P}_{\gamma_l}, t) - c^{ob}_{\gamma_s}(t) \Big]^2 dt + \sum_{l=1}^{n_s} \sum_{\gamma=n_e+1}^{n_c} \int_0^T \omega_2 A_{\gamma_l}(r_{\gamma_l}) dt. \end{aligned} \tag{2.15}$$

The first function, $f_1(\mathbf{P}_{\gamma_l})$, represents the concentration least squares error that defines the overall fitness between the simulated concentrations $c_{\gamma_s}(\mathbf{P}_{\gamma_l}, t)$ and the concentrations $c^{ob}_{\gamma_s}(t)$ at the observation sites with weight ω_{γ_s}. The allowable environmental concentrations $c^{ob}_{\gamma_s}(t)$ are perturbed from ideal concentration at minimum injection rates. The weight functions are designed to normalize the component affection in the objective function, which are defined as

$$\omega_{\gamma_s} = \frac{1}{\Big(c^{ob}_{\gamma_s} + \eta\Big)^2}, \tag{2.16}$$

where the constant η is dependent on the concentration values. It can be set to a sufficiently large value to prevent small differences in low concentrations from dominating the objective function.

The second function, $f_2(\mathbf{P}_{\gamma_l})$, refers to the reduction costs at all contaminated sites. $A_{\gamma_l}(r_{\gamma_l})$ represents the cost of reducing emissions on a daily basis at the l^{th} injected station during one unit period. This cost is calculated by

$$A_{\gamma_l}(r_{\gamma_l}) = b_{1,l} W_{\gamma_l}^{b_{2,l}} + b_{3,l} W_{\gamma_l}^{b_{2,l}} r_{\gamma_l}^{b_{4,l}}, \tag{2.17}$$

where the term of $b_{1,l} W_{\gamma_l}^{b_{2,l}}$ represents the power function of treatment volume at the l^{th} injected site and the total treated contamination volumes W_{γ_l} according to daily production activities are defined by

$$W_{\gamma_l} = P_{\gamma_l}^{max} \quad for \quad l = 1, 2, ..., n_s, \quad \gamma = n_e + 1, n_e + 2, ..., n_c, \tag{2.18}$$

and the influent rates, commonly known as reduction rates, are defined as

$$r_{\gamma_l} = \frac{P_{\gamma_l}^{max} - P_{\gamma_l}}{P_{\gamma_l}^{max}}, \ for \ l = 1, 2, ..., n_s, \quad \gamma = n_e + 1, n_e + 2, ..., n_c, \tag{2.19}$$

where $P_{\gamma_l}, \gamma = n_e + 1, n_e + 2, ..., n_c$, are the injected components injection rates.

The values of constant coefficients $b_{1,l}, b_{2,l}, b_{3,l}$ and $b_{4,l}$ at the l^{th} injection site are depended on industrial production activities. Here, $b_{1,l} > 0$ and $b_{3,l} > 0$ represent the coefficients of the cost function. The coefficient $b_{2,l}$ must be between zero and one, as it is subject to the scale economies effect. The $b_{4,l} > 1$ indicates the scale index of treatment efficiency where the cost increases exponentially with reduction rates.

Additionally, the concentrations simulated at observation sites, denoted as c_{γ_s}, always satisfy within a specific interval of concentrations during the simulation period. The injection rates P_{γ_l} are bounded by upper and lower values.

2.3 Discrete Multicomponent Optimal Control Model

In this section, we propose the discrete model of optimal control for the multicomponent contamination flows.

2.3.1 Splitting Improved Upwind Scheme for Multicomponent Flow Equations

Consider domain $\Omega = (a_x, b_x) \times (a_y, b_y)$. Let the mesh be $\Omega_h = I_h \times J_h$ with $I_h = \{a_x = x_0, x_1, ..., x_{n_x-1}, x_{n_x} = b_x\}$ and $J_h = \{a_y = y_{\frac{1}{2}}, y_1, ..., y_{n_y-1}, y_{n_y+\frac{1}{2}} = b_y\}$, where the spatial step size $\Delta x = \frac{b_x - a_x}{n_x}$ and $\Delta y = \frac{b_y - a_y}{n_y}$ along the x-direction and the y-direction, respectively. We denote in Fig. 2.1 that

$$x_i = a_x + i\Delta x, \quad i = 0, 1, 2, ..., n_x, \quad x_{i+\frac{1}{2}} = \frac{x_i + x_{i+1}}{2}, \quad i = 0, 1, 2, ..., n_x - 1,$$
$$y_j = a_y + j\Delta y, \quad j = 1, 2, 3, ..., n_y, \quad y_{j+\frac{1}{2}} = \frac{y_j + y_{j+1}}{2}, \quad j = 1, 2, 3, ..., n_y - 1.$$

Let N_t denote the number of the time steps and $\Delta t = \frac{T}{N_t}$. We define the time partition $0 = t^0 < t^1 < \ldots < t^{N_t-1} < t^{N_t} = T$ by $t^n = n\Delta t$.

We denote the approximate water-head by $H_{i,j}$ for $i = 1, 2, 3, ..., n_x - 1$ and $j = 1, 2, 3, ..., n_y$, the approximate velocity components in the x-direction by $U_{x_{i,j}}$, $i = 0, 1, 2, ..., n_x$ and $j = 1, 2, ..., n_y$ and in the y-direction by $U_{y_{i+\frac{1}{2}, j+\frac{1}{2}}}$ for $i = 0, 1, 2, ..., n_x - 1$ and $j = 0, 1, 2, ..., n_y$, and the approximate concentration by $C_{i+\frac{1}{2}, j}$ for $i = 0, 1, 2, ..., n_x - 1$ and $j = 1, 2, ..., n_y$, respectively.

We consider the modified upwind technique to approximate the convection and diffusion terms [58, 65], thereby avoiding nonphysical numerical oscillations.

Let $s(x)$ be the sign function given by

$$s(x) = \begin{cases} 1, & for \quad x \geq 0, \\ 0, & for \quad x < 0. \end{cases}$$

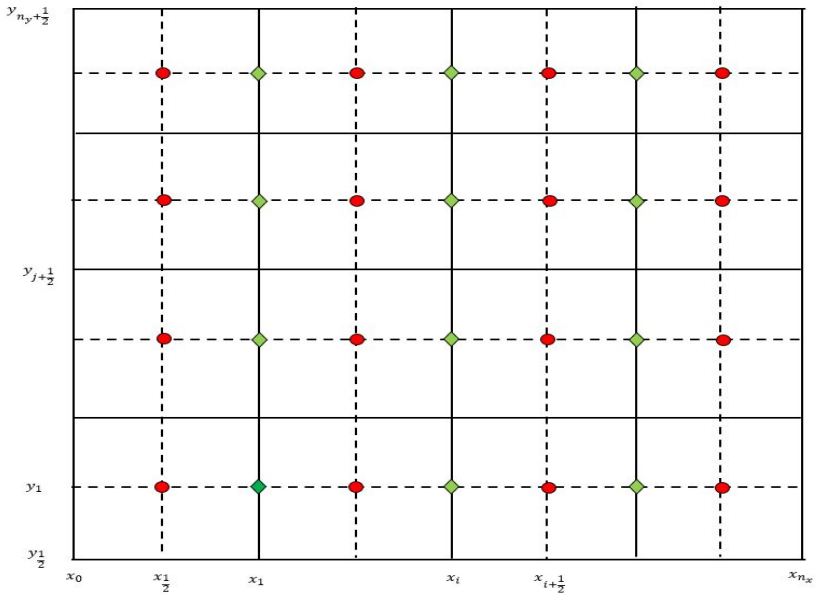

Figure 2.1: The staggered mesh where • represents $(x_{i+\frac{1}{2}}, y_j)$ and ♦ represents (x_i, y_j), the nodes for $C_{\alpha,i+\frac{1}{2},j}$ and $H_{i,j}$ respectively.

Let the global concentration fluxes be

$$z_\alpha = uc_\alpha - D\nabla c_\alpha, \ \alpha = 1, 2, \ldots, n_c. \tag{2.21}$$

Then, the approximate global concentration fluxes are defined by

$$\begin{aligned} Z^{x,n+\frac{1}{2}}_{\alpha_{i+1,j}} &= U^{n+1}_{x_{i+1,j}} \left[s\left(U^{n+1}_{x_{i+1,j}}\right) C^{n+\frac{1}{2}}_{\alpha_{i+\frac{1}{2},j}} + \left(1 - s\left(U^{n+1}_{x_{i+1,j}}\right)\right) C^{n+\frac{1}{2}}_{\alpha_{i+\frac{3}{2},j}} \right] \\ &\quad -D^*_{x_{i+\frac{1}{2},j}} \frac{C^{n+\frac{1}{2}}_{\alpha_{i+\frac{3}{2},j}} - C^{n+\frac{1}{2}}_{\alpha_{i+\frac{1}{2},j}}}{\Delta x}, i = 0, 1, ..., n_x - 1, j = 1, 2, ..., n_y. \qquad (2.22) \\ Z^{y,n+1}_{\alpha_{i+\frac{1}{2},j+\frac{1}{2}}} &= U^{x,n+1}_{y_{i+\frac{1}{2},j+\frac{1}{2}}} \left[s\left(U^{n+1}_{y_{i+\frac{1}{2},j+\frac{1}{2}}}\right) C^{n+1}_{\alpha_{i+\frac{1}{2},j}} + \left(1 - s\left(U^{n+1}_{y_{i+\frac{1}{2},j+\frac{1}{2}}}\right)\right) C^{n+1}_{\alpha_{i+\frac{3}{2},j+1}} \right] \end{aligned}$$

$$-D^*_{y_{i+\frac{1}{2},j+\frac{1}{2}}} \frac{C^{n+1}_{\alpha_{i+\frac{1}{2},j+1}} - C^{n+1}_{\alpha_{i+\frac{1}{2},j}}}{\Delta y}, i = 0, 1, ..., n_x - 1, j = 1, 2, ..., n_y. \quad (2.23)$$

with

$$D^*_{x_{i+\frac{1}{2},j}} = \frac{D_{x_{i+\frac{1}{2},j}}}{1 + \frac{|U^{n+1}_{x_{i+1,j}}|\Delta x}{2D_{x_{i+\frac{1}{2},j}}}}, \quad D^*_{y_{i+\frac{1}{2},j+\frac{1}{2}}} = \frac{D_{y_{i+\frac{1}{2},j+\frac{1}{2}}}}{1 + \frac{|U^{n+1}_{y_{i+\frac{1}{2},j+\frac{1}{2}}}|\Delta y}{2D_{y_{i+\frac{1}{2},j+\frac{1}{2}}}}}.$$

This improved upwind approximation avoids nonphysical numerical oscillations while keeping the second-order accuracy in the space step [58, 123, 125].

The splitting improved upwind finite difference scheme for the multicomponent contamination problem (2.5)-(2.10) is proposed as follows

For $n = 0, 1, ..., N_t - 1$, do

Step 1. To solve the water-head along the x-direction, for $j = 1, 2, ..., n_y$,

$$S_s \frac{H^{n+\frac{1}{2}}_{i,j} - H^n_{i,j}}{\Delta t} - \frac{1}{\Delta x}\left[K_{x_{i+\frac{1}{2},j}} \frac{H^{n+\frac{1}{2}}_{i+1,j} - H^{n+\frac{1}{2}}_{i,j}}{\Delta x} - K_{x_{i-\frac{1}{2},j}} \frac{H^{n+\frac{1}{2}}_{i,j} - H^{n+\frac{1}{2}}_{i-1,j}}{\Delta x}\right] = 0,$$
$$i = 1, 2, ..., n_x - 1, \quad (2.24)$$

with the Dirichlet boundary conditions

$$H^{n+\frac{1}{2}}_{0,j} = h_{left,j}, \quad H^{n+\frac{1}{2}}_{n_x,j} = h_{right,j}, \quad j = 1, 2, ..., n_y. \quad (2.25)$$

To solve the water-head along the y-direction, for $i = 1, 2, ..., n_x - 1$,

$$S_s \frac{H^{n+1}_{i,j} - H^{n+\frac{1}{2}}_{i,j}}{\Delta t} - \frac{1}{\Delta y}\left[K_{y_{i,j+\frac{1}{2}}} \frac{H^{n+1}_{i,j+1} - H^{n+1}_{i,j}}{\Delta y} - K_{y_{i,j-\frac{1}{2}}} \frac{H^{n+1}_{i,j} - H^{n+1}_{i,j-1}}{\Delta y}\right] = 0,$$
$$j = 1, 2, ..., n_y, \quad (2.26)$$

with the Neumann boundary conditions

$$\frac{H_{i,1}^{n+1}-H_{i,0}^{n+1}}{\Delta y}=0,\quad \frac{H_{i,n_y+1}^{n+1}-H_{i,n_y}^{n+1}}{\Delta y}=0,\quad i=1,2,...,n_x-1. \tag{2.27}$$

Step 2. To approximate the Darcy's velocity along the x-direction by, for $j=1,2,...,n_y$

$$U_{x_{i+1,j}}^{n+1}=-K_{x_{i+1,j}}\frac{H_{i+2,j}^{n+1}-H_{i,j}^{n+1}}{2\Delta x},\quad i=0,1,...,n_x-2, \tag{2.28}$$

and at the end points

$$U_{x_{0,j}}^{n+1}=-K_{x_{0,j}}\frac{H_{1,j}^{n+1}-H_{0,j}^{n+1}}{\Delta x},\qquad U_{x_{n_x,j}}^{n+1}=-K_{x_{n_x,j}}\frac{H_{n_x,j}^{n+1}-H_{n_x-1,j}^{n+1}}{\Delta x}. \tag{2.29}$$

To approximate the Darcy's velocity along the y-direction by, for $i=0,1,...,n_x-1$

$$U_{y_{i+\frac{1}{2},j+\frac{1}{2}}}^{n+1}=-K_{y_{i+\frac{1}{2},j+\frac{1}{2}}}\frac{H_{i+\frac{1}{2},j+1}^{n+1}-H_{i+\frac{1}{2},j}^{n+1}}{\Delta y},\quad j=1,2,...,n_y-1, \tag{2.30}$$

and at the end points

$$U_{y_{i+\frac{1}{2},\frac{1}{2}}}^{n+1}=-K_{y_{i+\frac{1}{2},\frac{1}{2}}}\frac{H_{i+\frac{1}{2},1}^{n+1}-H_{i+\frac{1}{2},0}^{n+1}}{\Delta y}, \tag{2.31}$$

$$U_{y_{i+\frac{1}{2},n_y+\frac{1}{2}}}^{n+1}=-K_{y_{i+\frac{1}{2},n_y+\frac{1}{2}}}\frac{H_{i+\frac{1}{2},n_y+1}^{n+1}-H_{i+\frac{1}{2},n_y}^{n+1}}{\Delta y}. \tag{2.32}$$

Step 3. To solve the concentrations along the x-direction by, for $j=1,2,...,n_y$,

$$\phi\frac{C_{\alpha_{i+\frac{1}{2},j}}^{n+\frac{1}{2}}-C_{\alpha_{i+\frac{1}{2},j}}^{n}}{\Delta t}+\frac{Z_{\alpha_{i+1,j}}^{x,n+\frac{1}{2}}-Z_{\alpha_{i,j}}^{x,n+\frac{1}{2}}}{\Delta x}=0,\quad i=0,1,...,n_x-1, \tag{2.33}$$

$$\begin{aligned}Z_{\alpha_{i+1,j}}^{x,n+\frac{1}{2}}=U_{x_{i+1,j}}^{n+1}&\left[s\left(U_{x_{i+1,j}}^{n+1}\right)C_{\alpha_{i+\frac{1}{2},j}}^{n+\frac{1}{2}}+\left(1-s\left(U_{x_{i+1,j}}^{n+1}\right)\right)C_{\alpha_{i+\frac{3}{2},j}}^{n+\frac{1}{2}}\right]\\&-D_{x_{i+\frac{1}{2},j}}^{*}\frac{C_{\alpha_{i+\frac{3}{2},j}}^{n+\frac{1}{2}}-C_{\alpha_{i+\frac{1}{2},j}}^{n+\frac{1}{2}}}{\Delta x},\end{aligned} \tag{2.34}$$

with the boundary conditions

$$\frac{C^{n+\frac{1}{2}}_{\alpha_{\frac{1}{2},j}} - C^{n+\frac{1}{2}}_{\alpha_{-\frac{1}{2},j}}}{\Delta x} = 0, \ \frac{C^{n+\frac{1}{2}}_{\alpha_{n_x+\frac{1}{2},j}} - C^{n+\frac{1}{2}}_{\alpha_{n_x-\frac{1}{2},j}}}{\Delta x} = 0, \quad j = 1, 2, ..., n_y. \tag{2.35}$$

To solve the concentrations along the y-direction by, for $i = 0, 1, ..., n_x - 1$

$$\phi \frac{C^{n+1}_{\alpha_{i+\frac{1}{2},j}} - C^{n+\frac{1}{2}}_{\alpha_{i+\frac{1}{2},j}}}{\Delta t} + \frac{Z^{y,n+1}_{\alpha_{i+\frac{1}{2},j+\frac{1}{2}}} - Z^{y,n+1}_{\alpha_{i+\frac{1}{2},j-\frac{1}{2}}}}{\Delta y} = R_\alpha\left(\mathbf{C}^{n+\frac{1}{2}}_{i+\frac{1}{2},j}\right), j = 1, 2, ..., n_y, \tag{2.36}$$

$$\begin{aligned} Z^{y,n+1}_{\alpha_{i+\frac{1}{2},j+\frac{1}{2}}} &= U^{n+1}_{y_{i+\frac{1}{2},j+\frac{1}{2}}} \left[s\left(U^{n+1}_{y_{i+\frac{1}{2},j+\frac{1}{2}}}\right) C^{n+1}_{\alpha_{i+\frac{1}{2},j}} + \left(1 - s\left(U^{n+1}_{y_{i+\frac{1}{2},j+\frac{1}{2}}}\right)\right) C^{n+1}_{\alpha_{i+\frac{1}{2},j+1}} \right] \\ &\quad - D^*_{y_{i+\frac{1}{2},j+\frac{1}{2}}} \frac{C^{n+1}_{\alpha_{i+\frac{1}{2},j+1}} - C^{n+1}_{\alpha_{i+\frac{1}{2},j}}}{\Delta y}, \end{aligned} \tag{2.37}$$

where

$$D^*_{x_{i+\frac{1}{2},j}} = \frac{D_{x_{i+\frac{1}{2},j}}}{1 + \frac{|U^{n+1}_{x_{i+1,j}}|\Delta x}{2D_{x_{i+\frac{1}{2},j}}}}, D^*_{y_{i+\frac{1}{2},j+\frac{1}{2}}} = \frac{D_{y_{i+\frac{1}{2},j+\frac{1}{2}}}}{1 + \frac{|U^{n+1}_{y_{i+\frac{1}{2},j+\frac{1}{2}}}|\Delta y}{2D_{y_{i+\frac{1}{2},j+\frac{1}{2}}}}},$$

and at the end points

$$\frac{C^{n+1}_{\alpha_{i+\frac{1}{2},1}} - C^{n+1}_{\alpha_{i+\frac{1}{2},0}}}{\Delta y} = 0, \quad i = 0, 1, ..., n_x - 1, \tag{2.38a}$$

$$\frac{C^{n+1}_{\beta_{i+\frac{1}{2},n_y+1}} - C^{n+1}_{\beta_{i+\frac{1}{2},n_y}}}{\Delta y} = 0, \quad \text{on} \quad \Gamma_l, \quad l = 1, 2, ..., n_s, \tag{2.38b}$$

$$\frac{C^{n+1}_{\gamma_{i+\frac{1}{2},n_y+1}} - C^{n+1}_{\gamma_{i+\frac{1}{2},n_y}}}{\Delta y} = -P_{\gamma_{i,j}}, \quad \text{on} \quad \Gamma_l, \quad l = 1, 2, ..., n_s, \tag{2.38c}$$

$$\frac{C^{n+1}_{\alpha_{i+\frac{1}{2},n_y+1}} - C^{n+1}_{\alpha_{i+\frac{1}{2},n_y}}}{\Delta y} = 0, \quad \text{on} \quad \{y = b_y\} \backslash \cup \Gamma_l. \tag{2.38d}$$

The initial values are defined as

$$H^0_{i,j} = h_0(i, j), \quad i = 1, 2, ..., n_x - 1, \quad j = 1, 2, ..., n_y, \tag{2.39a}$$

$$C^0_{\alpha_{i,j}} = c_{\alpha_0}(i, j), \quad i = 1, 2, ..., n_x, \quad j = 1, 2, ..., n_y. \tag{2.39b}$$

2.3.2 Discrete Multicomponent Optimal Control Model

To solve the multicomponent optimal control model (2.11) - (2.14) numerically, the discrete objective function can be approximated as

$$\begin{aligned} f_A\left(\mathbf{P}_{\gamma_l}\right) &= \sum_{s=1}^{n_{ob}} \sum_{\gamma=n_e+1}^{n_c} \sum_{n=1}^{N_t} \omega_{\gamma_s} \left[C_{\gamma_s}\left(\mathbf{P}_{\gamma_l}, t^n\right) - C_{\gamma_s}^{ob}(t^n)\right]^2 \Delta t \\ &\quad + \sum_{l=1}^{n_s} \sum_{\gamma=n_e+1}^{n_c} \sum_{n=1}^{N_t} \omega_2 A_{\gamma_l}\left(r_{\gamma_l}(t^n)\right) \Delta t. \end{aligned} \tag{2.40}$$

Thus the discrete multicomponent optimal control model is defined as finding the optimal P_{γ_l}, $\gamma = n_e + 1, n_e + 2, ..., n_c$, $l = 1, 2, ..., n_s$ such that

$$\min_{\{P_{\gamma_l}\}} f_A\left(\mathbf{P}_{\gamma_l}\right) \tag{2.41}$$

subject to

$$\text{The splitting improved upwind scheme of} \quad (2.24) - (2.39), \tag{2.42}$$

$$c_{\gamma_s}^{min} \le C_{\gamma_s}(t^n) \le c_{\gamma_s}^{max}, \quad \gamma = n_e + 1, n_e + 2, ..., n_c, \quad s = 1, 2, ..., n_{ob}, \tag{2.43}$$

$$P_{\gamma_l}^{min} \le P_{\gamma_l} \le P_{\gamma_l}^{max}, \quad \gamma = n_e + 1, n_e + 2, ..., n_c, \quad l = 1, 2, ..., n_s, \tag{2.44}$$

where $\{C_{\gamma_s}(t^n)\}$ are the numerical concentrations at the observation locations. The lower and upper bounds of concentrations at observation locations are denoted by $c_{\gamma_s}^{min}$ and $c_{\gamma_s}^{max}$. $\{C_{\gamma_s}^{ob}(t^n)\}$ are the allowable concentrations at the observation sites that are simulated at the smallest injection rates $P_{\gamma_l} = P_{\gamma_l}^{min}$.

2.3.3 Optimization Algorithm

We will apply the Differential Evolution (DE) algorithm to solve the discrete multicomponent optimal control model (2.40) - (2.44). The DE algorithm is a powerful population-based

optimization algorithm that is widely used to solve complex optimization problems. It is particularly well-suited for nonlinear and non-continuous problems with intricate search spaces. DE was first proposed in [97], which is composed of four distinct phases: initialization, mutation, crossover, and selection. With its effectiveness and flexibility, DE is an essential tool for optimization problems to obtain robust and assertive solutions.

The DE algorithm is a population-based stochastic evolutionary algorithm. (a) it is a derivative-free algorithm, which doesn't require to compute the gradient of objective function [106]. (b) it is a global optimal solution algorithm, which finds the global minimum, ignoring local minima. (c) it is straightforward to implement with a few control parameters [100]. The program is simple and is easy to use. (d) it has fast convergence. DE converges to the global minimum solution with good convergence property and outperforms many evolutionary algorithms in terms of convergence speed, as reported in [47, 67, 71, 127].

Here we present an extension of the DE algorithm to handle nonlinear constrained multicomponent optimal control problem of the objective function $f(\mathbf{P}_{\gamma_s})$.

Let $D = \left[\mathbf{P}_{\gamma_l}^{min}, \mathbf{P}_{\gamma_l}^{max}\right]$, then the restriction condition (2.43) can be rewritten as follows

$$f_{\gamma_s}^{n}(\mathbf{P}_{\gamma_l}) = C_{\gamma_s}^{n} - C_{\gamma_s}^{n,max} \leq 0, \quad s = 1, 2, ..., n_{ob}, \quad n = 1, 2, ..., N_t, \tag{2.45a}$$

$$f_{\gamma_s}^{N_t+n}(\mathbf{P}_{\gamma_l}) = C_{\gamma_s}^{n,min} - C_{\gamma_s}^{n} \leq 0, \quad s = 1, 2, ..., n_{ob}, \quad n = 1, 2, ..., N_t. \tag{2.45b}$$

For considering multiple-constraint optimal control problems of multicomponent, we have the following definitions and procedures, similar to [14, 42, 57, 88, 110, 117].

Definition 3.3.1 For the constrained optimization problem, we define the satisfaction function $\phi(\cdot)$: $D \to R$ by

$$\phi(\mathbf{P}_{\gamma_l}) = \sum_{n=1}^{N_t} \sum_{\gamma=n_e+1}^{n_c} \sum_{s=1}^{n_{ob}} \left(G_{\gamma_s}^{n} + G_{\gamma_s}^{N_t+n} \right), \tag{2.46}$$

where

$$G_{\gamma_s}^{n}(\mathbf{P}_{\gamma_l}) = \begin{cases} \frac{1}{2}, & f_{\gamma_s}^{n}(\mathbf{P}_{\gamma_l}) \leq 0, \\ \frac{1}{1+exp\left(f_{\gamma_s}^{n}(\mathbf{P}_{\gamma_l})\right)}, & otherwise, \end{cases} \tag{2.47a}$$

$$G_{\gamma_s}^{N_t+n}(\mathbf{P}_{\gamma_l}) = \begin{cases} \frac{1}{2}, & f_{\gamma_s}^{N_t+n}(\mathbf{P}_{\gamma_l}) \leq 0, \\ \frac{1}{1+exp\left(f_{\gamma_s}^{n}(\mathbf{P}_{\gamma_l})\right)}, & otherwise. \end{cases} \tag{2.47b}$$

Let, $S = \left\{\mathbf{P}_{\gamma_l} | \quad \mathbf{P}_{\gamma_l} \in D \wedge [f_{\gamma_s}^{n} \leq 0] \wedge [f_{\gamma_s}^{N_t+n} \leq 0]\right\}$. It's obvious that $\phi(\mathbf{P}_{\gamma_s}) = N_t(n_c - n_e)$ when $\mathbf{P}_{\gamma_l} \in S$ and $0 < \phi(\mathbf{P}_{\gamma_l}) < N_t(n_c - n_e)$ when $\mathbf{P}_{\gamma_l} \notin S$. The more of the constraint violation number of $\mathbf{P}_{\gamma_l}$, the less of the value of $\phi(\mathbf{P}_{\gamma_l})$.

Definition 3.3.2 Suppose $\mathbf{P}_{\gamma_l}$ and $\mathbf{Q}_{\gamma_l}$ are two different individuals from the next two generations, we define the following function

$$prior(\mathbf{P}_{\gamma_l}, \mathbf{Q}_{\gamma_l}) = \begin{cases} 1, & \phi(\mathbf{P}_{\gamma_l}) = \phi(\mathbf{Q}_{\gamma_l}) \text{ and } f(\mathbf{P}_{\gamma_l}) < f(\mathbf{Q}_{\gamma_l}) \text{ Or } \phi(\mathbf{P}_{\gamma_l}) > \phi(\mathbf{Q}_{\gamma_l}), \\ 0, & otherwise. \end{cases} \tag{2.48}$$

If the constraint violation number of $\mathbf{P}_{\gamma_l}$ > the constraint violation number of $\mathbf{Q}_{\gamma_l}$, that is $\phi(\mathbf{P}_{\gamma_l}) > \phi(\mathbf{Q}_{\gamma_l})$, we say that $\mathbf{P}_{\gamma_l}$ is prior to $\mathbf{Q}_{\gamma_l}$ and $prior(\mathbf{P}_{\gamma_l}, \mathbf{Q}_{\gamma_l}) = 1$. Where $f(\mathbf{P}_{\gamma_l})$ is the objective function.

The DE algorithm utilizes N_p D-dimensional parameter vectors $\mathbf{P}_{\gamma_{li,G}}^{j} = \left[\mathbf{P}_{\gamma_{li,G}}^{1}, \mathbf{P}_{\gamma_{li,G}}^{2}, ..., \mathbf{P}_{\gamma_{li,G}}^{D}\right]$, where $i = 1, 2, \ldots, N_p$ and $j = 1, 2, ..., D$, as a population for each generation G of the optimization process. The initialization is a one-time process while the other three phases are repeated until the termination criteria (maximum generation or reach tolerance) are satisfied. The initial population N_p by D dimensional matrix has been created using a uniformly distributed random variable within the range $[0, 1]$ and must be specified by maximum and minimum parameter bounds. For example, the initial value of j^{th} parameter

of the i^{th} vector at generation $G = 0$ is created as

$$\mathbf{P}^j_{\gamma_{l_{i,o}}} = \mathbf{P}^j_{\gamma_{l_L}} + \left(\mathbf{P}^j_{\gamma_{l_U}} - \mathbf{P}^j_{\gamma_{l_L}}\right) rand_j(0,1),\ i = 1, 2, ..., N_p \text{ and } j = 1, 2, ..., D, \tag{2.49}$$

where $\mathbf{P}^j_{\gamma_{l_U}}$ and $\mathbf{P}^j_{\gamma_{l_L}}$ are the maximum and minimum D-dimensional initialization vectors respectively and $rand_j(0,1)$ is uniformly distributed random variable within range $[0,1]$. Once initialized, the DE algorithm generates a mutant vector denoted by $\mathbf{Y}_{\gamma_{s_{i,G+1}}}$ following the mutation strategy. The mutation strategies are formulated with a base vector and weighted difference between two vectors. Generally, mutation strategies are labeled as $DE/a/b/c$, where a represents the target vector considered in the mutation procedure like $rand, best,$ or $rand - to - best$. The strategy with rand implies a random solution for perturbation, best used for perturbation the $\mathbf{P}_{\gamma_{l_{opt}}}$, and $rand - to - best$ implies a mix of both. The label b represents the number of difference vectors involved, either 1 or 2. The last label c usually doesn't show up in many authors' works, but it's important, c represents the crossover type. There are two types of crossover methods in the DE algorithm, one is binomial(bin) which takes the entries of the vector at random, and the second type is exponential (exp) selects a range of entries of the vector by starting at a random index.
We use the following strategy [97]

$$DE/rand - to - best/2/exp:$$
$$\mathbf{Y}_{\gamma_{l_{i,G+1}}} = \mathbf{P}_{\gamma_{l_{i,G}}} + \lambda\left(\mathbf{P}_{\gamma_{l_{opt,G}}} - \mathbf{P}_{\gamma_{l_{i,G}}}\right) + \mu\left(\mathbf{P}_{\gamma_{l_{1,G}}} - \mathbf{P}_{\gamma_{l_{2,G}}}\right), \tag{2.50}$$

where λ is a control parameter that further improves the quality of the greediness of the scheme by including the current optimal vector crossover phase. Trial vectors $\mathbf{U}^j_{\gamma_{l_{i,G+1}}}$ are produced in a probabilistic way by crossing mutant vectors $\mathbf{Y}_{\gamma_{l_{i,G+1}}}$, and target vectors $\mathbf{P}_{\gamma_{l_{i,G}}}$

as follows

$$\mathbf{U}^{j}_{\gamma_{l_{i,G+1}}} = \begin{cases} \mathbf{Y}^{j}_{\gamma_{l_{i,G+1}}}, & if \quad j = randb(j), \\ \mathbf{P}^{j}_{\gamma_{l_{i,G}}}, & if \quad j \neq randb(j). \end{cases} \tag{2.51}$$

To select the next generation vector, if the trail vector $\mathbf{U}^{j}_{\gamma_{l_{i,G+1}}}$ gives an equal or better objective value compared with the previous vector $\mathbf{P}^{j}_{\gamma_{l_{i,G}}}$ objective function value then trial vector is replaced the previous vector for next generation. It can be defined as following

$$\mathbf{P}^{j}_{\gamma_{l_{i,G+1}}} = \begin{cases} \mathbf{U}^{j}_{\gamma_{l_{i,G+1}}}, & if \quad prior\left(\mathbf{U}^{j}_{\gamma_{l_{i,G+1}}}, \mathbf{P}^{j}_{\gamma_{l_{i,G}}}\right) = 1, \\ \mathbf{P}^{j}_{\gamma_{;_{i,G}}}, & otherwise. \end{cases} \tag{2.52}$$

From the mutation stage to the selection stage procedure will continue until $G \leq G_{max}$ or the stop criteria are not satisfied.

DE is well-suited for global optimization problems, especially in high-dimensional spaces. One of the key factors that influence the exploration and exploitation capabilities of the Differential Evolution (DE) algorithm is its mutation strategy. To achieve a better balance between exploration and exploitation, we have opted to compare the performance of the seventh strategy from the traditional DE algorithm, which is denoted as "DE/rand-to-best/2/exp". Out of the ten available strategies, this particular one has been chosen for a comparative study to enhance the search behaviour of the algorithm. [107] used this strategy to select the best feature for predicting cardiovascular disease, which resulted in a model accuracy of 83%. For considering the adaptivity, some self-adaptive control parameter DE algorithms have been developed recently [14, 26].

2.4 Numerical Experiments

In this section, we will conduct numerical experiments to show the effectiveness of the multicomponent optimal control approach developed in the previous section. In the first

example, we will take numerical studies to assess the performance of the proposed splitting improved upwind numerical scheme that can efficiently model the transportation of three contaminants and their reactions with precipitation in porous media. This will help us gain valuable insights and a deeper understanding of the system dynamics. In the second example, our primary objective is to determine the optimal injection rates that minimize concentration errors at observation sites and reduce emission costs while using a rectangular aquifer. In these two examples, the pollutants are entering from the upper boundary of domains. In Example 3, we will consider a more realistic aquifer and further compute and analyze the multicomponent optimal control problems.

Table 2.1: Physical and chemical parameters used in the numerical simulations.

Parameter	**Symbol**	**Value**	**Unit**
Storage coefficient	S_s	10^{-5}	–
Effective porosity	ϕ	0.3	–
Hydraulic conductivity (x)	K_x	3.3	m/day
Hydraulic conductivity (y)	K_y	2.7	m/day
Diffusion coefficient (x)	D_x	8×10^{-2}	m^2/day
Diffusion coefficient (y)	D_y	3×10^{-2}	m^2/day
Reaction rate constant	k	0.04	mol m^{-2} day^{-1}
Effective surface area	S_e	0.049	m^{-1}

Example 1. In this experiment, we are assessing the performance of the multi-component contamination PDE problem for both continuous and discontinuous pollution injection processes. We consider three pollution components CO_3^{2-}, Mg^{2+} and Cl^- where the aquifer contains CO_3^{2-} inside and the other two components are injected on the specific top of the aquifer. The presence of multiple contaminants in a flow can greatly affect various chemical processes, including precipitation, complexation, dissolution, hydrolysis, oxidation-reduction, and more. We simulate the flow of multi-component contamination that occurs during the precipitation reaction.

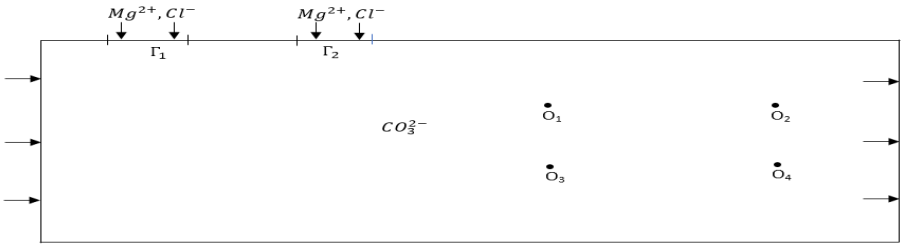

Figure 2.2: The domain of aquifer.

The stoichiometry equation for magnesite growth is as follows

$$CO_3^{2-} + Mg^{2+} \rightarrow MgCO_3.$$

The rate of growth for magnesium carbonate is $G_r = kS_eC_{Mg^{2+}}C_{CO_3^{2+}}$.
The kinetic control reaction for CO_3^{2-} is presented as $S_{CO_3^{2-}}G_r$, while that for Mg^{2+} is represented as $S_{Mg^{2+}}G_r$. The stoichiometric coefficients for the reaction involving CO_3^{2-} and Mg^{2+} are both equal to 1, denoted as $S_{CO_3^{2-}}G_r$ and $S_{Mg^{2+}}$. At a temperature of 25^0C, the solubility constant of $MgCO_3$ is 6.82×10^{-6}.
The Fig. 2.2 represents the domain of aquifer. We consider the domain of aquifer to be $L = 1000m$ horizontally and $M = 20m$ vertically. For the water head, we impose Dirichlet's boundary condition in the x-direction where left boundaries $h_{left} = 100m$ and right boundaries $h_{right} = 20m$ respectively, and the Neumann boundary condition $\frac{\partial h}{\partial y} = 0$ are considered on the top and bottom boundaries. For concentration, initially, water flow contains CO_3^{2-} contamination, and pollutions Mg^{2+} and Cl^- are injected on the top of the aquifer by imposing Neumann boundary condition.

We consider $\frac{\partial c}{\partial x} = 0$ on the left and right boundaries. The injected locations are placed between $[70m, 160m]$, and $[550m, 650m]$ respectively. Due to hydraulic head difference, an initial steady flow is produced from left to right.
For this experiment, we take the injection rates of two contaminants $Mg^{2+} = 0.009$ and $Cl^- = 0.05$ injected on the top of boundary $[70m, 160m]$ and $[550m, 650m]$ by imposing

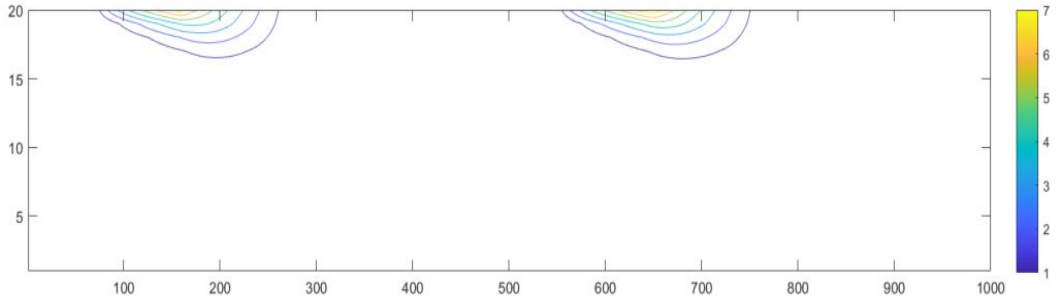

(a) at $t = 4$ months

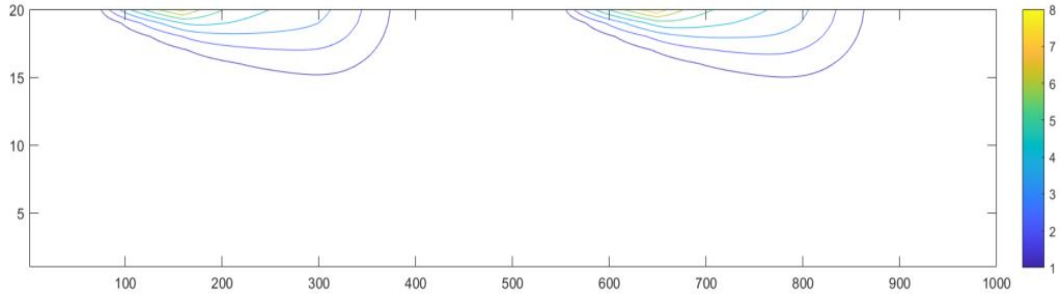

(b) at $t = 8$ months

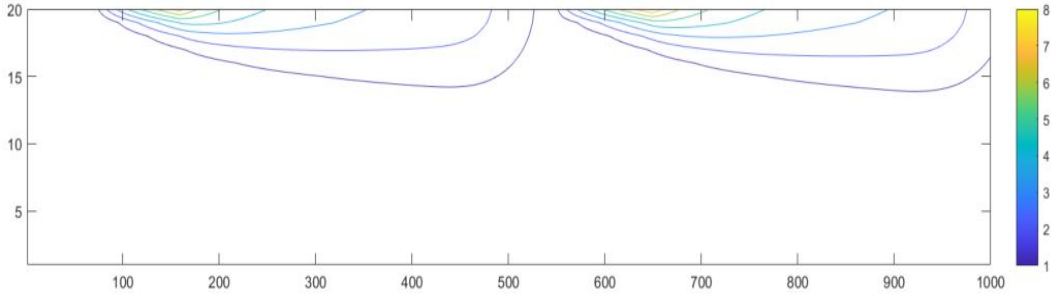

(c) at $t = 14$ months

Figure 2.3: Concentration profiles of contamination Cl^- with different component injection rates after 4^{rd}, 8^{th} and 14^{th} months respectively.

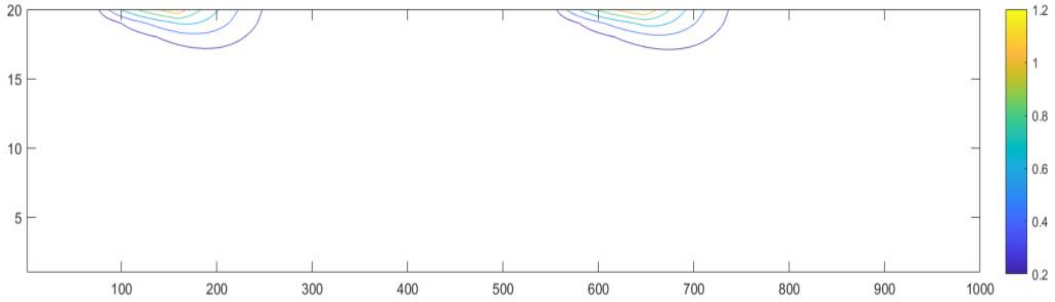

(a) at $t = 4$ months

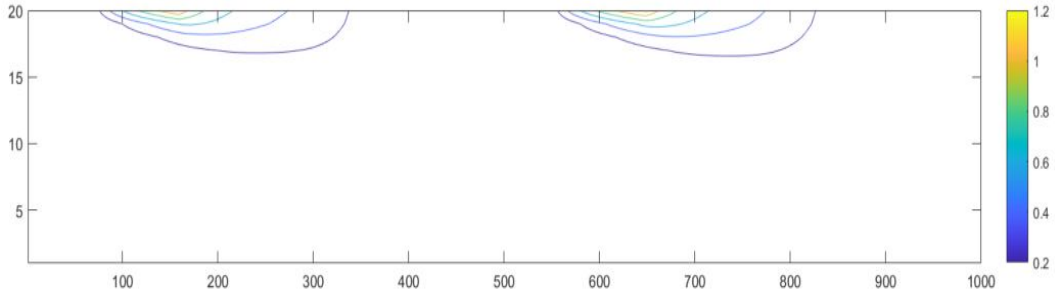

(b) at $t = 8$ months

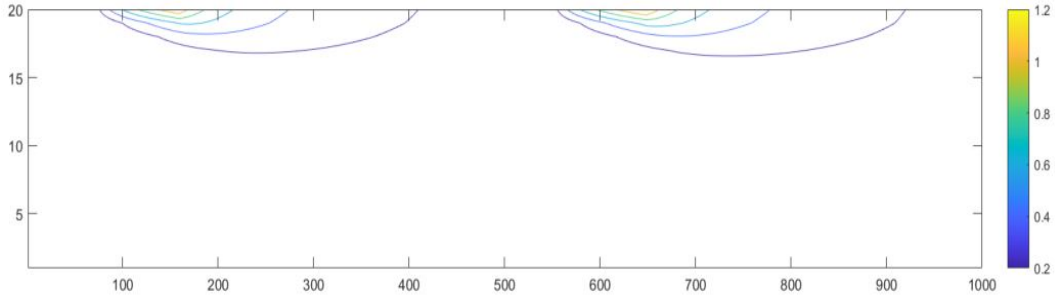

(c) at $t = 14$ months

Figure 2.4: Concentration profiles of contamination Mg^{2+} for different component injection rates after 4^{rd}, 8^{th} and 14^{th} months respectively.

Neumann boundary condition. The initial value of hydraulic head is $h_0 = 20m$. The initial concentration of CO_3^{2-} is $C_{CO_3^{2-}} = 0.67mol/m^3$, Mg^{2+} is $C_{Mg^{2+}} = 0$, and Cl^- is $C_{Cl^-} = 0$, respectively. The parameter values are listed in Table 2.1. We consider the spatial steps $\Delta x = \Delta y = 1m$ and the time step $\Delta t = 1day$. The total simulation time is 28 months. Firstly,

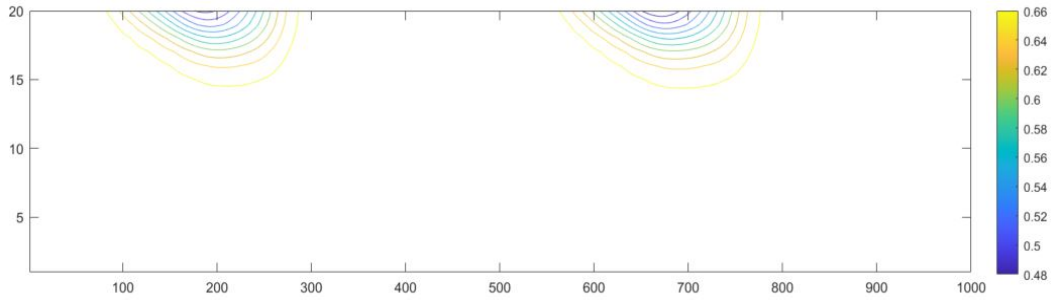

(a) at $t = 4$ months

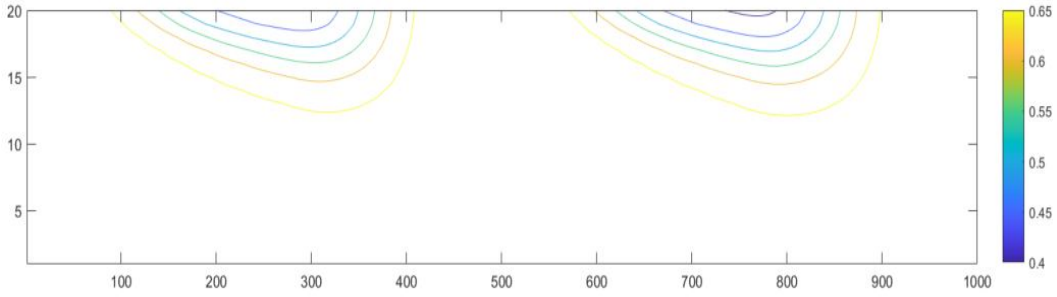

(b) at $t = 8$ months

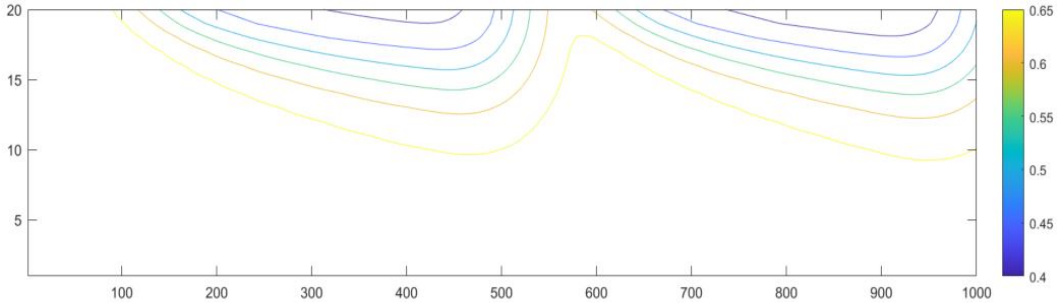

(c) at $t = 14$ months.

Figure 2.5: Concentration profiles of contamination CO_3^{2-} for different component injection rates after 4^{rd}, 8^{th} and 14^{th} months respectively.

we consider pollutions Cl^- and Mg^{2+} are injected continuously in two specific locations on the top of the boundary. Fig. 2.3 shows concentration profiles of Cl^- for 14 months. For different months, we can clearly observe that the Cl^- pollution moves from left to right

due to velocity which has been created by the water head difference. The Mg^{2+} pollution Fig. 2.4 also shows the same behaviour like Cl^{-}, but if we compare Fig. 2.4 and Fig. 2.3, Cl^{-} pollution moves fast than Mg^{2+} pollution since the precipitation reaction with CO_3^{2-} makes Mg^{2+} slow down. Concentration profiles of inside aquifer component CO_3^{2-} are shown in Fig. 2.5 where concentration moves left to right due to water head difference, and Fig. 2.5 (a)-(c) show that there is less concentration at injection locations because CO_3^{2-} is going to decrease due to the precipitation reaction with Mg^{2+}. Secondly, we will discuss a more

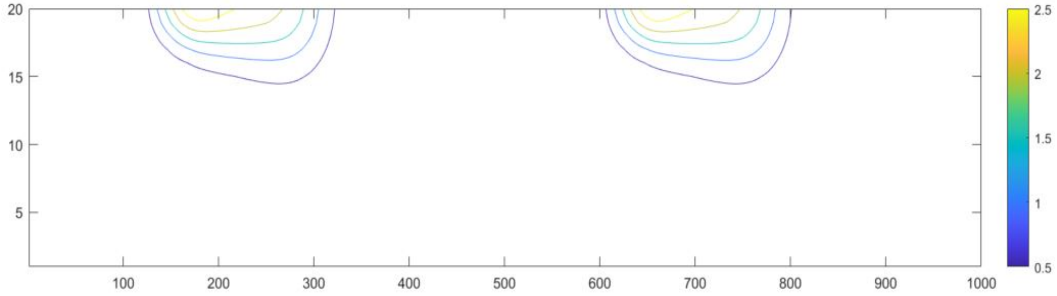

(a) at $t = 8$ months

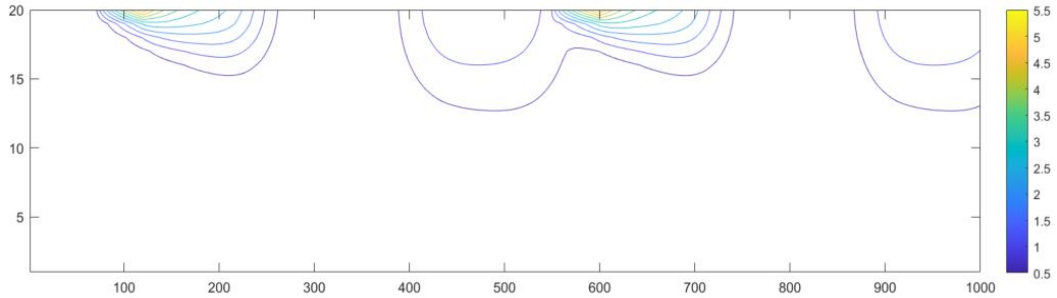

(b) at $t = 18$ months

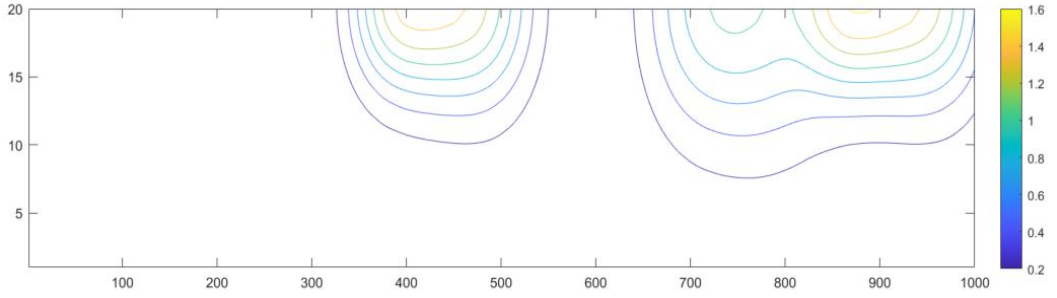

(c) at $t = 28$ months

Figure 2.6: Concentration profiles of contamination Cl^{-} due to the discontinuous injections at different time.

realistic situation that pollution sources do not release contamination continuously. We consider that the rates of injection for Mg^{2+} and Cl^{-} are introduced in six months and that there are be no further pollution injections in the next six months. From Fig. 2.6(a), the Cl^{-} contamination transports along the flow and the affection of diffusion is shown at the 8^{th} month. Then at the 12^{th} month, again, we re-inject the contamination rate on the top of the domain. Fig. 2.6(b) displays that there are new concentrations at the injected locations, and the big bubbles represent previous pollution moving with velocity and diffusion. Finally,

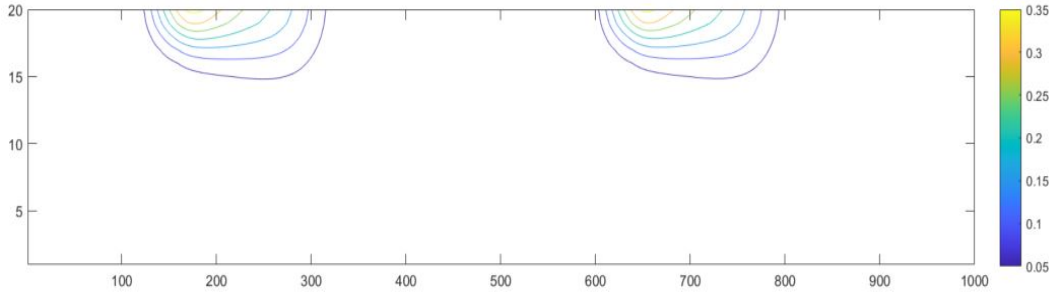

(a) at $t = 8$ months

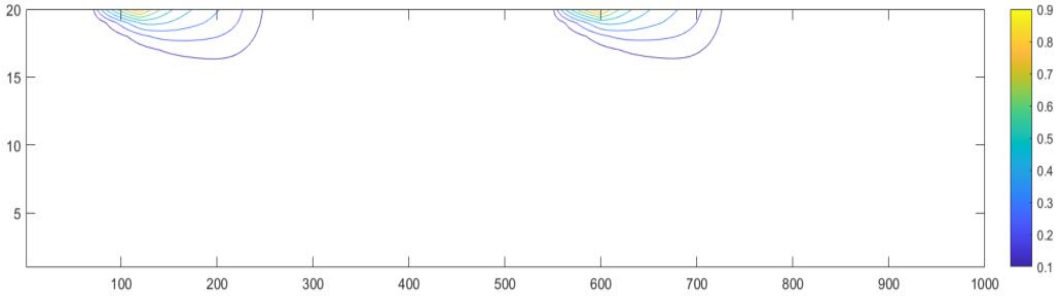

(b) at $t = 18$ months

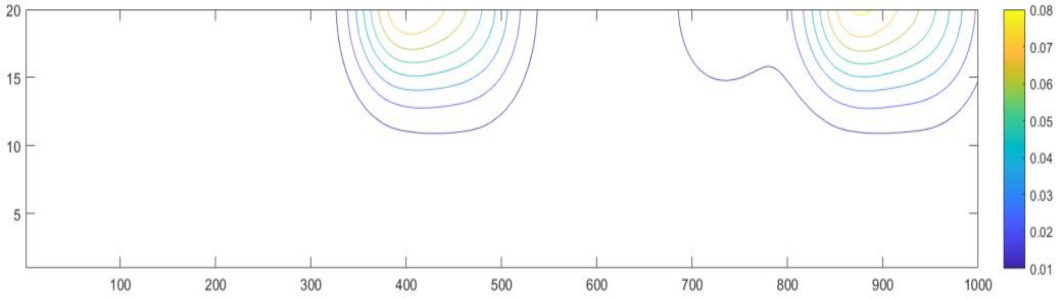

(c)at $t = 28$ months.

Figure 2.7: Concentration profiles of contamination Mg^{2+} due to the discontinuous injections at different time.

there is no injection rate after the 18^{th} month, and the pollution reaches the end of the right boundary at the 28^{th} month in Fig. 2.6(c). In Fig. 2.7(a) for Mg^{2+}, it shows the same behaviour of Mg^{2+} as in Fig. 2.6(a), but the scenarios are different at the 18^{th} month because Mg^{2+} concentration is depleted in the presence of CO_3^{2-} due to magnetic precipitation that shown in Fig. 2.7(b). At the end of 28^{th} month, Mg^{2+} pollution reaches the end of the right boundary with less concentration (see Fig. 2.7(c)). Fig. 2.8(a)-(c) show the concentration profiles of CO_3^{2-} and the results indicate that the concentration CO_3^{2-} will decrease due to its reaction with Mg^{2+}.

Example 2. In second experiment, we aim to find the optimal injection rates by the optimal control approach that minimizes the concentration deviation at the observation sites and the emission reduction at the injected pieces locations. We analyze the injection rates of two pollutants that are being injected at the four distinct pieces on the top boundary of the domain.

Consider the domain $\Omega = [0, 1000m] \times [0, 20m]$ and the total simulation time period of 2 years. In addition, we have a continuous pollution injection process that happens through the injected pieces at the top boundary of the domain. The left boundary value of water head is $h_{left} = 100m$ and the right boundary value of water head is $h_{right} = 20m$. The initial condition for water head is $h_0 = 20m$ as well as the initial value for pollution concentrations Mg^{2+}, Cl^- are zero and $CO_3^2 = 0.67mol/m^2$. We consider four injection rates P_{γ_l}, $l = 1, 2, 3, 4$, at the four injected pieces, and the four observation locations of $O_{n_{ob}}$, $n_{ob} = 1, 2, 3, 4$, inside the aquifer as shown in Fig. 2.2.

In the computation, the observation concentration $C_{\gamma_s}^{ob}$ is define by

$$C_{\gamma_s}^{ob} = C_{\gamma_s,min} + \zeta C_{\gamma_s,min} rand(.), \tag{2.53}$$

where $C_{\gamma_s,min}$ is the simulated concentration at the minimum injection rate, $rand(.)$ creates uniformly distributed random numbers in $(0, 1)$, and ζ is a fraction. The value of ζ varies

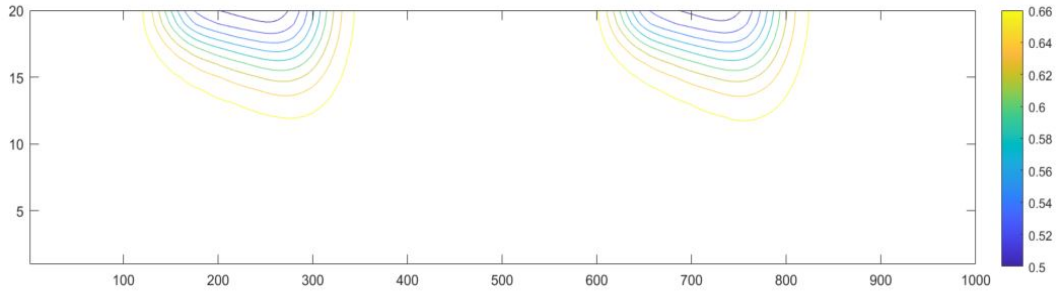

(a) at $t = 8$ months

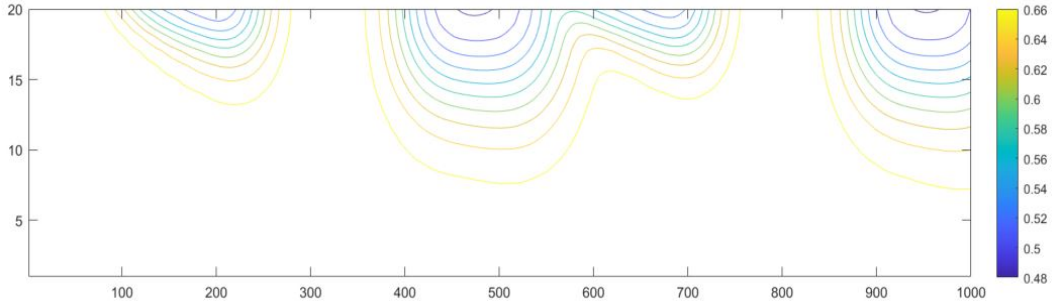

(b) at $t = 18$ months

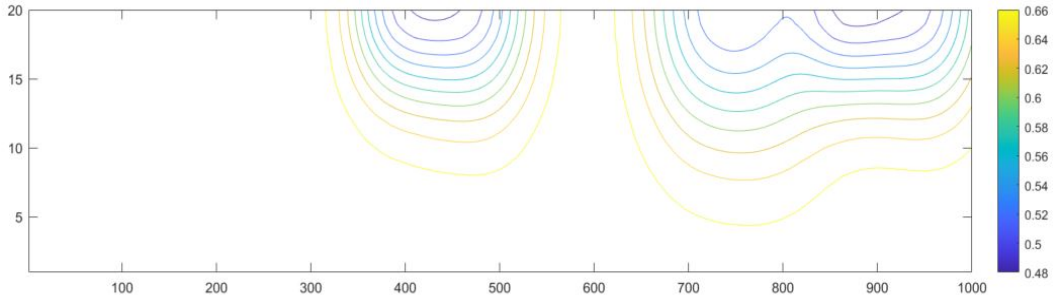

(c) at $t = 28$ months

Figure 2.8: Concentration profiles of contamination CO_3^{2-} due to the discontinuous injections at different time.

from 0.001 to 0.2, representing the noise level. For $\zeta < 0.10$ means low-level noise, between $0.1 < \zeta < 0.15$ corresponds to moderate noise level, and $\zeta > 0.15$ presents to high noise level. We consider the four injection locations on the top boundary of the left half domain. They are located between $[50m, 100m]$, $[170m, 220m]$, $[420m, 470m]$, and $[540m, 590m]$ respectively. Four discrete areas where the pollution concentrations are somewhat constrained need to be protected. In this instance, the particular places are considered as a few points which serve as observation locations. We consider the four observation points are $(410, 18.5)$, $(410, 18)$, $(850, 18.5)$ and $(850, 18)$. We use the spatial step sizes are $\Delta x = \Delta y = 1m$ and the time step size as $\Delta t = 1day$. The parameter values are given in Table 2.1.

The overall fitness function is defined as follows

$$f_1(\mathbf{P}_{\gamma_l}) = \sum_{s=1}^{n_{ob}} \sum_{\gamma=n_e+1}^{n_c} \sum_{n=1}^{N_t} \omega_{\gamma_s} [C_{\gamma_s}(\mathbf{P}_{\gamma_l}, t^n) - C^*_{\gamma_s}(t^n)]^2 \Delta t. \tag{2.54}$$

Table 2.2 and Table 2.3 show the accuracy of numerical results by the optimal control

Table 2.2: Numerical simulations-optimization results of Mg^{2+} and Cl^- when observation concentration at the lowest point of injection rates range for the objective function f_1.

	P_{γ_l}	AIR	$\zeta = 0$		$\zeta = 0.005$		$\zeta = 0.1$	
			Opt	Error	Opt	Error	Opt	Error
Mg^{2+}	P_{γ_1}	0.07	0.07	0	0.071072	$1.1e-3$	0.071224	$1.2e-3$
	P_{γ_2}	0.07	0.07	0	0.070951	$9.5e-4$	0.072278	$2.3e-3$
	P_{γ_3}	0.07	0.07	0	0.071046	$1.1e-3$	0.071223	$1.2e-3$
	P_{γ_4}	0.07	0.07	0	0.070979	$9.8e-4$	0.072135	$2.1e-3$
Cl^-	P_{γ_1}	0.08	0.08	0	0.081059	$1.1e-3$	0.081167	$1.2e-3$
	P_{γ_2}	0.08	0.08	0	0.080959	$9.6e-4$	0.082203	$2.2e-3$
	P_{γ_3}	0.08	0.08	0	0.081034	$1.0e-3$	0.081207	$1.2e-3$
	P_{γ_4}	0.08	0.08	0	0.080989	$9.9e-4$	0.082106	$2.1e-3$

approach. In Table 2.2 and Table 2.3, we consider only overall fitness f_1 as the objective function and present the results of different noise levels ζ. In the tables, AIR means the actual injection rates, and Opt means the numerical optimal injection rates. The relative

error indicates how good the measurement is relative to the object's size. We consider the injection rates range at four different injection locations $[0.07, 0.9]$ for Mg^{2+} and $[0.08, 0.9]$ for Cl^{-}. Then, we find the numerical optimal injection rates (Opt) at four different injection locations and find relative errors. In Table 2.2, we choose the minimum injection rates as

Table 2.3: Numerical simulations-optimization results of Mg^{2+} and Cl^{-} when observation concentration at the middle point of injection rates range for the objective function f_1.

	P_{γ_l}	AIR	$\zeta = 0$		$\zeta = 0.005$		$\zeta = 0.1$	
			Opt	Error	Opt	Error	Opt	Error
Mg^{2+}	P_{γ_1}	0.2	0.199261	$7.4e-4$	0.209822	$9.8e-3$	0.218743	$1.9e-2$
	P_{γ_2}	0.2	0.200092	$9.2e-5$	0.210055	$1.0e-2$	0.221054	$2.1e-2$
	P_{γ_3}	0.2	0.199177	$8.2e-4$	0.209974	$9.9e-3$	0.221686	$2.2e-2$
	P_{γ_4}	0.2	0.199900	$9.9e-5$	0.209949	$9.9e-3$	0.219137	$1.9e-2$
Cl^{-}	P_{γ_1}	0.3	0.299745	$2.6e-4$	0.309615	$9.6e-3$	0.317943	$1.8e-2$
	P_{γ_2}	0.3	0.299912	$8.8e-5$	0.310159	$1.0e-2$	0.321825	$2.2e-2$
	P_{γ_3}	0.3	0.298059	$1.9e-3$	0.309833	$9.8e-3$	0.322468	$2.2e-2$
	P_{γ_4}	0.3	0.301423	$1.4e-3$	0.309962	$9.9e-3$	0.318699	$1.9e-2$

AIR, *i.e.* 0.07 for Mg^{2+} and 0.08 for Cl^{-} for the observation solution. Here, we list results for $\zeta = 0$, $\zeta = 0.005$ and $\zeta = 0.1$. For $\zeta = 0$ *i.e.* no noise, we get the numerical optimal injection rates (Opt) same as the minimum injection rates at four injected locations as expected, and the relative errors are zero, which means there are no error for this case. After that, we add low level of noise $\zeta = 0.005$ in the observed simulation, and we get the numerical optimal injection rates for Mg^{2+} and Cl^{-} are slightly higher than the actual injection rates in the presence of the noise. The relative errors are 10^{-3}. The 8^{th} column of Table 2.2 presents the results of numerical optimal injection rates (Opt) for moderate noise level $\zeta = 0.1$. As we observe, the numerical optimal injection rates and the relative errors increase with the increase of noise.

In Table 2.3, we consider the AIR to be almost at the middle point of the injection rates range where the AIR for $Mg^{2+} = 0.2$ and $Cl^{-} = 0.3$. For $\zeta = 0.0$, the numerical optimal injection rates are very close to AIR at different injection locations, and the relative errors

are 10^{-4}. For Mg^{2+} and Cl^{-}, the numerical optimal injection rates at the four locations are slightly higher than AIR for adding slight noise $\zeta = 0.005$. The relative errors reach 10^{-3}. For the moderate noise level $\zeta = 0.1$, the numerical optimal injection rates are much higher than AIR, and the relative errors are higher than those with $\zeta = 0.005$. From Table 2.2 and Table 2.3, we observe that noise at the observation solution increases the numerical optimal injection rates. From the results, they reach small relative errors, which indicate that the numerical optimal injection rates by the optimal control approach are reasonable.

We then consider the joint affection of the overall fitness function and the abatement cost function. The abatement cost function is defined as follows

$$f_2(\mathbf{P}_{\gamma_l}) = \sum_{n=1}^{N_t} \sum_{l=1}^{n_s} \sum_{\gamma=n_e+1}^{n_c} \omega_2 [b_{1,l} W_{\gamma_l}^{b_{2,l}} + b_{3,l} W_{\gamma_l}^{b_{2,l}} r_{\gamma_l}^{b_{4,l}}(t^n)] \Delta t, \tag{2.55}$$

where the influent rates, commonly known as reduction rates(r-rate), are defined by

$$r_{\gamma_l} = \frac{P_{\gamma_l}^{max} - P_{\gamma_l}}{P_{\gamma_l}^{max}}. \tag{2.56}$$

The impact of velocity on the simulation-optimization model is discussed in Table 2.4 and Table 2.5. We calculate velocity in our model using the water head equation. The velocity is directly proportional to the difference between the two water head boundaries. As this difference increases, the velocity also increases. We consider the water flows from left to right. To observe the effect of velocity on optimal injection rates and reduction rates, we vary the left boundary values of water head from $100m$ to $300m$. However, the right water head boundary value remains constant at $h_{right} = 20m$. We use $\zeta = 0.005$ to perturb the observed concentration. We take different injection rate ranges in different injection locations. We consider the range of injection rate at the first location $[0.02, 0.9]$, second location $[0.05, 0.9]$, third location $[0.09, 0.9]$ and fourth location $[0.4, 0.9]$ for Mg^{2+}. On the other hand, the first location $[0.03, 0.9]$, second location $[0.07, 0.9]$, third location $[0.1, 0.9]$ and fourth location

$[0.5, 0.9]$ for Cl^-. At the specific injection location, we use the AIR as the minimum injection rate. We choose and noise level $\zeta = 0.005$. In Table 2.4, we have selected the objective

Table 2.4: Numerical simulations-optimization results of Mg^{2+} and Cl^- injection rates for different water heads for the objective function f_1.

	P_{γ_l}	AIR	$h = 100m$		$h = 200m$		$h = 300m$	
			Opt	r-rate (%)	Opt	r-rate (%)	Opt	r-rate (%)
Mg^{2+}	P_{γ_1}	0.02	0.02107	97.66	0.02101	97.67	0.02268	97.48
	P_{γ_2}	0.05	0.05096	94.34	0.05144	94.28	0.05000	94.44
	P_{γ_3}	0.09	0.09546	89.39	0.11101	87.67	0.11319	87.42
	P_{γ_4}	0.40	0.40711	54.77	0.40347	54.17	0.40000	55.56
Cl^-	P_{γ_1}	0.03	0.03106	96.55	0.03099	96.56	0.03306	96.33
	P_{γ_2}	0.07	0.07094	92.12	0.07240	91.96	0.07000	92.22
	P_{γ_3}	0.10	0.10541	88.29	0.12075	86.58	0.14069	84.44
	P_{γ_4}	0.50	0.51305	42.99	0.50278	44.13	0.50000	44.44

function that incorporates the overall fitness f_1. This table shows the cases the influence of varying water head values. We take different injection rate ranges in different injection locations. In the table, r-rate means the reduction rates. According to the data presented in Table 2.4, it is observed that the numerical optimal injection rates (Opt) are nearly identical to the actual injection rates at four distinct injection sites for both Mg^{2+} and Cl^-. The reduction rates increase for a wide range of injection rates and then gradually decrease as the injection rate range narrows.

Table 2.5 shows a similar experiment by considering the joint objective function of the overall fitness f_1 and the deduction cost f_2. The values of the coefficients for the f_2 function are as follows: $b_1 = 1.7945$, $b_2 = 0.5733$, $b_3 = 2.9275$, and $b_4 = 3.7391$. Additionally, the weight ω_2 is equal to 100. As the value of the left head boundary increases, it is clear that the flow velocity of the pollutant also increases, resulting in an overall decrease in the emission reduction rate. From Table 2.5, it can be observed that the optimal injection rates rise as the water head increases while the reduction rate decreases. The locations of P_{γ_1} and P_{γ_2} have undergone significant changes. But at P_{γ_4}, the optimal injection rate is identical to AIR

Table 2.5: Numerical simulations-optimization results of Mg^{2+} and Cl^{-} injection rates for different water heads for the objective function $f_1 + f_2$.

	P_{γ_l}	AIR	$h = 100m$		$h = 200m$		$h = 300m$	
			Opt	r-rate (%)	Opt	r-rate (%)	Opt	r-rate (%)
Mg^{2+}	P_{γ_1}	0.02	0.25920	71.20	0.29008	67.77	0.36312	59.65
	P_{γ_2}	0.05	0.18968	78.92	0.26873	70.14	0.35900	60.11
	P_{γ_3}	0.09	0.41402	53.99	0.38114	57.65	0.43468	51.70
	P_{γ_4}	0.40	0.40000	55.56	0.40000	55.56	0.40000	55.56
Cl^{-}	P_{γ_1}	0.03	0.26623	70.42	0.29117	67.65	0.36037	59.96
	P_{γ_2}	0.07	0.19724	78.08	0.27074	69.92	0.35796	60.23
	P_{γ_3}	0.10	0.41787	53.57	0.38738	56.96	0.43873	51.25
	P_{γ_4}	0.50	0.50000	44.44	0.50000	44.44	0.50000	44.44

because the injection rate range is small. Based on the result, the flow velocity impacts the injection rate and has a more significant impact on the upstream injection locations.

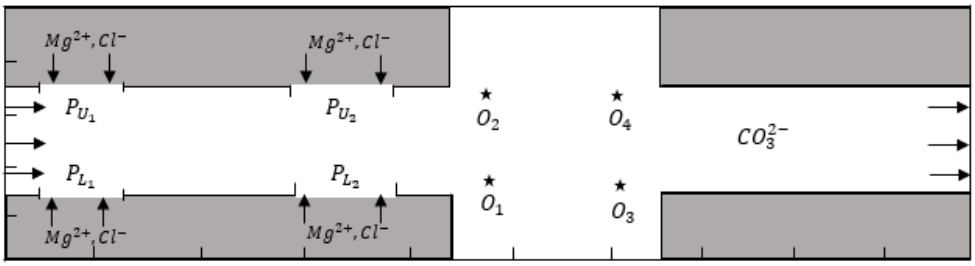

Figure 2.9: The domain of aquifer for Example 3.

Example 3. For the experiment, we evaluate the performance of multicomponent contamination problem with a discontinuous pollution injection process on the specific location of more realistic domain. A more realistic aquifer with irregular geometry is shown in Fig. 2.9 over a large domain with the dimensions of the aquifer to be $L = 1000m$ horizontally and $M = 50m$ vertically, respectively. We have divided the domain into two channels that are $20m$ wide each. The first channel stretches from the left side of the domain up to $450m$, while the second channel is located between $650m$ and $1000m$. However, in the middle of the domain, between $450m$ and $650m$, the width is extended to $50m$. For the water head, we impose Dirichlet's boundary condition in the x-direction where the left boundary value

is $h_{left} = 150m$ and the right boundary value $h_{right} = 50m$ respectively, and the Neumann boundary condition $\frac{\partial h}{\partial y} = 0$ is considered on the top and bottom boundaries of the domain. For the concentrations, initially, the flow contains CO_3^{2-} contamination, and on the specific location of the aquifer, there is four pieces where we inject Mg^{2+} and Cl^- pollutions by imposing Neumann boundary condition with injection rate. We consider $\frac{\partial c_\alpha}{\partial x} = 0$ on the left and right boundaries. Except on the injection pieces, we assume $\frac{\partial c_\alpha}{\partial y} = 0$ at the top and bottom boundaries. Due to hydraulic head difference, an initial steady flow travels from left to right.

Table 2.6: Numerical simulations-optimization results of Mg^{2+} and Cl^- injection rates for different noises for the objective function f_1.

	Month		$\zeta = 0$				$\zeta = 0.2$			
			P_{L_1}	P_{L_2}	P_{U_1}	P_{U_2}	P_{L_1}	P_{L_2}	P_{U_1}	P_{U_2}
Mg^{2+}	1^{st}	Opt	0.1078	0.1129	0.1194	0.1130	0.1408	0.1236	0.1408	0.1236
		r-rate	84.6%	83.9%	82.9%	83.9%	79.8%	82.4%	79.8%	82.3%
	2^{nd}	Opt	0.1521	0.1693	0.1790	0.1696	0.1952	0.1794	0.2012	0.1704
		r-rate	78.3%	75.8%	74.4%	75.8%	72.1%	74.4%	71.3%	75.7%
	3^{rd}	Opt	0.2189	0.1975	0.2089	0.1978	0.2584	0.2260	0.2514	0.2288
		r-rate	68.7%	71.9%	70.2%	71.7%	63.1%	67.7%	64.0%	67.3%
Cl^-	1^{st}	Opt	0.1541	0.1411	0.1492	0.1413	0.1910	0.1816	0.1909	0.1820
		r-rate	80.7%	82.4	81.4%	82.3%	76.1%	77.3%	76.1%	77.2%
	2^{nd}	Opt	0.2089	0.1975	0.2049	0.1978	0.2414	0.2280	0.2414	0.2288
		r-rate	73.9%	75.3%	74.4%	75.3%	69.8%	71.5%	69.8%	71.4%
	3^{rd}	Opt	0.2357	0.2258	0.2386	0.2260	0.2716	0.2599	0.2715	0.2602
		r-rate	70.5%	71.8%	70.2%	71.7%	66.1%	67.5%	66.1%	67.5%

We take four injection pieces, which are placed in x-direction $P_{L_1} = [70m, 200m]$, $P_{L_2} = [270m, 400m]$ at $y = 15m$ and $P_{U_1} = [70m, 200m]$, $P_{U_2} = [270m, 400m]$ at $y = 35m$. We consider four observation points at $O_1 = (470, 20)$, $O_2 = (470, 30)$, $O_3 = (620, 20)$ and $O_4 = (620, 30)$. Table 2.6 exclusively focuses on overall fitness f_1 as the objective function and shows the outcomes of various noise levels ζ. In the table, r-rate means the reduction rates and Opt means the optimal injection rates. We consider the injection rates range at four different injection locations $[0.05, 0.7]$ for Mg^{2+} and $[0.06, 0.8]$ for Cl^-. We obtain the

Table 2.7: Numerical simulations-optimization results of Mg^{2+} and Cl^- injection rates for different time for the objective function $f_1 + f_2$.

	P	1^{st} month		2^{nd} month		3^{rd} month	
		Opt	r-rate (%)	Opt	r-rate (%)	Opt	r-rate (%)
Mg^{2+}	P_{L_1}	0.32699	59.12%	0.44548	44.56%	0.57472	28.16%
	P_{L_2}	0.30289	62.14%	0.39433	50.71%	0.46005	42.49%
	P_{U_1}	0.35422	55.72%	0.48633	39.21%	0.56738	29.08%
	P_{U_2}	0.30992	61.26%	0.40488	49.39%	0.47236	40.96%
Cl^-	P_{L_1}	0.42623	52.64%	0.55472	38.36%	0.63397	29.56%
	P_{L_2}	0.40861	55.00%	0.46005	48.88%	0.52577	41.58%
	P_{U_1}	0.41527	53.86%	0.56738	36.96%	0.64844	27.95%
	P_{U_2}	0.40740	54.73%	0.47236	47.52%	0.53984	40.02%

observation solution with the injection rates of 0.1. For $\zeta = 0$, *i.e.* no noise, we get the optimal injection rates very close to the actual injection rates at four injected piceces as expected, and the r-rates are higher. After that, we added noise level of $\zeta = 0.2$ in the observed simulation, and we get the optimal injection rates for Mg^{2+} and Cl^- are higher than the actual injection rates due to adding noise. we also observe that injection rates are increasing for the three stress periods. Here, P_{L_1} and P_{U_1} are at the upstream locations and P_{L_2} and P_{U_2} are at the downstream locations. We get more pollutions in the upstream locations than the downstream locations. Hence, the r-rates at downstream locations are higher than at upstream locations. But in some cases, we get fluctuation in upstream locations, which indicate that upstream locations are more sensitive. Table 2.7 presents the optimal injection rates in three individual stress periods. The joint objective function is applying by $f = f_1 + f_2$. We consider the injection rate ranges $[0.05, 0.8]$ for Mg^{2+} and $[0.06, 0.9]$ for Cl^- at four different injection locations. We use injection rate of 0.1 for obtaining the observations solution where the noise level is $\zeta = 0.2$. As we observe from Table 2.7, both Mg^{2+} and Cl^- show more contamination upstream than downstream. Consequently, the pollution is increasing in each stress period. The r-rates difference between the two stress periods is around 10% at downstream locations, which is almost consistent for every scenario. On the other hand, the r-rates difference at upstream locations is around 15%, but it's fluctuating. This behaviour establishes that the

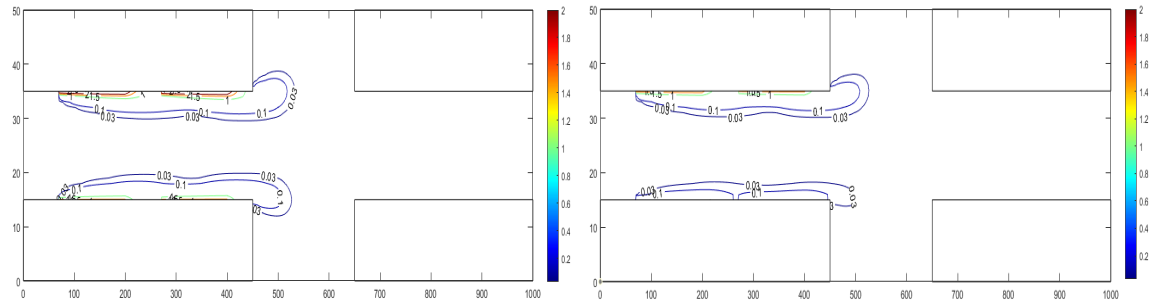

(a) $t = 90$ days

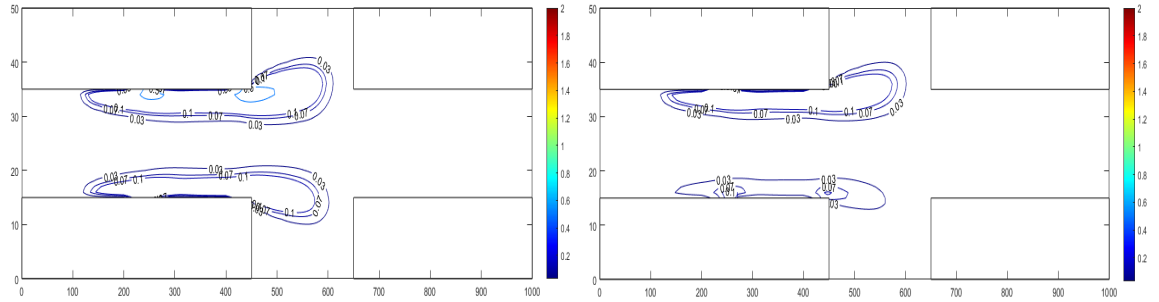

(b) $t = 150$ days

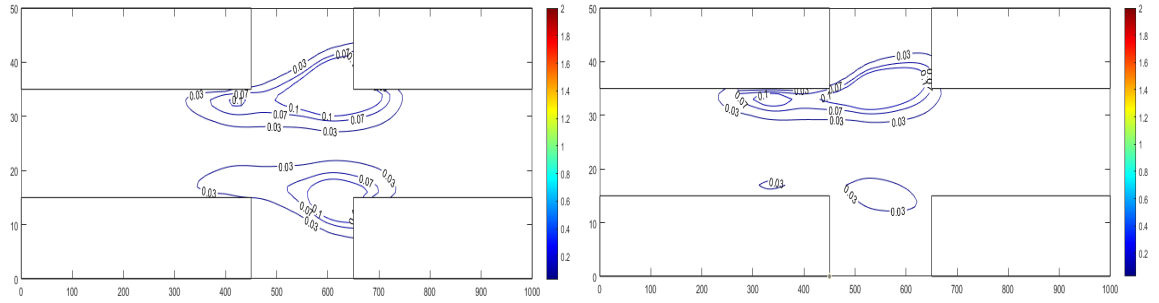

(c) $t = 210$ days

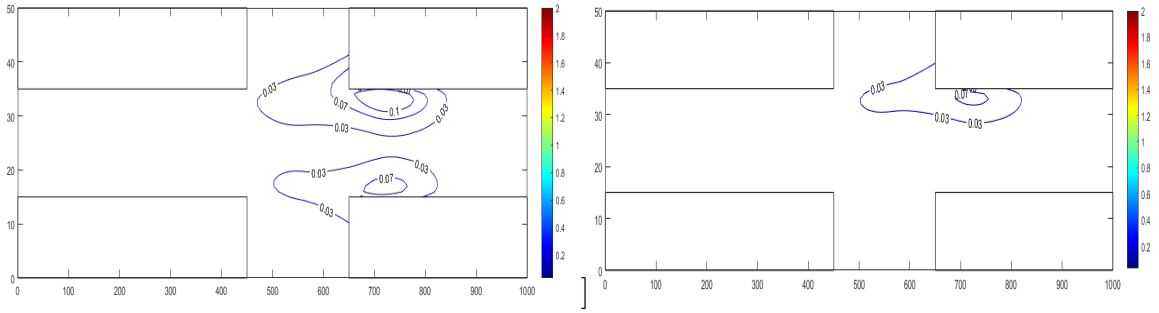

(d) $t = 360$ days

Figure 2.10: Concentration distributions of pollutant Cl^- at different time. Left column with maximum injection rates; Right column with optimal injection rates obtained by the optimal control approach.

upstream injection is more sensitive.

Finally, we compare the concentration distributions of the pollutants without optimization injection rates and with optimal injection rates from the optimal control process. We take the maximum injection rates for Mg^{2+} and Cl^{-} at $P_{L_1} = P_{L_2} = 0.2$ and $P_{U_1} = P_{U_2} = 0.9$. On the other hand, We take the optimal injection rates for Mg^{2+} at $P_{L_1} = 0.13, P_{L_2} = 0.11, P_{U_1} = 0.57$ and $P_{U_2} = 0.51$ and for Cl^{-} at $P_{L_1} = 0.14, P_{L_2} = 0.11, P_{U_1} = 0.56$ and $P_{U_2} = 0.52$. To compute optimal injection rates, we simulated the multicomponent optimal control model. The injection rate ranges in four different injection segments are $P_{L_1} = P_{L_2} = [0.05, 0.2]$ and $P_{U_1} = P_{U_2} = [0.1, 0.9]$ for both Mg^{2+} and Cl^{-}. Additionally, we took injection rates for the observation solution at O_1 and O_3 are 0.08 and O_2 and O_4 are 0.5 for Mg^{2+} and Cl^{-} and we added low level of noise $\zeta = 0.05$ in the observed solution simulation, where the same parameter values were used as the previous experiment. The total time period is 12 months. The pollutions are injected for the first three months. Each stress period is considered to be one month long. We use the spatial step sizes as $\Delta x = \Delta y = 1m$ and the time step size as $\Delta t = 1day$. In Fig. 3.5 and Fig. 3.6, the right columns present the pollutant concentrations of controlled pollution with the optimal injected rates, by the optimal control approach, based on the joint objective function of the overall fitness errors and reduction costs $f = f_1 + f_2$, while the left columns present the pollutant concentrations without controlling, which are with the maximum injection rate of $\mathbf{P} = P^{max}$, for the same time period. From the figures, we can see that the pollution concentrations (right) by the controlled approach are clearly reduced in pollution, comparing with those pollution concentrations (left) without controlling. In addition, the concentrations of pollutants reduce significantly in time as the water flows. This shows that applying the optimal control approach at the pollutant injections has obtained the reduction of multicomponent pollutions in the flow.

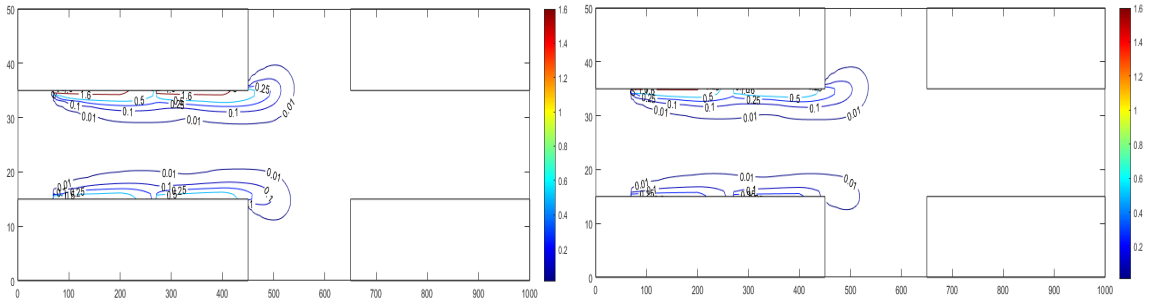

(a) $t = 90$ days

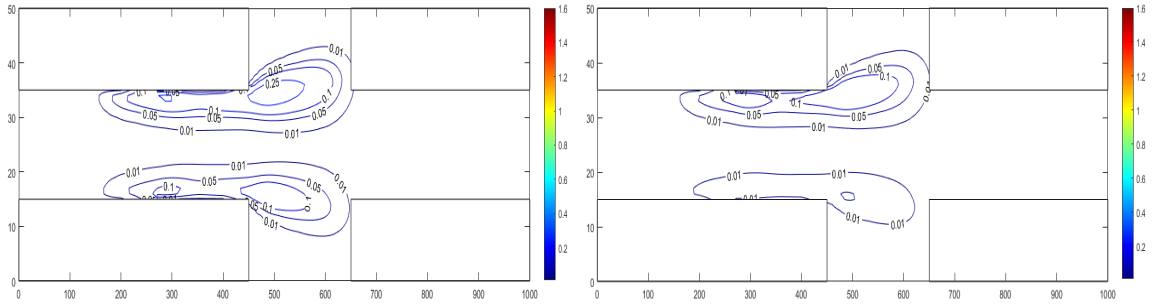

(b) $t = 180$ days

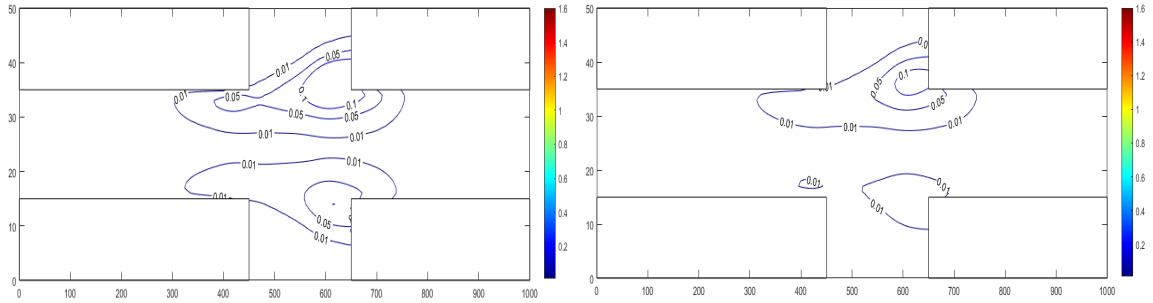

(c) $t = 270$ days

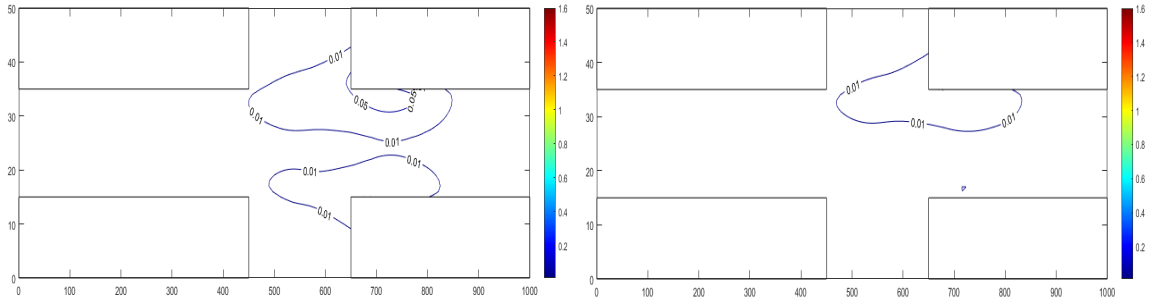

(d) $t = 360$ days

Figure 2.11: Concentration distributions of pollutant Mg^{2+} at different time. Left column with maximum injection rates; Right column with optimal injection rates obtained by the optimal control approach.

Chapter 3

The Parallel DE-PDE Multicomponent Pollution Optimal Control Approach for Contamination Flows in Porous Media

3.1 Introduction

Groundwater contamination involving multiple reactive species presents a significant challenge for environmental management due to the coupled effects of advection, diffusion, and nonlinear geochemical reactions in porous media [44, 85]. Designing effective remediation strategies requires not only accurate simulation of multicomponent transport processes but also optimization procedure capable of balancing environmental objectives with operational and economic constraints [39, 122]. In PDE-constrained groundwater control problems, the challenge is further intensified by the high dimensionality and strong nonlinearity arising from the coupling between transport dynamics and control variables [75, 73].

In this chapter, we develop a problem-specific parallel DE-PDE algorithm to efficiently tackle the computational challenges of large-scale optimization in multicomponent groundwater contamination control, where population-based search is distributed across processors and each candidate solution is evaluated through full PDE simulation parallelly. The associated objective function incorporates both a concentration least squares error term and a piecewise-defined abatement cost function. The parallel DE-PDE approach integrates a stable and high-fidelity PDE solver to simulate multicomponent groundwater flow and contaminant transport processes. The first numerical experiment evaluates the efficiency of the parallel DE-PDE model, emphasizing its scalability and computational performance for large-scale groundwater contamination problems. The second experiment investigates the behaviour of the piecewise abatement cost function under various physical scenarios within a hypothetical rectangular aquifer. The final example considers a realistic aquifer with discontinuous injection, showing that optimal control strategies build in parallel DE-PDE algorithm achieve superior contamination reduction compared to maximum injection.

3.2 Mathematical Model of Multicomponent Pollution Optimal Control

We present the governing equations, formulated as a coupled system of nonlinear partial differential equations, to model multicomponent contaminant transports in porous media. In addition, an optimal control system is fully integrated with the multicomponent groundwater flow and transport PDE system, enabling the systematic determination of control strategies for effective contamination management.

3.2.1 Groundwater Flow and Multicomponent Transport Mathematical Model

We consider a multicomponent groundwater system in a saturated porous medium, where contaminant transport is governed by the coupled processes of flow, advection, diffusion, and nonlinear chemical reactions. We consider horizontal flow within the aquifer. No internal source or sink terms are assumed within the domain. The physical behaviour of the system is described by a set of time-dependent partial differential equations, consisting of a flow equation for the hydraulic head and a system of convection–diffusion–reaction equations for multiple chemical species. These equations are strongly coupled through the velocity field and reaction mechanisms, resulting in a nonlinear and high-dimensional model. In addition, contaminant injection is applied along a specified portion of the domain boundary. Under these assumptions, the governing equations reduce to the following form:

$$S_s \frac{\partial h}{\partial t} - \nabla.(K \nabla h) = 0, \tag{3.1}$$

$$\mathbf{u} = -K \nabla h, \tag{3.2}$$

$$\frac{\partial(\phi c_\alpha)}{\partial t} + \nabla.(\mathbf{u} c_\alpha - D \nabla c_\alpha) = \mathbf{R}_\alpha(\mathbf{c}), \quad \alpha = 1, 2, \ldots, n_c, \tag{3.3}$$

where, S_s is the specific storage $[L^{-1}]$, h is the hydraulic head $[L]$. K is hydraulic conductivity $[LT^{-1}]$, described by $K = \frac{k\rho g}{\mu}$, k represents the permeability $[L^2]$, and μ represents the viscosity $[ML^{-1}T^{-1}]$ of the fluid. $\mathbf{u}$ is the Darcy's velocity of the flow $[LT^{-1}]$. c_α is the concentration $[ML^{-3}]$ for α species, $\alpha = 1, 2, \ldots, n_c$. n_c is the number of species and $\mathbf{c} = (c_1, c_2, \ldots, c_{n_c})$. ϕ is the porosity. The diffusion coefficient is D. $\mathbf{R}_\alpha(\mathbf{c})$ represents nonlinear chemical reaction $[ML^{-3}T]$ that describes the mineral precipitation-dissolution reactions and the intra-aqueous reactions.

The initial conditions are

$$h(x, y, 0) = h_0(x, y, 0), \quad (x, y) \in \Omega, \tag{3.4a}$$

$$c_\alpha(x, y, 0) = c_{\alpha_0}(x, y, 0), \quad \alpha = 1, 2, \ldots, n_c, \quad (x, y) \in \Omega, \tag{3.4b}$$

and the Dirichlet and Neumann boundary conditions for the water head are given as

$$h(a_x, y, t) = h_{left}(y, t), \quad h(b_x, y, t) = h_{right}(y, t), \tag{3.5a}$$

$$\frac{\partial h}{\partial y}(x, t) = 0, \quad (x, y) \in \text{the top and bottom boundaries of } \Omega. \tag{3.5b}$$

Let the first group of concentrations, c_β, $\beta = 1, 2, ..., n_e$, represent the concentrations of the existing components within aquifer water and let the second group of concentrations, c_γ, $\gamma = n_e + 1, n_e + 2, \ldots, n_c$, represent the concentrations of the injected components into aquifer througn specific boundary locations. The boundary conditions of concentrations are given as

$$\frac{\partial c_\beta}{\partial x}(y, t) = 0, \quad \frac{\partial c_\beta}{\partial y}(x, t) = 0, \quad (x, y) \in \partial\Omega, \quad \beta = 1, 2, \ldots, n_e, \tag{3.6a}$$

$$\frac{\partial c_\gamma}{\partial y}(x, t) = -P_{\gamma_l}, on\ \Gamma_l, l = 1, 2, \ldots, n_s, \ \frac{\partial c_\gamma}{\partial x} = 0, \frac{\partial c_\gamma}{\partial y} = 0, \quad \text{on} \quad \partial\Omega \backslash \cup\, \Gamma_l, \tag{3.6b}$$

where, $\gamma = n_e + 1, n_e + 2, \ldots, n_c$. The Γ_l, $l = 1, 2, \ldots, n_s$, represent the segments located on the upper boundary of the domain where the pollutions are injected into the aquifer. P_{γ_l}, where $l = 1, 2, \ldots, n_s$, are the injection rates for the γ's pollutant. $\partial\Omega \backslash \cup\, \Gamma_l$ represents the rest boundary except $\cup\Gamma_l$ of the aquifer.

3.2.2 Multicomponent Contamination Optimal Control Model

The objective of the multicomponent optimal control model is to determine optimal pollutant injection rates that minimize the deviation between the simulated contaminant concentrations

and the prescribed environment standards at the observation locations, while simultaneously accounting for the cost of pollution control. The multicomponent pollution optimal control model can be described as follows

$$\min_{\{P_{\gamma_l}\}} f(\mathbf{P}_{\gamma_1}) = \min_{f\{P_{\gamma_l}\}} \{f_1(\mathbf{P}_{\gamma_1}) + f_2(\mathbf{P}_{\gamma_1})\}; \tag{3.7}$$

subject to

$$\text{The governing system of PDEs:} \quad (3.1) - (3.6b), \tag{3.8}$$

$$c_{\gamma_s}^{min} \leq c_{\gamma_s} \leq c_{\gamma_s}^{max}, \quad s = 1,\, 2,\, \ldots,\, n_{ob},\ \gamma = n_e + 1,\, n_e + 2,\, \ldots,\, n_c, \tag{3.9}$$

$$P_{\gamma_l}^{min} \leq P_{\gamma_l} \leq P_{\gamma_l}^{max}, \quad l = 1,\, 2,\, \ldots,\, n_s,\ \gamma = n_e + 1,\, n_e + 2,\, \ldots,\, n_c, \tag{3.10}$$

where $\mathbf{P}_{\gamma_l} = \{P_{\gamma_l};\ l = 1,\, 2,\, \ldots,\, n_s,\ \gamma = n_e + 1,\, n_e + 2,\, \ldots,\, n_c\}$.

The objective function $f(\mathbf{P}\gamma_l)$ is composed of two main components. The first component, $f_1(\mathbf{P}\gamma_l)$, represents the overall fitness and quantifies the discrepancy between the simulated concentrations c_{γ_s} and the observed concentrations $c_{\gamma_s}^{ob}$. The second component, $f_2(\mathbf{P}_{\gamma_l})$, accounts for the abatement and maintenance costs associated with the control strategy. $f_1(\mathbf{P}\gamma_l)$ is defined as follows:

$$f_1(\mathbf{P}_{\gamma_l}) = \sum_{s=1}^{n_{ob}} \sum_{\gamma=n_e+1}^{n_c} \int_0^T \omega_{\gamma_s} \left[c_{\gamma_s}(\mathbf{P}_{\gamma_l}, t) - c_{\gamma_s}^{ob}(t)\right]^2 dt \tag{3.11}$$

which represents the concentration least squares error that defines the overall fitness between the simulated concentrations $c_{\gamma_s}(\mathbf{P}_{\gamma_l}, t)$ and the allowable environmental concentrations $c_{\gamma_s}^{ob}(t)$ at the observation sites with weight ω_{γ_s}. The allowable environmental concentrations $c_{\gamma_s}^{ob}(t)$ are perturbed from the ideal concentration at minimum injection rates. The weight functions ω_{γ_s} are designed to normalize the component affection in the objective function which has defined in chapter two equation (2.16).

The function $f_2(r_{\gamma,l})$ is introduced to represent the cost associated with contaminant abatement at the injection locations [90]. For each species γ at location l, it evaluates the total cost required to attain a specified reduction rate $r_{\gamma,l}$ over the simulation horizon. The cost model is composed of two terms: a fixed cost term, reflecting capital investment and infrastructure requirements, and a variable cost term, which accounts for operational expenses that increase with the magnitude of the reduction effort. This formulation provides a practical and economically consistent description of treatment costs in groundwater remediation. The cost function $f_2(\mathbf{r}_{\gamma,l})$ defines as follow:

$$f_2(\mathbf{P}_{\gamma_l}) = \sum_{l=1}^{n_s} \sum_{\gamma=n_e+1}^{n_c} \int_0^T \omega_2 A_{\gamma_l}(r_{\gamma_l}) dt \tag{3.12}$$

with,

$$A_{\gamma_l}(r_{\gamma_l}) = \left(b_{1,l} W_{\gamma_l}^{b_{2,l}} + b_{3,l} W_{\gamma_l}^{b_{2,l}} r_{\gamma_l}^{b_{4,l}} \right),$$

where, the term of $b_{1,l} W_{\gamma_l}^{b_{2,l}}$ represents fixed treatment cost which is the power function of treatment volume at the l^{th} injected site and the total treated contamination volumes W_{γ_l} according to daily production activities are defined by

$$W_{\gamma_l} = P_{\gamma_l}^{max} \quad for \quad l = 1, 2, ..., n_s, \quad \gamma = n_e + 1,\ n_e + 2,\ \ldots,\ n_c, \tag{3.13}$$

and the influent rates, commonly known as reduction rates, are defined as

$$r_{\gamma_l} = \frac{P_{\gamma_l}^{max} - P_{\gamma_l}}{P_{\gamma_l}^{max}},\ for\ l = 1,\ 2,\ \ldots,\ n_s, \quad \gamma = n_e + 1,\ n_e + 2,\ \ldots,\ n_c, \tag{3.14}$$

where, $P_{\gamma_l}, \gamma = n_e + 1,\ n_e + 2,\ \ldots,\ n_c$, are the injection rates of injected components.
The abatement cost function $f_2(r_{\gamma,l})$ assumes a uniform charge rate for all pollution sources. However, in practice, treatment costs vary significantly with the level of pollution and the required degree of reduction. Lower levels of treatment may be achieved with relatively

simple and cost-effective methods, whereas higher levels of pollution control often require more advanced and expensive technologies. To better reflect this realistic behaviour, we propose a modified abatement cost function $f_2'(r_{\gamma,l})$ that captures the nonlinear relationship between pollution levels and treatment costs. The modified function $f_2'(r_{\gamma,l})$ models the abatement cost through a threshold-based piecewise formulation that distinguishes between moderate and high levels of contaminant reduction. The key parameter in this formulation is the critical reduction rate r_c, which separates conventional treatment from intensified remediation. When the effective reduction $r_{\gamma l}$ remains below this threshold r_c, the associated cost evolves gradually according to a baseline nonlinear relationship, representing typical operational conditions. Once the reduction level surpasses r_c, the cost structure changes significantly by incorporating an additional penalty b_5, leading to a sharper increase in total cost. This transition reflects the disproportionate effort and expense required to achieve high removal efficiencies, often involving advanced technologies or stricter regulatory compliance. The modified objective function $f_2'(r_{\gamma,l})$ is forme as follows:

$$f_2'(\mathbf{P}_{\gamma_l}) = \sum_{l=1}^{n_s} \sum_{\gamma=n_e+1}^{n_c} \int_0^T \omega_3 A'_{\gamma_l}(r_{\gamma_l}) dt \tag{3.15}$$

with,

$$A'_{\gamma_l}(r_{\gamma_l}) = \begin{cases} \left(b_{1,l} W_{\gamma_l}^{b_{2,l}} + b_{3,l} W_{\gamma_l}^{b_{2,l}} r_{\gamma_l}^{b_{4,l}}\right), & for \quad r < r_c, \\ \left(b_{1,l} W_{\gamma_l}^{b_{2,l}} + b_{3,l} W_{\gamma_l}^{b_{2,l}} r_{\gamma_l}^{b_{4,l}} + b_{5,l} W_{\gamma_l}^{b_{2,l}} \left((r - r_c)_{\gamma_l}^{b_{6,l}}\right)\right), & for \quad r \geq r_c. \end{cases}$$

The terms $b_{3,l} W_{\gamma_l}^{b_{2,l}} r_{\gamma_l}^{b_{4,l}}$ and $b_{5,l} W_{\gamma_l}^{b_{2,l}} \left((r - r_c)_{\gamma_l}^{b_{6,l}}\right)$ are called variable treatment cost or abatement cost due to reduction effort before and after threshold r_c respectively.

Further, each parameter plays a critical role in capturing the economic and technical complexity of groundwater pollution remediation. The threshold reduction rate r_c defines the point at which the cost structure changes, representing regulatory limits or technological

boundaries, where basic treatment transitions to advanced methods.

The parameter b_1 represents fixed setup costs, independent of reduction effort, while b_2 captures economies of scale in the treated volume W. For reduction levels below the threshold, the variable cost is governed by cost coefficient b_3 and growth exponent b_4, controlling the magnitude and rate of cost increase. Beyond the threshold, an additional penalty term is introduced, scaled by cost coefficient b_5 and shaped by the exponent b_6, reflecting the higher costs associated with advanced treatment and stricter regulatory requirements. Together, these parameters enable a continuous yet nonlinear cost function that captures both gradual cost increases at low reduction levels and rapid escalation at higher treatment intensities.

Additionally, the concentrations simulated at observation sites, denoted as $c_{\gamma_s}^{ob}$, always satisfy within a specific interval of concentrations during the simulation period. The injection rates P_{γ_l} are bounded by upper and lower values.

3.3 Discrete Multicomponent Pollution Optimal Control Model

In this section, we present the discrete multicomponent optimal control model for groundwater contamination. The continuous PDE-constrained continuous model is transformed into a finite-dimensional system through discretization. This discrete model provides the basis for numerical optimization staggered control of multicomponent contamination processes.

3.3.1 Numerical Scheme for Governing Equations

We discretize the governing equations (3.1)–(3.6b) using the splitting-improved upwind finite difference scheme. The numerical scheme is formulated on a staggered grid with spatial indices $(i,\ j)$ and discrete time levels t^n. It combines the directional operator splitting with a staggered grid discretization, as illustrated in Figure 2.1 of Chapter 2. The hydraulic

head $H_{i,\,j}$ is defined at integer grid points and is discretized using a two-step splitting procedure. In the first substep, the x-direction operator is applied from t^n to $t^{n+\frac{1}{2}}$, yielding an intermediate solution $H^{n+\frac{1}{2}}_{i,\,j}$, where spatial derivatives are discretized along the x-direction. In the second substep, the y-direction operator is applied from $t^{n+\frac{1}{2}}$ to t^{n+1}, producing the updated hydraulic head $H^{n+1}_{i,\,j}$. This splitting effectively reduces the two-dimensional flow model into a sequence of one-dimensional models.

The Darcy velocity field is then computed from the discrete gradient of the hydraulic head at time level t^{n+1}. Specifically, the velocity components are evaluated on a staggered grid to ensure flux continuously: the x-direction velocity $U^{n+1}_{x_{i,\,j}}$ is defined at integer grid points, while the y-direction velocity $U^{n+1}_{y_{i+\frac{1}{2},\,j+\frac{1}{2}}}$ is defined at half-grid locations on the grid. These are obtained through discrete approximations of the hydraulic gradient, ensuring consistent coupling between pressure and flux variables.

For the multicomponent transport equations, the concentration field is advanced using a similar directional splitting strategy. In the first substep, from t^n to $t^{n+\frac{1}{2}}$, the advection-diffusion operator in the x-direction is applied to obtain $C^{n+\frac{1}{2}}_{\alpha_{i+\frac{1}{2},\,j}}$, where the concentration is evaluated at half-grid points in the x-direction to align with the corresponding fluxes. In the second substep, from $t^{n+\frac{1}{2}}$ to t^{n+1}, the y-direction operator is applied, yielding the updated concentration $C^{n+1}_{i+\frac{1}{2},\,j}$ at integer grid points in y-direction.

The modified diffusion coefficients are given to stabilize the discretization of the advection terms by incorporating flow direction into the effective diffusion. In the x-direction splitting step, the modified diffusion coefficient $D^*_{x_{i+\frac{1}{2},\,j}}$ is defined at half-grid locations consistent with the concentration $C_{\alpha_{i+\frac{1}{2},\,j}}$, and depends on the local velocity $U^{n+1}_{x_{i,\,j}}$ such that additional diffusion is applied in the upwind direction. Similarly, in the y-direction splitting step, the coefficient $D^*_{y_{i+\frac{1}{2},\,j+\frac{1}{2}}}$ is defined at half-grid locations aligned with the corresponding flux direction and depends on $U^{n+1}_{y_{i+\frac{1}{2},\,j+\frac{1}{2}}}$. These directionally dependent coefficients augment the physical diffusion to ensure numerical stability while preserving sharp concentration fronts,

thereby providing a consistent and stable discretization of the transport equation on the staggered grid.

Overall, the combination of directional splitting and improved upwind disceitization on staggered grid leads to a stable and efficient numerical scheme that preserves the structure of the underlying flow and transport processes. It reduces the multidimensional problem into a sequence of lower-dimensional updates, minimizes numerical diffusion in advection-dominated regimes, and maintains consistency between hydraulic gradients, velocities, and concentration fluxes.

3.3.2 Discrete Multicomponent Pollution Optimal Control Model

To solve the multicomponent pollution optimal control model (3.7)-(3.10) numerically, the continuous formulation is discretized in both space and time. This process converts the coupled system of governing PDEs and associated control variables into a finite-dimensional optimization problem defined on a structured computational grid. Accordingly, the continuous objective function is approximated by a discrete counterpart, where the spatial and temporal integrals are replaced by summations over grid points and time levels. The discrete objective function accounts for the concentration deviations at prescribed observation locations as well as the corresponding abatement costs associated with the control variables. In particular, for each chemical species and time level, the state variables are evaluated at discrete grid points, while the control variables, defined at the injection locations, are incorporated consistently within the discretized system. This discrete model preserves the essential structure of the original continuous problem while enabling efficient numerical evaluation. It also allows the objective function to be computed repeatedly by the PDE solver and efficiently within the optimization algorithm. The discrete objective function can be described as

$$F\left(\mathbf{P}_{\gamma_l}\right) \;=\; \sum_{s=1}^{n_{ob}} \sum_{\gamma=n_e+1}^{n_c} \sum_{n=1}^{N_t} \omega_{\gamma_s} \left[C_{\gamma_s}\left(\mathbf{P}_{\gamma_l}, t^n\right) - C_{\gamma_s}^{ob}(t^n)\right]^2 \Delta t$$

$$+\sum_{l=1}^{n_s}\sum_{\gamma=n_e+1}^{n_c}\sum_{n=1}^{N_t}\omega_2 A'_{\gamma_l}\left(r_{\gamma_l}(t^n)\right)\Delta t \tag{3.16}$$

Thus, the discrete multicomponent pollution optimal control model is defined as finding the optimal P_{γ_l}, $\gamma = n_e+1,\, n_e+2,\, \ldots,\, n_c$, $l = 1,\, 2,\, \ldots,\, n_s$ such that

$$\min_{\{P_{\gamma_l}\}} F\left(\mathbf{P}_{\gamma_l}\right) \tag{3.17}$$

subject to

$$\text{The splitting improved upwind scheme (in chapter 2) of} \quad (2.5)-(2.20), \tag{3.18}$$

$$c_{\gamma_s}^{min} \le C_{\gamma_s}(t^n) \le c_{\gamma_s}^{max}, \quad \gamma = n_e+1,\, n_e+2,\, \ldots,\, n_c, \quad s = 1,\, 2,\, \ldots,\, n_{ob}, \tag{3.19}$$

$$P_{\gamma_l}^{min} \le P_{\gamma_l} \le P_{\gamma_l}^{max}, \quad \gamma = n_e+1,\, n_e+2,\, \ldots,\, n_c, \quad l = 1,\, 2,\, \ldots,\, n_s, \tag{3.20}$$

where the simulated numerical concentrations at the observation sites are $\{C_{\gamma_s}(t^n)\}$. The admissible range of concentrations at these locations is defined by the lower and upper bounds, $c^{\min}\gamma_s$ and $c^{\max}\gamma_s$, respectively. The terms $C_{\gamma_s}^{ob}(t^n)$ represent the allowable concentrations at the observation sites, which are obtained by simulating the system under minimum injection rates $P_{\gamma_l} = P_{\gamma_l}^{\min}$ or other prescribed injection scenarios.

3.4 Parallel DE-PDE Algorithm for Multicomponent Contamination Control

3.4.1 MPI Parallel System

The Message Passing Interface (MPI) is a standardized communication protocol widely used for parallel computing on distributed-memory systems, particularly in high-performance computing (HPC) environments. It provides an efficient framework for distributing computa-

tional tasks across multiple processors while enabling communication and synchronization among them. A sophisticated approach in MPI system to mitigate these issues is the use of a master-worker architecture, where the master processor manages coordination and global information, while worker processors perform computationally intensive tasks independently. This parallel approach significantly reduces computational time and enables the effective treatment of high-dimensional, computationally intensive problems.

3.4.2 Parallel DE–PDE Optimization algorithm

In the context of PDE-constrained optimization problems, such as multicomponent groundwater contamination control, the repeated evaluation of complex numerical optimal contamination models leads to significant computational demands. We develop the parallel DE-PDE optimization approach to solve the discrete multicomponent optimal control problem (3.19)–(3.25) using a master–worker strategy within the Message Passing Interface (MPI) system. The parallelization is performed at the population level, where the evaluation of individuals (i.e., each candidate solution $\mathbf{P}_{\gamma_l}$) in each generation is distributed across multiple processors. Let, N_p be the number of population vectors and N_{proce} be the number of used processors. The total population is divided into sub-generations, with each processor handling approximately $[j = N_p/N_{proce}]$ individuals per generation. The parallel DE-PDE approach starts with MPI initialization, the master processor (rank 0) generates the $N_p l$ dimensional initial population of candidate solutions $\mathbf{P}_{\gamma_l}$ within the prescribed parameter bounds $D = \left[\mathbf{P}_{\gamma,l}^{min}, \mathbf{P}_{\gamma,l}^{max}\right]$ as follow:

$$\mathbf{P}_{\gamma,l,i} = \mathbf{P}_{\gamma,l}^{min} + \left(\mathbf{P}_{\gamma,l}^{max} - \mathbf{P}_{\gamma,l}^{min}\right) rand_j(0,1), \quad i = 1,\, 2,\, \ldots,\, N_p, \quad l = 1,\, 2,\, \ldots,\, n_s, \quad (3.21)$$

and evaluates their corresponding objective-function values using the PDE solver satisfying the following restriction condition.

$$f_{\gamma_s}^{n}(\mathbf{P}_{\gamma_l}) = C_{\gamma_s}^{n} - C_{\gamma_s}^{n,max} \leq 0, \quad s = 1,\, 2,\, \ldots,\, n_{ob}, \quad n = 1,\, 2,\, \ldots,\, N_t, \tag{3.22a}$$

$$f_{\gamma_s}^{N_t+n}(\mathbf{P}_{\gamma_l}) = C_{\gamma_s}^{n,min} - C_{\gamma_s}^{n} \leq 0, \quad s = 1,\, 2,\, \ldots,\, n_{ob}, \quad n = 1,\, 2,\, \ldots,\, N_t. \tag{3.22b}$$

After that, the initialized population and objective-function values are distributed to all worker processors.

During each generation, the master processor first stores the previous generation population and its associated objective-function values and broadcasts this information to all worker processors using MPI_Bcast. Each worker processor independently receives the global population data and performs the DE-PDE evolutionary operations for its assigned subset of individuals. Specifically, worker processors construct mutant vectors from previous generation distinct population members, apply crossover to generate trial vectors, and evaluate the objective-function values of the trial solutions by invoking the PDE solver. In each individual processor, the DE-PDE algorithm performs the following steps.

Definition 4.2.1 For the constrained optimization problem, we define the satisfaction function $\phi(\cdot)$: $D \to R$ by

$$\phi(\mathbf{P}_{\gamma_l}) = \sum_{n=1}^{N_t} \sum_{\gamma=n_e+1}^{n_c} \sum_{s=1}^{n_{ob}} \left(G_{\gamma_s}^{n} + G_{\gamma_s}^{N_t+n} \right), \tag{3.23}$$

where

$$G_{\gamma_s}^{n}(\mathbf{P}_{\gamma_l}) = \begin{cases} \frac{1}{2}, & f_{\gamma_s}^{n}\left(\mathbf{P}_{\gamma_l}\right) \leq 0, \\ \frac{1}{1+exp\left(f_{\gamma_s}^{n}\left(\mathbf{P}_{\gamma_l}\right)\right)}, & otherwise, \end{cases} \tag{3.24a}$$

$$G_{\gamma_s}^{N_t+n}(\mathbf{P}_{\gamma_l}) = \begin{cases} \frac{1}{2}, & f_{\gamma_s}^{N_t+n}\left(\mathbf{P}_{\gamma_l}\right) \leq 0, \\ \frac{1}{1+exp\left(f_{\gamma_s}^{n}\left(\mathbf{P}_{\gamma_l}\right)\right)}, & otherwise \end{cases} \tag{3.24b}$$

Let, $S = \left\{ \mathbf{P}_{\gamma_l} | \quad \mathbf{P}_{\gamma_l} \in D \wedge [f_{\gamma_s}^{n} \leq 0] \wedge [f_{\gamma_s}^{N_t+n} \leq 0] \right\}$. It's obvious that $\phi\left(\mathbf{P}_{\gamma_s}\right) = N_t(n_c - n_e)$ when $\mathbf{P}_{\gamma_l} \in S$ and $0 < \phi(\mathbf{P}_{\gamma_l}) < N_t(n_c - n_e)$ when $\mathbf{P}_{\gamma_l} \notin S$. The more of the constraint violation number of $\mathbf{P}_{\gamma_l}$, the less of the value of $\phi\left(\mathbf{P}_{\gamma_l}\right)$.

Definition 4.2.2 Suppose $\mathbf{P}_{\gamma_l}$ and $\mathbf{Q}_{\gamma_l}$ are two different individuals from the next two generations, we define the following function

$$prior(\mathbf{P}_{\gamma_l}, \mathbf{Q}_{\gamma_l}) = \begin{cases} 1, & \phi(\mathbf{P}_{\gamma_l}) = \phi(\mathbf{Q}_{\gamma_l}) \text{ and } f(\mathbf{P}_{\gamma_l}) < f(\mathbf{Q}_{\gamma_l}) \text{ Or } \phi(\mathbf{P}_{\gamma_l}) > \phi(\mathbf{Q}_{\gamma_l}), \\ 0, & otherwise. \end{cases} \tag{3.25}$$

If the constraint violation number of $\mathbf{P}_{\gamma_l}$ > the constraint violation number of $\mathbf{Q}_{\gamma_l}$, that is $\phi(\mathbf{P}_{\gamma_l}) > \phi(\mathbf{Q}_{\gamma_l})$, we say that $\mathbf{P}_{\gamma_l}$ is prior to $\mathbf{Q}_{\gamma_l}$ and $prior(\mathbf{P}_{\gamma_l}, \mathbf{Q}_{\gamma_l}) = 1$. Where $f(\mathbf{P}_{\gamma_l})$ is the objective function.

The mutation follows the DE/rand-to-best/2/exp strategy:

$$\mathbf{V}_{\gamma,l,j}^{G} = \mathbf{P}_{\gamma,l,r_1}^{G,\text{prev}} + F\left(\mathbf{P}_{\gamma,l,best}^{G,\text{prev}} - \mathbf{P}_{\gamma,l,r_2}^{G,\text{prev}}\right) + \lambda\left(\mathbf{P}_{\gamma,l,r_3}^{G,\text{prev}} - \mathbf{P}_{\gamma,l,r_4}^{G,\text{prev}}\right), \tag{3.26}$$

where F be the crossover factor and λ is a control parameter that further improves the quality of the greediness of the scheme by including the current optimal vector crossover phase. Let, $\mathbf{U}_{\gamma,l,j}^{G}$ is the trial vectors that are produced in a probabilistic way by crossing mutant vectors $\mathbf{V}_{\gamma,l,j}^{G}$, and target vectors $\mathbf{P}_{\gamma,l,j}^{G}$ as follows

$$\mathbf{U}_{\gamma,l,j}^{G} = \begin{cases} \mathbf{V}_{\gamma,l,j}^{G}, & if \quad l = randb(l), \\ \mathbf{P}_{\gamma,l,j}^{G,\text{prev}}, & if \quad l \neq randb(l). \end{cases} \tag{3.27}$$

After completing the mutation and crossover processes, each processor evaluates its assigned trial vectors $\mathbf{U}_{\gamma,l,j}^{G}$ by solving the PDE system using the above numerical solver subroutine.

Algorithm: Parallel DE–PDE Contamination Optimization Algorithm.

Input: PDE model parameters, DE parameters.

Initialization of parallel MPI: MPI_parameters, MPI_Init, MPI_Comm_rank (K), MPI_Comm_size (S).

Initialization on master processor (rank $K = 0$):

Generate initial population $\mathbf{P}_{\gamma_l}^0 = \{\mathbf{P}_{\gamma_l}^0(i)\}_{i=0}^{NP-1}, \quad \mathbf{P}_{\gamma_l}^0(i) \in D.$

Evaluate initial fitness values $f_i^0 = f(\mathbf{P}_{\gamma_l}^0(i))$ using the **Contamination_PDE_solver**

Set $g \leftarrow 0$

Determine the global best: $\mathbf{P}_{\gamma_l}^0(best) \in \{\mathbf{P}_{\gamma_l}^0(i)\}_{i=0}^{NP-1}$, $f_{best}^0 = f(\mathbf{P}_{\gamma_l}^0(best))$

while $G < G_{\max}$ **do**

Step 1: Broadcast previous generation on master processor (rank $K = 0$)

Store $\mathbf{P}_{\gamma_l}^{G,\,prev}(i) \leftarrow \mathbf{P}_{\gamma_l}^{G}(i)$, $f_i^{G,\,prev} \leftarrow f_i^G$

MPI_Bcast($\mathbf{P}_{\gamma_l}^{G,\,prev}(i)$); MPI_Bcast($f_i^{G,\,prev}$)

Step 2: Parallel evolution on worker processors (rank $K = 0,\ 1, \ldots,\ S-1$)

Each worker processor w receives $\mathbf{P}_{\gamma_l}^{G,\,prev}(i)$ and $f_i^{G,\,prev}$

Partition population indices $\{i = 0,\ 1,\ \ldots,\ NP-1\}$ among worker processors; worker processor $\{w = K || K = 0,\ 1, \ldots,\ S-1\}$ handles $I_w = NP/S$.

for each $i \in I_w$ **do**

Select distinct indices $r_1, r_2, r_3 \neq i$

Generate the mutant vectors

$\mathbf{V}^G(i) = \mathbf{P}_{\gamma_l}^{G,\,prev}(r_1) + F\big(\mathbf{P}_{\gamma_l}^{G,\,prev}(best) - \mathbf{P}_{\gamma_l}^{G,\,prev}(r_2)\big) + \lambda\big(\mathbf{P}_{\gamma_l}^{G,\,prev}(r_3) - \mathbf{P}_{\gamma_l}^{G,\,prev}(r_4)\big)$

Construct trial vectors $\mathbf{U}^G(i)$ with crossover rate CR

Bounded $\mathbf{U}^G(i)$ into $D \in [\mathbf{P}_{\gamma_l}^{max},\ \mathbf{P}_{\gamma_l}^{min}]$

Evaluate concentrations C_i^{ob} calling **Contamination_PDE_solver**

Calculate fitness value for each i^{th} trail populations, $f_i^{G,trial} = f(\mathbf{U}^G(i))$

Selection:

if $f_i^{G,\mathrm{trial}} \leq f_i^{G,\mathrm{prev}}$ **then**

$\mathbf{P}_{\gamma_l}^{G+1}(i) \leftarrow \mathbf{U}^G(i)$

$f_i^{G+1} \leftarrow f_i^{G,\mathrm{trial}}$

else

$\mathbf{P}_{\gamma_l}^{G+1}(i) \leftarrow \mathbf{P}_{\gamma_l}^{G,\mathrm{prev}}(i)$

$f_i^{G+1} \leftarrow f_i^{G,\mathrm{prev}}$

end if

end for

Send updated $\mathbf{P}_{\gamma_l}^{G+1}(I_w)$ and $f^{G+1}(I_w)$ to master processor (rank $K = 0$)

Step 3: Master processor update (rank $K = 0$)

Receive updated subpopulations I_w from all worker processors and assemble full $\{\mathbf{P}_{\gamma_l}^{G+1}(i)\}_{i=0}^{NP-1}$ and f_i^{G+1}

Update global best: $\mathbf{P}_{\gamma_l}^{G+1}(best) \in \{\mathbf{P}_{\gamma_l}^{G+1}(i)\}_{i=0}^{NP-1}$, $f_{best}^{G+1} = f(\mathbf{P}_{\gamma_l}^{G+1}(best))$

if $f^* < Tol.$ **then**

Return

else

$G \leftarrow G + 1$

end if

end while

Output on master processor (rank $K = 0$): Output $\mathbf{P}_{\gamma_l}^{best}$ and $f_{best}^{G+1} = f(\mathbf{P}_{\gamma_l}^{G+1}(best))$

MPI_Finalize

It then computes $f\left(\mathbf{U}^{G}_{\gamma,l,j}\right)$ and $\phi\left(\mathbf{U}^{G}_{\gamma,l,j}\right)$ using the objective function.

Sub-Algorithm: Contamination_PDE_solver : Splitting improved upwind finite difference to contamination flow

Input: Contamination flow parameters, spatial grids (n_x, n_y), time steps N.

Step 1: Initialization: Initialize H^0, C^0_α and apply boundary conditions.

Step 2: Time-stepping loop
for $n = 0,\ 1,\ \ldots,\ N-1$ **do**
  for $j = 1,\ 2,\ \ldots,\ n_y$ **do**
    Solve $H^{n+\frac{1}{2}}_{i,j}$ along x-direction for half time step
  end for
  for $i = 1,\ 2,\ \ldots,\ n_x - 1$ **do**
    Solve $H^{n+1}_{i,j}$ along y-direction for full time step
  end for
  for $j = 0,\ 1,\ \ldots,\ n_y - 1$ **do**
    Solve $U^{n+1}_{x_{i,j}}$ along x-direction
  end for
  for $i = 1,\ 2,\ \ldots,\ n_x - 1$ **do**
    Solve $U^{n+1}_{y_{i+\frac{1}{2},j+\frac{1}{2}}}$ in y-direction
  end for
  for $j = 1,\ 2,\ \ldots,\ n_y$ **do**
    Solve $C^{n+\frac{1}{2}}_{\alpha_{i+\frac{1}{2},j}}$ along x-direction for half time step, for all α
  end for
  for $i = 0,\ 1,\ \ldots,\ n_x - 1$ **do**
    Solve $C^{n+1}_{\alpha_{i+1,j}}$ along y-direction for full time step, for all α
  end for
  Update: Set $H^n \leftarrow H^{n+1}$ and $C^n_\alpha \leftarrow C^{n+1}_\alpha$, for all α
end for

Step 3: Return all H and C_α.

To select the next generation vector, if the trail vector $\mathbf{U}^{G}_{\gamma,l,j}$ gives an equal or better objective value compared with the previous vector $\mathbf{P}^{G,\text{prev}}_{\gamma,l,j}$ objective function value then trial vector is replaced the previous vector for next generation. It can be defined as follows

$$\mathbf{P}^{G}_{\gamma,l,j} = \begin{cases} \mathbf{U}^{G}_{\gamma,l,j}, & if \quad prior\left(\mathbf{U}^{G}_{\gamma,l,j}, \mathbf{P}^{G}_{\gamma,l,j}\right) = 1, \\ \mathbf{P}^{G,\text{prev}}_{\gamma,l,j}, & otherwise. \end{cases} \tag{3.28}$$

After completing all those steps in parallel, the all worker processors send updated vectors $\mathbf{P}^{G}_{\gamma,l,j}$ and their corresponding objective function values to the master processor.

Upon receiving all updated subpopulations $\mathbf{P}^{G}_{\gamma,l,j}$ and their corresponding objective function values from the workers, the master processor reconstructs the full population for the current generation and determines the global best solution $\mathbf{P}^{G}_{\gamma,l,\ best}$ based on the lowest objective function value and its corresponding best objective function value. The convergence criterion is then evaluated; if the best objective function value satisfies the prescribed tolerance, the evolutionary loop terminates. Otherwise, the algorithm proceeds to the next generation until it reaches the maximum number of generations. Finally, the master processor outputs the optimal solution, the optimal objective function value, and the MPI environment is finalized. This MPI-based master–worker formulation enables distributed evaluation of the DE-PDE system across processors, significantly reducing computational time while maintaining the standard Differential Evolution evolutionary mechanism [46, 119].

The convergence behaviour of the parallel Differential Evolution (DE) algorithm is governed by the interplay between population diversity, evolutionary parameters, and termination criteria [5, 66]. In the proposed MPI-based DE-PDE system, convergence depends primarily on the population size N_p, mutation factor F, crossover rate CR, maximum number of generations $G_{\max}$, and stopping tolerance ε. A sufficiently large population maintains diversity and reduces premature convergence, which is particularly important in parallel DE-PDE system because subpopulations evolve concurrently across processors [70]. At each generation, the master processor broadcasts the global population to all worker processors, ensuring that mutation and crossover operations are being performed using consistent population information. This preserves the canonical DE search dynamics and supports stable convergence.

The mutation factor F and crossover rate CR jointly regulate the exploration-exploitation balance that drives convergence toward the global optimum [**price2006differential**, 97]. Meanwhile, $G_{\max}$ and ε control the convergence depth by limiting the number of evolutionary iterations and defining the required fitness accuracy [**price2006differential**, 99, 101]. Since the objective function $f(\mathbf{P}_{\gamma_l})$ is evaluated via computationally intensive PDE solves [45],

efficient parallel evaluation across MPI workers accelerates wall-clock convergence without altering the underlying DE convergence mechanism. Consequently, with appropriate parameter selection and synchronized population broadcasting, the MPI-based parallel DE-PDE system retains the convergence characteristics of standard DE while achieving substantial computational speedup for PDE-constrained optimization problems.

3.5 Numerical Experiments

In this section, we conduct numerical experiments using our developed parallel DE-PDE multicomponent pollution optimal control approach.

Example 1. To evaluate the computational efficiency and scalability of the proposed PDE-constrained optimal control model, we implemented our developed DE-PDE algorithm. The main objective of this experiment is to examine how the parallelization strategy influences runtime performance, speedup, and computational cost when solving high-dimensional, nonlinear groundwater contamination control problems.

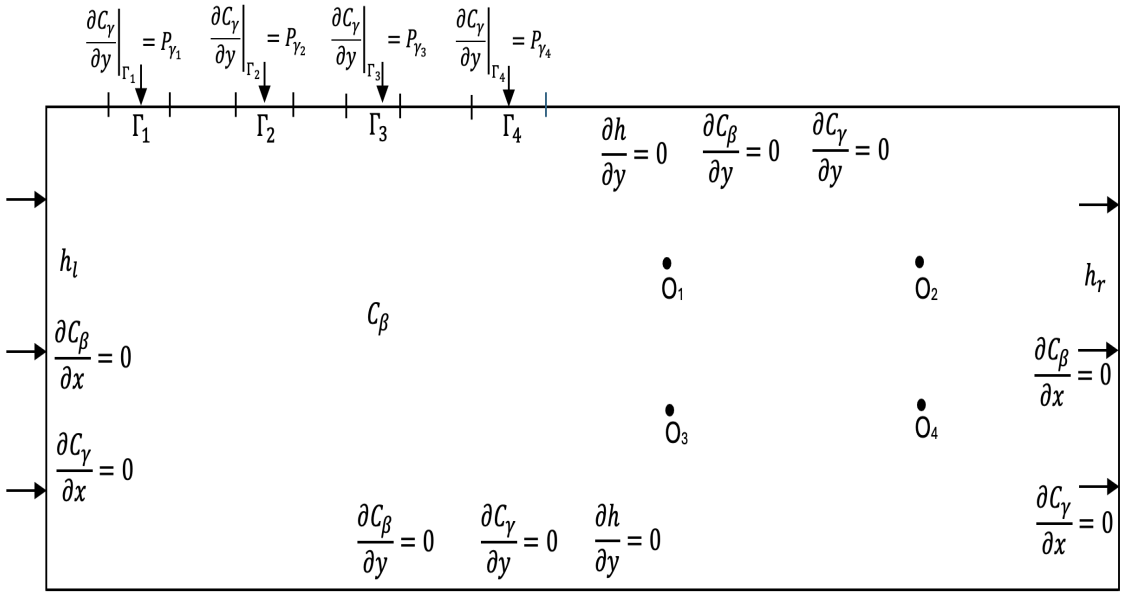

Figure 3.1: Hypothetical rectangular vertical aquifer.

We consider a three-component contamination system involving $C_\beta = C_{CO_3^{2-}}$ and $C_\gamma = C_{Mg^{2+}}, C_{Cl^-}$ where carbonate ions (CO_3^{2-}) are initially present in the aquifer, while magnesium and chloride ions are injected at designated locations along the top boundary. We consider the domain $\Omega = [0,\ 1000m] \times [0,\ 20m]$ and the total simulation time period of one years. In addition, we have a continuous pollution injection process that occurs through the injection pieces at the top boundary of the domain. The left boundary value of water head is $h_{left} = 100m$ and the right boundary value of water head is $h_{right} = 20m$. The initial condition for water head is $h_0 = 20m$ as well as the initial value for pollution concentrations $C_{Mg^{2+}}$, C_{Cl^-} are zero and $C_{CO_3^2} = 0.67mol/m^2$. We consider four injection rates P_{γ_l}, $l = 1,\ 2,\ 3,\ 4$, in the four injected pieces, and the four observation locations of $O_{n_{ob}}$, $n_{ob} = 1,\ 2,\ 3,\ 4$, are placed deep in the aquifer to track the spread of the contaminant, as shown in Fig. 3.1. For this example, the optimization focuses only the fitness component f_1 of the objective function, which minimizes the deviation between simulated and permissible concentrations at the observation sites.

The presence of multiple contaminants in a flow can greatly affect various chemical processes, including precipitation, complexation, dissolution, hydrolysis, oxidation-reduction, and more. We simulate the flow of multi-component contamination that occurs during the precipitation reaction.

The stoichiometry equation for magnesite growth is as follows

$$CO_3^{2-} + Mg^{2+} \rightarrow MgCO_3.$$

The rate of growth for magnesium carbonate is $G_r = k\ S_e C_{Mg^{2+}} C_{CO_3^{2+}}$.

The kinetic reaction for CO_3^{2-} is presented as $S_{CO_3^{2-}}\ G_r$, while that for Mg^{2+} is represented as $S_{Mg^{2+}} G_r$. The stoichiometric coefficients for the reaction involving CO_3^{2-} and Mg^{2+} are both equal to 1, denoted as $S_{CO_3^{2-}} G_r$ and $S_{Mg^{2+}}$. At a temperature of $25^0 C$, the solubility constant of $MgCO_3$ is 6.82×10^{-6}.

In computation, the observation concentration $C_{\gamma_s}^{ob}$ is defined in Chapter 2 equation (2.53). The $f_1(\mathbf{P}_{\gamma_l})$ function represents the concentration least squares error that defines the overall fitness between the simulated concentrations $c_{\gamma_s}(\mathbf{P}_{\gamma_l}, t)$ and the concentrations $c_{\gamma_s}^{ob}(t)$ at the observation sites with weight ω_{γ_s}.

$$f_1(\mathbf{P}_{\gamma_l}) = \sum_{s=1}^{n_{ob}} \sum_{\gamma=n_e+1}^{n_c} \sum_{n=1}^{N_t} \omega_{\gamma_s} [C_{\gamma_s}(\mathbf{P}_{\gamma_l}, t^n) - C_{\gamma_s}^{ob}(t^n)]^2 \Delta t. \tag{3.29}$$

The allowable environmental concentrations $c_{\gamma_s}^{ob}(t)$ are perturbed from the ideal concentration at minimum injection rates.

Table 3.1: Paralle DE-PDE Performance Summary for the objective function f_1.

γ	P_{γ_l}	AIR	Number of Processors				
			1	5	10	20	25
			Opt	*Opt*	*Opt*	*Opt*	*Opt*
Mg^{2+}	P_{γ_1}	0.2	0.226	0.233	0.226	0.213	0.236
	P_{γ_2}	0.2	0.236	0.210	0.237	0.267	0.200
	P_{γ_3}	0.2	0.200	0.239	0.200	0.200	0.253
	P_{γ_4}	0.2	0.218	0.200	0.212	0.239	0.200
Cl^-	P_{γ_1}	0.1	0.119	0.122	0.119	0.112	0.124
	P_{γ_2}	0.1	0.124	0.111	0.125	0.141	0.101
	P_{γ_3}	0.1	0.102	0.126	0.105	0.100	0.133
	P_{γ_4}	0.1	0.115	0.102	0.112	0.126	0.103
Time :			$35h\ 59m$	$6h\ 23m$	$3h\ 32m$	$2h\ 10m$	$1h\ 53m$
Obj.	val.:		$8.34e-6$	$1.89e-5$	$1.71e-5$	$3.81e-4$	$3.81e-6$

Table 3.1 presents the numerical optimization results for 1, 5, 10, 20, and 25 processors, with each processor evaluating a subset of the DE population using MPI-based communication. We consider a Population size of 100, a maximum of 150 generations and a tolerance of 10^{-6}. We consider the four injection locations on the top boundary of the left half domain. They are located between [250m 280m], [310m, 340m], [370m, 400m], and [430m, 460m] respectively. We consider the injection rates range at four different injection locations for $P_{Mg_l^{2+}}$, [0.1 0.9] and for $P_{Cl_l^-}$ [0.1 0.9], $l = 1, 2, 3, 4$.The pollutions are injected for 360 days. In Table 3.1,

AIR means actual injection rate and Opt means optimal injection rate. Four discrete areas where the pollution concentrations are somewhat constrained need to be protected. In this instance, the particular places are considered as a few points which serve as observation locations. We consider the four observation points are $O_1 = (700, 18.5)$, $O_2 = (700, 16)$, $O_3 = (800, 18.5)$ and $O_4 = (800, 16)$. We consider AIR at the observation location to find $C_{\gamma_s}^{ob}$ with the noise $\zeta = 0.1$. We use the spatial step sizes are $\Delta x = \Delta y = 1m$ and the time step size as $\Delta t = 1day$. The parameter values are given in Table 2.1.

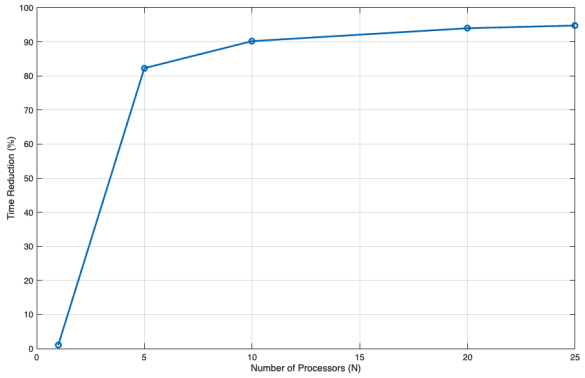

(a) Parallel DE-PDE time reduction performance metrics.

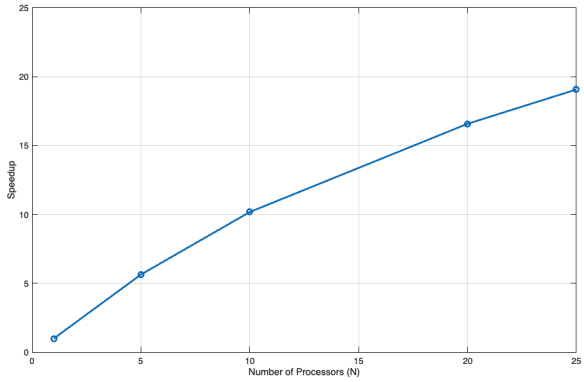

(b) Parallel DE-PDE speedup performance metrics.

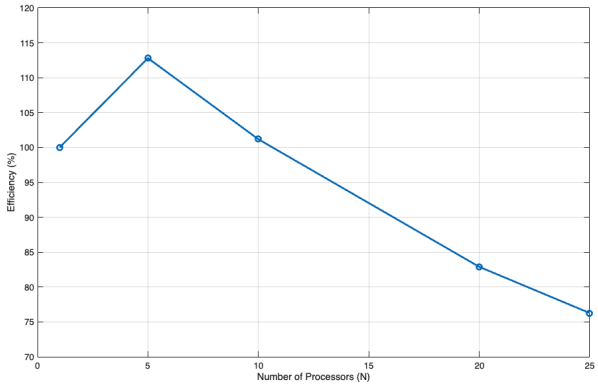

(c) Parallel DE-PDE efficiency performance metrics.

Figure 3.2: Parallel DE-PDE performance metrics: (a) Time reduction, (b) Speedup, and (c) Efficiency.

The numerical optimization results and performance metrics by the proposed parallelDE-PDE

optimal control algorithm are listed in Table 3.1. The results clearly demonstrate that the parallel DE-PDE algorithm maintains numerical robustness and solution stability across all processor configurations. The optimal injection rates $P_{Mg_l^{2+}}$ and $P_{Cl_l^-}$ at the four injection locations remain close to their actual injection rates, with only minor variations in the range of $\pm(0.02 - 0.06)$ due to the noise ζ across the 1–25 processor runs. This consistency confirms that the distributed population evaluation within MPI parallelization does not introduce instability or bias into the optimization process.

Time Reduction $= \left(\frac{T_1 - T_N}{T_1} \times 100\right)$, Speedup $= \frac{T_1}{T_N}$, Efficiency $= \frac{\text{Speedup}}{N} \times 100$,

where, N is number of processors, T_1 is simulation time with 1 processor, T_N Simulation time with N processors.

Figure 3.2a presents the variation of time reduction (%) with respect to the number of processors used in the parallel DE-PDE algorithm. The curve demonstrates a clear, monotonic increase, indicating that the computational time decreases significantly as more processors participate in the simulation. Starting from a single-processor baseline, the total runtime is reduced by nearly 82% with five processors, 90% with ten processors, and reaches approximately 94.8% reduction with twenty-five processors. This strong improvement confirms that the MPI-based population-level parallel DE-PDE efficiently distributes the workload across multiple processors.

Figure 3.2b illustrates the speedup achieved by the parallel DE–PDE solver as a function of the number of processors. The speedup curve closely follows an ideal linear trend up to approximately ten processors, where the speedup value reaches around 10.2, nearly equivalent to the number of processors employed. This near-linear growth confirms that the computational tasks are evenly distributed and efficiently executed in parallel. Interestingly, a slight superlinear acceleration is observed between five and ten processors, likely caused by improved memory usage, reduced cache misses, and lower data contention when the population and domain data are partitioned into smaller segments per processor. Beyond ten processors,

the curve begins to deviate slightly from linearity, with speedup values of approximately 16.6 for twenty processors and 19.1 for twenty-five processors. The marginal decline in the rate of increase is expected due to the rising communication cost and synchronization time associated with frequent MPI data exchanges. Despite this, the achieved speedup remains remarkably high, demonstrating that the proposed DE-PDE algorithm offers efficient scalability and effective load balancing, especially for complex PDE-constrained optimization tasks involving nonlinear and multicomponent transport processes.

Figure 3.2c depicts the parallel efficiency (%), which measures how effectively the computational resources are utilized relative to the ideal case. The efficiency curve exhibits three distinct regions. In the initial stage (up to five processors), the efficiency exceeds 100%, reaching a peak around 112%, which indicates a superlinear speedup. This behaviour is commonly observed when parallel execution improves cache utilization, reduces memory swapping, and minimizes latency compared to the serial case. In the intermediate region (around ten processors), the efficiency remains close to the ideal level at approximately 100%, confirming that the algorithm maintains a balanced computational workload without excessive communication overhead. In the final stage (beyond twenty processors), the efficiency gradually declines to around 75–80% as the benefit of additional processors is offset by increased message-passing and synchronization costs. Nevertheless, the efficiency remains well above the typical threshold for strong parallel performance, reflecting the robustness of the parallelization strategy.

Together, Figures 3.2a, 3.2b, 3.2c collectively confirm that the proposed parallel DE–PDE solver achieves near-linear scalability, significant runtime reduction, and high computational efficiency while maintaining stable optimization accuracy.

Next, we consider the four injection locations on the top boundary of the left half domain. They are located between $[250m\,280m]$, $[310m, 340m]$, $[370m, 400m]$, and $[430m, 460m]$ respectively in Table 4.2. The injection rates range at four different injection locations for

Mg^{2+} ions, [0.1 0.8] and for Cl^- ions, [0.2 0.9]. We consider the pollutions are injected for 360 days. In Table 3.3, AIR means actual injection rate, Opt means optimal injection rate, and r-rate means reduction rate. The four observation points are $O_1 = (700, 18.5)$, $O_2 = (700, 16)$, $O_3 = (800, 18.5)$ and $O_4 = (800, 16)$. We consider AIR at the observation location to find $C^{ob}_{\gamma_s}$ with the noise $\zeta = 0.1$. We use the spatial step sizes are $\Delta x = \Delta y = 1m$ and the time step size as $\Delta t = 1day$. The parameter values are given in Table 2.1. The injected locations case description is given in Table 4.2. We consider a total population size of 100, a maximum of 150 generations, and a tolerance of 10^{-6}. For each simulation, we use 10 processors for in the computation. The objective function considered here is solely f_1.

Table 3.2: Injected location case description.

	P_{γ_1}	P_{γ_2}	P_{γ_3}	P_{γ_4}
$Case\ L_1$	[250m 280m]	[310m 340m]	[370m 400m]	[430m 460m]
$Case\ L_2$	[20m 50m]	[250m 270m]	[290m 310m]	[490m 520m]
$Case\ L_3$	[20m 50m]	[70m 100m]	[430m 460m]	[490m 520m]

Table 3.3: Numerical simulations-optimization outcomes of Mg^{2+} and Cl^- injection rates across different locations for the objective function f_1 evaluated with 10 parallel processors.

γ	P_{γ_l}	AIR	$Case\ L_1$		$Case\ L_2$		$Case\ L_3$	
			Opt	r-rate (%)	Opt	r-rate (%)	Opt	r-rate (%)
Mg^{2+}	P_{γ_1}	0.2	0.382	57.55	0.732	18.67	0.278	69.11
	P_{γ_2}	0.2	0.317	64.78	0.359	60.11	0.619	31.22
	P_{γ_3}	0.2	0.499	44.56	0.374	58.44	0.361	59.89
	P_{γ_4}	0.2	0.262	70.89	0.360	60.00	0.364	59.55
Cl^-	P_{γ_1}	0.3	0.316	64.89	0.605	32.78	0.511	43.22
	P_{γ_2}	0.3	0.262	70.89	0.296	67.11	0.229	74.55
	P_{γ_3}	0.3	0.412	54.22	0.309	65.67	0.298	66.87
	P_{γ_4}	0.3	0.216	76.00	0.297	67.00	0.301	66.56
Time:			$3h\ 19m$		$3h\ 18m$		$3h\ 18m$	

Table 3.3 shows the optimization results for magnesium Mg^{2+} and chloride Cl^- ion injection rates at four injection locations under three distinct spatial configurations, L_1, L_2, andL_3. Each configuration represents a different geometric layout of injection and observation wells

within the two-dimensional domain, thereby enabling an assessment of how spatial positioning influences the efficiency of contaminant reduction.

For the Mg^{2+} ion, the optimized injection rates across configurations L_1 to L_3 generally remain above the actual injection rate, implying effective control through reduced intensity. In configuration L_1, the r-rates are relatively high—ranging from approximately 44 % to 71 %, suggesting stronger injection suppression due to shorter pollutant travel distances between the injection locations and observation wells. Configuration L_2 shows smaller r-rates (around 18 %–60 %) and higher optimized injection values, indicating that more injection is required to maintain comparable pollutant concentrations when injected locations are positioned farther apart or in regions of weaker hydraulic connectivity. Configuration L_3 yields intermediate results, with balanced reductions between 31 % and 69 %, demonstrating the adaptability of the optimization algorithm to heterogeneous spatial conditions.

For the Cl^- ion, the optimized injection rates exhibit similar but slightly higher reduction percentages than those of the Mg^{2+} ion, consistent with chloride's higher mobility and lower reactivity in groundwater systems. In layout L_1, r-rates range from approximately 54 % to 76 %, showing strong reductions in injection intensity. Configuration L_2 presents a moderate pattern (r-rates between 32 % and 67 %), while L_3 produces the most consistent and balanced reduction profile (r-rates between 43 % and 75 %) across all injected locations. These outcomes confirm that chloride transport responds more sensitively to injected location configuration, but the DE-PDE algorithm successfully stabilizes the optimization by adjusting injection magnitudes according to local transport pathways and diffusion effects.

The computational performance remains steady for all three configurations, with nearly identical CPU times (around 3 hours 18–19 minutes), indicating that the parallel Differential Evolution algorithm maintains consistent efficiency regardless of geometric complexity.

Example 2. In the second experiment, our aim is to demonstrate the application of a multicomponent optimal control model to a practical scenario involving three interacting

pollutants, four injection points, and observation constraints at multiple locations within a groundwater domain. The example highlights how the structure of the fitness function, combined with the abatement cost functions, can significantly impact the optimal pollution management strategy.

We consider four pollution components $C_\beta = C_{CO_3^{2-}}$, and $C_\gamma = C_{Mg^{2+}}$, $C_{Ca^{2+}}$, C_{Cl^-}, where the aquifer contains $C_{CO_3^{2-}}$ inside and the other three components are injected on the specific top of the aquifer. We consider the domain $\Omega = [0,\ 1000m] \times [0,\ 20m]$ and the total simulation time period of 1 years. The left boundary value of water head is $h_{left} = 200m$ and the right boundary value of water head is $h_{right} = 20m$. The initial condition for water head is $h_0 = 20m$ as well as the initial value for pollution concentrations $C_{Ca^{2+}}$, $C_{Mg^{2+}}$, and C_{Cl^-} are zero and $C_{CO_3^{2-}} = 0.67mol/m^2$. We consider four injection rates $P_{\gamma l}$, $l = 1,\ 2,\ 3,\ 4$, in the four injected pieces, and the four observation locations of $O_{n_{ob}}$, $n_{ob} = 1,\ 2,\ 3,\ 4$, are placed deep in the aquifer to track the spread of the contaminant, as shown in Figure 3.1. The parameter values are given in Table 2.1. We simulate the flow of multicomponent contamination that occurs during the precipitation reaction.

The stoichiometry equation for magnesite growth is as follows

$$Mg^{2+} + Ca^{2+} + 2CO_3^{2-} \rightarrow CaMg(CO_3)_2(s).$$

The rate of growth for magnesium carbonate is $G_r = kS_eC_{Mg^{2+}}C_{Ca^{2+}}2C_{CO_3^{2+}}$. The kinetic control reaction: $R_{Mg^{2+}} = -v_{Mg^{2+}}G_r$, and $R_{CO_3^{2-}} = -v_{CO_3^{2-}}G_r$, where stoichiometric coefficients are $v_{Mg^{2+}} = v_{CO_3^{2-}} = 1$

.

The kinetic control reaction for CO_3^{2-} is presented as $S_{CO_3^{2-}}G_r$, while that for Ca^{2+} is represented as $S_{Ca^{2+}}G_r$ and Mg^{2+} is represented as $S_{Mg^{2+}}G_r$. The stoichiometric coefficients for the reaction involving CO_3^{2-}, Ca^{2+} and Mg^{2+} are both equal to 1, denoted as $S_{CO_3^{2-}}G_r$, $S_{Ca^{2+}}$ and $S_{Mg^{2+}}$. At a temperature of 25^0C, the solubility constant of $MgCO_3$ is 6.82×10^{-6}.

The decretize cost function f_2 given below:

$$f_2(\mathbf{P}_{\gamma_l}) = \sum_{l=1}^{n_s} \sum_{\gamma=n_e+1}^{n_c} \sum_{t=0}^{T} \omega_2 \left(b_{1,l} W_{\gamma_l}^{b_{2,l}} + b_{3,l} W_{\gamma_l}^{b_{2,l}} r_{\gamma_l}^{b_{4,l}} \right) dt, \tag{3.30}$$

where the influent rates, commonly known as reduction rates(r-rate), are defined by

$$r_{\gamma_l} = \frac{P_{\gamma_l}^{max} - P_{\gamma_l}}{P_{\gamma_l}^{max}}. \tag{3.31}$$

and the coefficients values of the cost function listed in Table 4.4.

Table 3.4: The values of the cost function coefficients.

Coefficient	b_1	b_2	b_3	b_4	b_5	b_6
Value	0.90	0.75	3.50	5.00	20.00	0.75

We consider the four injection locations on the top boundary of the left half domain. They are located between [250m 280m], [310m, 340m], [370m, 400m], and [430m, 460m] respectively. We consider the injection rates range at four different injection locations for $P_{Mg_l^{2+}}$, [0.1 0.9],$P_{Ca_l^{2+}}$, [0.1 0.9], and for $P_{Cl_l^-}$ [0.1 0.9], $l = 1, 2, 3, 4$. We consider the pollutions are injected for 360 days. AIR means actual injection rate and Opt means optimal injection rate. Four discrete areas where the pollution concentrations are somewhat constrained need to be protected. In this instance, the particular places are considered as a few points which serve as observation locations. We consider the four observation points are $O_1 = (700, 18.5)$, $O_2 = (700, 16)$, $O_3 = (800, 18.5)$ and $O_4 = (800, 16)$. We consider AIR at the observation location to find $C_{\gamma_s}^{ob}$ with the noise $\zeta = 0.1$. We use the spatial step sizes are $\Delta x = \Delta y = 1m$ and the time step size as $\Delta t = 1day$. The parameter values are given in Table 2.1.

Table 3.5 presents the numerical optimization results for 1, 5, 10, 20, and 25 processors. A Population size of 100, a maximum of 350 generations and a tolerance of 10^{+2} are taken. The results by the parallel DE-PDE clearly demonstrate that the parallel algorithm maintains numerical robustness and solution stability across all processor configurations. The optimal

injection rates $P_{Mg_l^{2+}}$, $P_{Ca_l^{2+}}$ and $P_{Cl_l^-}$ at the four injection locations remain consistent with their actual injection rates, and the r-rates vary from 60-75% across the 1–25 processor runs. The objective function values are also very consistent.

Table 3.5: Paralle DE-PDE Performance Summary for the objective function $f_1 + f_2$.

γ	P_{γ_l}	AIR	Number of Processors				
			1	5	10	20	25
			Opt	*Opt*	*Opt*	*Opt*	*Opt*
Mg^{2+}	P_{γ_1}	0.10	0.289	0.312	0.275	0.268	0.285
	P_{γ_2}	0.10	0.310	0.240	0.326	0.364	0.370
	P_{γ_3}	0.10	0.209	0.320	0.259	0.274	0.288
	P_{γ_4}	0.10	0.270	0.261	0.300	0.253	0.318
Ca^{2+}	P_{γ_1}	0.10	0.322	0.260	0.219	0.288	0.308
	P_{γ_2}	0.10	0.261	0.284	0.341	0.268	0.298
	P_{γ_3}	0.10	0.281	0.286	0.267	0.303	0.296
	P_{γ_4}	0.10	0.282	0.374	0.266	0.269	0.301
Cl^-	P_{γ_1}	0.10	0.290	0.289	0.344	0.304	0.261
	P_{γ_2}	0.10	0.311	0.269	0.349	0.313	0.214
	P_{γ_3}	0.10	0.299	0.339	0.249	0.251	0.286
	P_{γ_4}	0.10	0.278	0.293	0.284	0.329	0.273
Time :			$81h\ 56m$	$18h\ 33m$	$9h\ 48m$	$6h\ 49m$	$6h\ 27m$
Obj.	val.:		$3.67e+3$	$3.68e+3$	$3.69e+3$	$3.67e+3$	$3.68e+3$

Figure 3.3a presents the variation of time reduction (%) with respect to the number of processors used in the parallel DE-PDE algorithm. The curve demonstrates a clear, monotonic increase, indicating that the computational time decreases significantly as more processors participate in the simulation. Starting from a single-processor baseline, the total runtime is reduced by nearly 77.35% with five processors, 88% with ten processors, and reaches approximately 92.11% reduction with twenty-five processors. Though we get a little better time reduction for f_1 that shown in Figure 3.2a from 82-94.76 %, but this strong time reduction confirms that the MPI-based population-level efficiency of the DE-PDE algorithm. Figure 3.3b illustrates the speedup achieved by the parallel DE–PDE solver as a function of the number of processors. The speedup curve closely follows an ideal linear trend up to approximately ten processors, where the speedup value reaches around 8.36, nearly

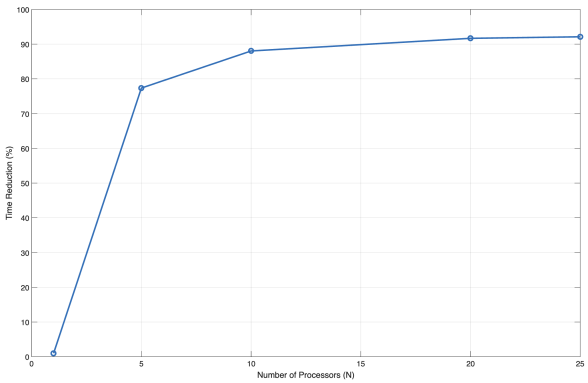

(a) Parallel DE-PDE time reduction performance metrics.

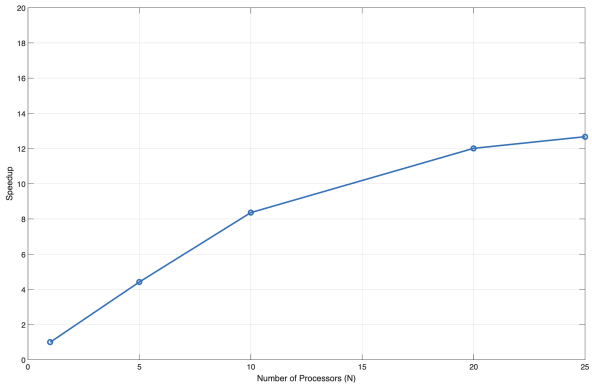

(b) Parallel DE-PDE speedup performance metrics.

Figure 3.3: Parallel DE-PDE performance metrics: (a) Time reduction, (b) Speedup.

equivalent to the number of processors employed. This near-linear growth confirms that the computational tasks are evenly distributed and efficiently executed in parallel. For parallel processors 20 and 25, the speedup are comperatively slow than parallel processors 5 and 10. We get better speedup for the objective function f_1 than $f_1 + f_2$. The achieved speedup remains remarkably high, demonstrating that the proposed parallelization offers efficient scalability and effective load balancing. Further, Figures 3.3a, 3.3b show the proposed parallel DE–PDE solver achieves near-linear scalability, significant runtime reduction, and high computational efficiency while maintaining stable optimization accuracy.

Table 3.6 presents the optimal injection rates (Opt) for each pollutant at four injection locations and the corresponding reduction rates (r-rate %) for two different left boundary hydraulic heads, which represent the achieved fractional reduction relative to maximum permissible injection levels. We use 10 processors to produce Table 3.6. We consider a Population size of 50, a maximum of 250 generations and a tolerance of 10^2. The objective function considered here is $f_1 + f_2$, which minimizes the deviation between simulated and permissible concentrations at observation points as well as the abatement cost. We consider the noise $\zeta = 0.1$. We consider the four injection locations on the top boundary of the left half domain.They are located between $[250m\, 280m]$, $[310m, 340m]$, $[370m, 400m]$, and

[430m, 460m] respectively. At four different injection locations P_{γ_1}, P_{γ_2}, P_{γ_3} and P_{γ_4}, we consider two group of injection rate range. For the first group, for all injected locations for all components, we consider the injection rate range [0.1 0.9] and the AIR is 0.1. For second group of injection rate range, we consider [0.04 0.4], [0.06 0.6], and [0.08 0.8], for Mg^{2+}, Ca^{2+} and Cl^{-} ions and there corresponding AIR are 0.07, 0.09, and 0.40 respectively. We consider the four observation points are (700, 18.5), (700, 16), (800, 18.5) and (800, 16). We consider AIR at the observation location to find $C^{*}_{\gamma_s}$. We consider the pollutions are injected for 360 days. We use the spatial step sizes of $\Delta x = \Delta y = 1m$ and the time step size of $\Delta t = 1day$. Then, we find the optimal injection rates at four different injection locations and find the r-rates. In Table 3.6, we consider two different left boundary hydraulic heads $50m$ and $300m$ while the right boundary hydraulic head is $20m$ in each case.

For $P_{Mg_l^{2+}}$, Table 3.6 shows that optimal injections strongly depend both on the hydraulic gradient and on the injection-rate group. Under the lower head of $50m$, $P_{Mg_l^{2+}}$ injections from the wider range [0.1 0.9] often settle in the mid-to-upper region of the interval, while the narrower ranges [0.04 0.4], [0.06 0.6], and [0.08 0.8] leads the optimizer to push values close to the upper bound, because we consider AIR 0.1 as the lower limit of range for wider range and AIR in the middle of the narrow ranges. For both injection rate range groups, for all pollutant γ_l, the fourth injection location ($l = 4$) injected less pollution due to close to the observation locations. These higher injection levels are feasible because slower flow and precipitation reduce $C_{Mg_l^{2+}}$ accumulation at monitoring points. When the left boundary head increases to $300m$, however, both groups experience substantial downward shifts in optimal injection, with reduction rates typically exceeding 50–60%. Even within the tighter range, the optimizer reduces $P_{Mg_l^{2+}}$ sharply, demonstrating that fast transport dominates and forces conservative injection regardless of the allowed interval.

$P_{Ca_l^{2+}}$ displays the clearest influence of the two injection-rate groups. At $50m$ head, injections from the broader [0.1 0.9] range frequently reach very high values, and even the narrower

[0.04 0.4], [0.06 0.6], and [0.08 0.8] ranges drive the optimizer to use injection levels close to the upper limit, producing very small reduction rates. This behaviour reflects $P_{Ca_l^{2+}}$ strong participation in precipitation reactions, which buffer concentration buildup during slow flow. Under the high-head condition of $300m$, both groups exhibit pronounced declines in optimal injection, with reduction rates commonly in the 60–70% range. The narrower ranges moderate the absolute magnitude of reductions but do not change the overall trend: rapid transport forces strong injection cuts even for a highly reactive ion like Ca^{2+}.

$P_{Cl_l^-}$ shows the most restrictive behaviour across both injection-rate groups due to its high mobility and limited participation in reactions. In the $50m$ head case, the optimizer already suppresses $P_{C_l^-}$ injections near the lower bound for the [0.1 0.9] group, while the narrower groups permit somewhat higher values but still reflect tight control. Under the $300m$ head, both groups experience large reductions, typically producing r-rates in the 60–80% range. Importantly, the two groups reveal that even when $P_{Cl_l^-}$ is given a reduced feasible interval, the optimizer continues to choose low values because $C_{Cl_l^-}$ rapidly reaches observation locations under both flow conditions. Thus, $C_{Cl_l^-}$ remains the most constrained pollutant, and the injection-rate group influences the numerical value of the optimum but not the underlying need for strong reduction.

Overall, the combined results for $P_{Mg_l^{2+}}$, $P_{Ca_l^{2+}}$ and $P_{Cl_l^-}$ in Table 3.6 highlight the strong interplay between hydraulic conditions, injection-rate bounds, and pollutant-specific transport and reaction behavior in shaping optimal pollution control strategies. Under the weak-flow scenario, the optimizer utilizes the upper portions of the injection intervals more freely—especially for the reactive ions Mg^{2+} and Ca^{2+}, because slower transport and precipitation reactions help maintain concentrations within acceptable limits. However, as the hydraulic gradient increases, the system becomes far more sensitive, and the optimizer consistently imposes substantial reductions across all pollutant and injection-rate groups to prevent rapid contaminant breakthrough at the observation locations.

Table 3.6: Numerical simulations-optimization results of Mg^{2+}, Ca^{2+} and Cl^{-} injection rates for different hydraulic heads for the objective function $f_1 + f_2$ evaluated with 10 parallel processors.

γ	$P_{\gamma l}$	IR range	AIR	$h_{left} = 50m$ Opt	$h_{left} = 50m$ r-rate (%)	$h_{left} = 300m$ Opt	$h_{left} = 300m$ r-rate (%)
Mg^{2+}	P_{γ_1}	[0.1 0.9]	0.10	0.740	17.74	0.305	66.09
		[0.04 0.4]	0.07	0.361	09.75	0.163	59.25
	P_{γ_2}	[0.1 0.9]	0.10	0.613	31.88	0.419	53.44
		[0.06 0.6]	0.09	0.570	05.00	0.257	57.17
	P_{γ_3}	[0.1 0.9]	0.10	0.620	31.07	0.455	49.44
		[0.08 0.8]	0.10	0.600	25.00	0.373	53.38
	P_{γ_4}	[0.1 0.9]	0.10	0.267	70.03	0.366	59.36
		[0.1 0.9]	0.40	0.418	53.56	0.416	53.78
Ca^{2+}	P_{γ_1}	[0.1 0.9]	0.10	0.812	09.75	0.300	66.61
		[0.04 0.4]	0.07	0.393	01.75	0.156	61.00
	P_{γ_2}	[0.1 0.9]	0.10	0.602	33.14	0.326	63.81
		[0.06 0.6]	0.09	0.553	07.83	0.445	25.83
	P_{γ_3}	[0.1 0.9]	0.10	0.507	43.70	0.398	55.80
		[0.08 0.8]	0.10	0.600	25.00	0.308	61.50
	P_{γ_4}	[0.1 0.9]	0.10	0.253	71.89	0.317	64.82
		[0.1 0.9]	0.40	0.417	53.67	0.377	58.11
Cl^{-}	P_{γ_1}	[0.1 0.9]	0.10	0.717	20.29	0.282	68.64
		[0.04 0.4]	0.07	0.400	00.00	0.209	47.75
	P_{γ_2}	[0.1 0.9]	0.10	0.574	36.26	0.350	61.08
		[0.06 0.6]	0.09	0.569	05.17	0.242	59.67
	P_{γ_3}	[0.1 0.9]	0.10	0.618	31.30	0.336	62.63
		[0.08 0.8]	0.10	0.563	29.63	0.331	58.63
	P_{γ_4}	[0.1 0.9]	0.10	0.240	73.31	0.287	68.08
		[0.1 0.9]	0.40	0.413	54.11	0.312	65.33
Time :				$7h\ 55m$		$7h\ 58m$	

Table 3.7 presents the numerical optimization results for two different case of Reduction Rate Exponent b_4. For groundwater contamination with four interacting pollutants CO_3^{2-}, Mg^{2+}, Ca^{2+} and Cl^{-} ions in a four-injection configuration. We use 10 processors to produce Table 3.7. We consider a Population size of 50, a maximum of 250 generations and a tolerance of 10^2. The objective function considered here is $f_1 + f_2$, which minimizes the deviation between simulated and permissible concentrations at observation points as well as

the abatement cost. We consider the noise $\zeta = 0.1$. The table reports the optimal injection rates (Opt) for each pollutant at four injection locations and the corresponding reduction rates (r-rate %), which represent the achieved fractional reduction relative to maximum permissible injection levels. At four different injection locations P_{γ_1}, P_{γ_2}, P_{γ_3} and P_{γ_4}, we consider two group of injection rate range. For the first group, for all injected locations for all components, we consider the injection rate range [0.1 0.9] and the AIR is 0.1. For second group of injection rate range, we consider [0.08 0.8], [0.08 0.8], [0.1 0.9], and [0.1 0.9] for Mg^{2+}, Ca^{2+} and Cl^{-} ions and there corresponding AIR are 0.10, 0.10, 0.30 and 0.30 respectively. We consider the four observation points are (700, 18.5), (700, 16), (800, 18.5) and (800, 16). We consider AIR at the observation location to find $C^*_{\gamma_s}$. We consider the pollutions are injected for 360 days. We use the spatial step sizes of $\Delta x = \Delta y = 1m$ and the time step size of $\Delta t = 1day$. Then, we find the optimal injection rates at four different injection locations and find the r-rates. In Table 3.7, we present two different cases of the reduction rate exponent, where case-I is for $b_4 = 2.0$ and case-II is for $b_4 = 8.0$.

For $P_{Mg_l^{2+}}$, Table 3.7 shows that both the reduction rate exponent b_4 and the chosen injection-rate group strongly influence the optimized injection behaviour. Under the wider range [0.1 0.9] with a low AIR of 0.10 and 0.30, the optimizer has considerable flexibility, and with $b_4 = 2.0$ it often selects lower injection rates with higher r-rates because reductions are not overly penalized. In contrast, under the narrower range [0.08 0.8], the optimizer tends to place the solution closer to the upper bound, especially when $b_4 = 8.0$, because the steep cost curve makes any significant reduction prohibitively expensive. As a result, the combination of a tight feasible interval and a large exponent forces the optimizer toward much higher injection values and substantially lower reduction percentages. Thus, for $P_{Mg_l^{2+}}$, both the allowable injection bounds and the curvature of the abatement cost function jointly determine how aggressively the system can reduce injections.

$P_{Ca_l^{2+}}$ follows the same general trend but exhibits additional nuances due to its strong

role in the precipitation reaction. With the broader [0.1 0.9] interval and AIR = 0.10 or 0.30, the optimizer can take advantage of $P_{Mg_l^{2+}}$ natural attenuation, especially when $b_4 = 2.0$, producing moderate reductions without incurring excessive cost. However, when the injection rate group is tightened to [0.08 0.8], the feasible range restricts how much downward adjustment is possible, and the transition to a large exponent ($b_4 = 8.0$) further discourages reductions by dramatically inflating abatement cost at higher r-rates. Consequently, $P_{Ca_l^{2+}}$ injections rise noticeably under Case II, regardless of its reactive benefits. The combined influence of the narrow interval and steep cost structure makes aggressive $P_{Ca_l^{2+}}$ reduction infeasible, highlighting the dominant role of economic penalties in shaping control strategies. $P_{Cl_l^-}$, being highly mobile and weakly reactive, shows the strongest combined sensitivity to both injection-rate groups and cost-function curvature. Under the first group [0.1 0.9] with AIR = 0.10 or 0.30, the optimizer imposes substantial reductions when $b_4 = 2.0$, producing low optimal injection values to prevent rapid transport toward observation points. However, under the second group—where $P_{Cl_l^-}$ may have a higher AIR or a modified bound, the optimizer's flexibility diminishes, and the steep $b_4 = 8.0$ penalty makes large reductions economically prohibitive. As a result, $P_{Cl_l^-}$ injections increase sharply and r-rates drop across all injection locations. This pattern demonstrates that when a pollutant is both highly mobile and assigned a steep abatement-cost exponent, the optimizer prioritizes cost avoidance over aggressive reduction, even if transport physics would favour stronger suppression.

Overall, the results in Table 3.7 clearly demonstrate that the reduction-rate exponent b_4 and the chosen injection-rate group play decisive roles in shaping the optimal injection strategies for $P_{Mg_l^{2+}}$,$P_{Ca_l^{2+}}$ and $P_{Cl_l^-}$. When $b_4 = 2.0$, the moderate growth of abatement cost allows the optimizer to impose substantial reductions across all species, especially within the wider injection-rate intervals, leading to lower optimal injections and higher r-rates. In contrast, when $b_4 = 8.0$, the abatement cost becomes extremely steep, making high reductions prohibitively expensive and pushing the optimizer toward much higher injection values with

significantly reduced r-rates.

Table 3.7: Numerical simulations-optimization results of Mg^{2+}, Ca^{2+} and Cl^- injection rates for different cost coefficient penalty for the objective function $f_1 + f_2$ evaluated with 10 parallel processors.

γ	P_{γ_l}	IR range	AIR	$Case-I$ Opt	$Case-I$ r-rate (%)	$Case-II$ Opt	$Case-II$ r-rate (%)
Mg^{2+}	P_{γ_1}	[0.1 0.9]	0.10	0.370	58.87	0.193	78.55
		[0.08 0.8]	0.10	0.680	15.00	0.475	40.63
	P_{γ_2}	[0.1 0.9]	0.10	0.323	64.11	0.229	74.54
		[0.08 0.8]	0.10	0.578	27.75	0.618	22.75
	P_{γ_3}	[0.1 0.9]	0.10	0.314	65.15	0.260	71.09
		[0.1 0.9]	0.30	0.617	31.44	0.385	57.22
	P_{γ_4}	[0.1 0.9]	0.10	0.100	88.89	0.135	85.01
		[0.1 0.9]	0.30	0.594	34.00	0.383	57.44
Ca^{2+}	P_{γ_1}	[0.1 0.9]	0.10	0.405	54.52	0.278	69.12
		[0.08 0.8]	0.10	0.700	12.50	0.367	54.13
	P_{γ_2}	[0.1 0.9]	0.10	0.168	81.28	0.188	79.13
		[0.08 0.8]	0.10	0.583	27.13	0.248	69.00
	P_{γ_3}	[0.1 0.9]	0.10	0.100	89.89	0.216	75.98
		[0.1 0.9]	0.30	0.661	26.56	0.386	57.11
	P_{γ_4}	[0.1 0.9]	0.10	0.259	71.18	0.200	77.78
		[0.1 0.9]	0.30	0.575	36.11	0.316	64.89
Cl^-	P_{γ_1}	[0.1 0.9]	0.10	0.379	57.81	0.269	70.03
		[0.08 0.8]	0.10	0.648	19.00	0.271	66.13
	P_{γ_2}	[0.1 0.9]	0.10	0.100	88.89	0.134	85.11
		[0.08 0.8]	0.10	0.664	17.00	0.368	54.00
	P_{γ_3}	[0.1 0.9]	0.10	0.174	80.65	0.216	75.99
		[0.1 0.9]	0.30	0.685	23.89	0.350	61.11
	P_{γ_4}	[0.1 0.9]	0.10	0.269	70.04	0.253	71.90
		[0.1 0.9]	0.30	0.662	26.44	0.480	46.67
Time:				$7h\ 7m$		$7h\ 6m$	

Table 3.8 presents the numerical optimization results for different objective functions f_1, f_1+f_2 and f_1+f_3 by the parallel DE-PDE algorithm for the multicomponent PDE-constrained optimal control model to groundwater contamination with four interacting pollutants CO_3^{2-}, Mg^{2+}, Ca^{2+} and Cl^- in a four-injection configuration. We use 10 processors to produce Table 3.8. A Population size of 50, a maximum of 150 generations and a tolerance 10^{-4} are

taken for f_1 and tolerance 10^{-2} for $f_1 + f_2$ and $f_1 + f_3$. We use 10 parallel processors to produce optimal values. The table reports the optimal injection rates (Opt) for each species at four injection locations and the corresponding reduction rates (r-rate %), which represent the achieved fractional reduction relative to maximum permissible injection levels. At four different injection locations P_{γ_1}, P_{γ_2}, P_{γ_3} and P_{γ_4}, we consider the injection rates range is [0.1 0.9] and AIR is 0.1 for Mg^{2+}, Ca^{2+}, and Cl^- . We consider the four observation points are (700, 18.5), (700, 16), (800, 18.5) and (800, 16). We consider AIR at the observation location to find $C^*_{\gamma_s}$. We consider the noise $\zeta = 0.05$. We consider the pollutions are injected for 360 days. We use the spatial step sizes of $\Delta x = \Delta y = 1m$ and the time step size of $\Delta t = 1day$. Then, we find the optimal injection rates at four different injection locations and find the r-rates.

On the other hand, the specified piecewise abatement cost function f_2' is considered

$$f_2'(\mathbf{P}_{\gamma_l}) = \sum_{l=1}^{n_s} \sum_{\gamma=n_e+1}^{n_c} \sum_{t=0}^{T} \omega_2 A'_{\gamma_l}(r_{\gamma_l}), \qquad \forall \quad r. \tag{3.32}$$

$$A'_{\gamma_l}(r_{\gamma_l}) = \begin{cases} \left(b_{1,l} W_{\gamma_l}^{b_{2,l}} + b_{3,l} W_{\gamma_l}^{b_{2,l}} r_{\gamma_l}^{b_{4,l}}\right), & for \quad r < r_c, \\ \left(b_{1,l} W_{\gamma_l}^{b_{2,l}} + b_{3,l} W_{\gamma_l}^{b_{2,l}} r_{\gamma_l}^{b_{4,l}} + b_{5,l} W_{\gamma_l}^{b_{2,l}} \left((r - r_c)_{\gamma_l}^{b_{6,l}}\right)\right), & for \quad r \geq r_c. \end{cases}$$

Table 3.8 shows that the optimal $P_{Mg_l^{2+}}$ are highly sensitive to the choice of objective function. Under the tracking only objective f_1, the optimizer consistently selects the minimum permissible injection value of 0.100 at two of the four injection locations, and at the other two locations, injection rates are very close to AIR, yielding very high reduction rates between 82% and 89%. This reflects an aggressive minimization of concentration deviations, as the absence of a cost penalty encourages strong reductions. When the standard abatement cost function f_2 is included, the optimal injections rise substantially to values in the range 0.612 to 0.722, and the corresponding reduction rates fall markedly to $19 - 32\%$. This demonstrates the influence of economic penalties, which discourage excessive reductions and force a balance

Table 3.8: Numerical simulations-optimization results of Mg^{2+}, Ca^{2+} and Cl^{-} injection rates for different cost coefficient penalties for the objective function f_1,f_1+f_2, and f_1+f_3 evaluated with 10 parallel processors.

γ	P_{γ_l}	AIR	f_1		f_1+f_2		f_1+f_2'	
			Opt	r-rate (%)	Opt	r-rate (%)	Opt	r-rate (%)
Mg^{2+}	P_{γ_1}	0.10	0.100	88.89	0.658	26.86	0.446	50.50
	P_{γ_2}	0.10	0.152	83.07	0.722	19.81	0.368	59.16
	P_{γ_3}	0.10	0.162	82.00	0.612	31.96	0.419	53.48
	P_{γ_4}	0.10	0.100	88.89	0.638	29.17	0.256	71.52
Ca^{2+}	P_{γ_1}	0.10	0.100	88.89	0.547	39.22	0.222	75.32
	P_{γ_2}	0.10	0.120	86.68	0.551	38.74	0.353	60.74
	P_{γ_3}	0.10	0.181	79.83	0.646	28.19	0.464	48.46
	P_{γ_4}	0.10	0.100	88.89	0.565	37.19	0.371	58.81
Cl^{-}	P_{γ_1}	0.10	0.100	88.89	0.535	40.57	0.386	57.10
	P_{γ_2}	0.10	0.130	85.52	0.610	32.18	0.279	69.04
	P_{γ_3}	0.10	0.183	79.69	0.751	16.60	0.524	41.76
	P_{γ_4}	0.10	0.101	88.79	0.611	32.10	0.401	55.45
Time:			$3h\ 54m$		$4h\ 2m$		$4h\ 35m$	

between environmental performance and cost. Under the piecewise cost function $f_1 + f_2'$, $P_{Mg_l^{2+}}$ falls between the two previous regimes, with optimal values of 0.256 to 0.446 and reduction rates of 50% to 72%. The f_3' structure therefore yields a moderated compromise that allows meaningful reduction while avoiding the extreme penalties imposed by f_2.

The $P_{Ca_l^{2+}}$ results in Table 3.8 follow the same general trend as $P_{Mg_l^{2+}}$, but with distinct behavior arising from $P_{Ca_l^{2+}}$ strong involvement in the precipitation reaction. Under f_1, the optimizer again drives the injection rates to the lower bound of 0.100 at two locations and to similarly low levels at the remaining sites, producing reduction rates of 80%–89%. When the abatement cost f_2 is introduced, injection rates increase noticeably to the range 0.547 to 0.646, accompanied by reduced r-rates of 28% to 39%. These values are slightly lower than their $P_{Mg_l^{2+}}$ counterparts, indicating that the optimizer tolerates somewhat higher $P_{Ca_l^{2+}}$ injections because reactions naturally attenuate its concentration. Under the decreasing cost function f_3, optimal $P_{Ca_l^{2+}}$ injections shift to the intermediate range 0.222 to 0.464, with r-rates between 48% and 75%. Thus, f_3' promotes substantial but not extreme reductions,

reflecting a balanced interaction between concentration tracking and the moderated economic penalty.

$P_{Cl_l^-}$ displays the most pronounced sensitivity to the objective function due to its weak reactivity and high mobility. Under f_1, optimal injection rates remain close to the lower bound (0.100–0.183), resulting in high reduction rates of 79%–89%, which reflects the need to strongly suppress chloride transport when reductions are cost-free. When the abatement cost f_2 is included, the optimizer relaxes these reductions substantially, increasing optimal injections to 0.535 to 0.751 and decreasing r-rates to $16-41\%$. This highlights the prohibitive cost of aggressive reduction for a highly mobile species. Under the piecewise cost function f_2', chloride injection rates again fall between the extremes, taking values of 0.279 to 0.524 with r-rates of 41% to 69%. The f_2' formulation therefore yields a tempered strategy that allows for meaningful reduction while avoiding the severe economic penalty associated with strong suppression under f_2. Overall, $P_{Cl_l^-}$ remains the most constrained contaminant, with the objective function exerting dominant control over its optimal injection patterns.

Overall, the results presented in Table 3.8 clearly demonstrate that the structure of the objective function has a profound influence on the optimal injection strategy for $P_{Mg_l^{2+}}$, $P_{Ca_l^{2+}}$ and $P_{Cl_l^-}$. When the optimization relies solely on the tracking objective f_1, the algorithm consistently drives the injection rates toward their lower bounds, resulting in very high reduction rates across all species. This outcome reflects the fact that, in the absence of an economic penalty, the optimizer favours aggressive suppression to minimize concentration mismatches at observation locations. In contrast, the introduction of the standard abatement cost function f_2 significantly alters this behaviour, penalizing strong reductions and leading to much higher optimal injection values with substantially lower r-rates. The piecewise abatement cost function f_2' produces intermediate results, offering a balanced compromise between reduction effort and cost by allowing meaningful reductions in injection without imposing the steep penalties of f_2. Together, these findings highlight

the critical role of cost-function design in shaping groundwater contamination management decisions and demonstrate how economic considerations can strongly modulate physically driven optimal control solutions.

Example 3. In the third experiment, our aim is to demonstrate the application of a multicomponent optimal control model to a practical scenario involving four interacting pollutants, two injection locations, and observation constraints at multiple locations within a groundwater domain. The example emphasizes how the structure of the fitness function f_1 and abatement cost functions f_2 and f_2' can substantially influence the optimal pollution management strategy.

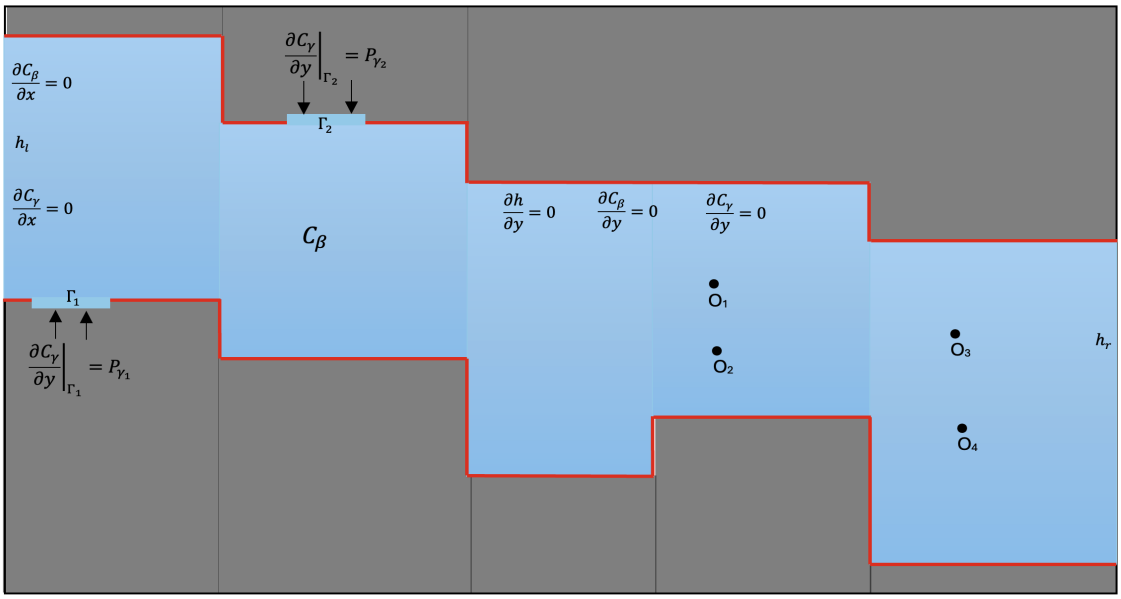

Figure 3.4: Hypothetical vertical aquifer.

We consider a conceptual aquifer whose shape closely resembles that of the real aquifer which is presented in Fig. 3.4. We consider the domain $\Omega = [0,\ 1000m] \times [0,\ 100m]$ and the total simulation time period of 360 days. Additionally, we have a discontinuous pollution-injection process that occurs at specific boundary locations of the domain, as specified by the injected locations. We consider injection pollution for the first six months and no injection pollution for the last six months. The left boundary value of water head is $h_{left} = 150m$ and the

right boundary value of water head is $h_{right} = 20m$. We consider the same contamination components and precipitation chemical reaction as in Example 2. The initial condition for water head is $h_0 = 20m$ as well as the initial value for pollution concentrations $C_{Ca^{2+}}$, $C_{Mg^{2+}}$, C_{Cl^-} are zero and $C_{CO_3^2} = 0.6\, mol/m^2$. We consider two injection rates P_{γ_l}, $l = 1, 2$, in the two injected pieces, and the four observation locations of $O_{n_{ob}}$, $n_{ob} = 1, 2, 3, 4$, are placed deep in the aquifer to track the spread of the contaminant, as shown in Fig. 3.4.

Table 3.9: The case description.

	Injected locations	Observed locations	
Case-I	$P_{\gamma_1} : ([30m\ 130m],\ 50m)$	$O_1 : (300m,\ 75m)$	$O_2 : (300m,\ 50m)$
	$P_{\gamma_2} : ([30m\ 130m],\ 95m)$	$O_3 : (350m,\ 75m)$	$O_4 : (350m,\ 50m)$
Case-II	$P_{\gamma_1} : ([30m\ 130m],\ 50m)$	$O_1 : (450m,\ 50m)$	$O_2 : (450m,\ 45m)$
	$P_{\gamma_2} : ([250m\ 350m],\ 40m)$	$O_3 : (480m,\ 50m)$	$O_4 : (480m,\ 45m)$
Case-III	$P_{\gamma_1} : ([30m\ 130m],\ 50m)$	$O_1 : (200m,\ 60m)$	$O_2 : (200m,\ 50m)$
	$P_{\gamma_2} : ([470m\ 570m],\ 20m)$	$O_3 : (670m,\ 40m)$	$O_4 : (670m,\ 30m)$

In Case I, the injection and observation points are spatially close, producing strong hydraulic coupling. The optimizer chooses Opt values near the lower end of each IR range of [0.1 0.9] for the $P_{Mg_l^{2+}}$, $P_{Ca_l^{2+}}$, and $P_{Cl_l^-}$ and resulting in high reduction rates of roughly 70–90 %. But when we choose AIR as the mid value of the IR range, the Opt is around its AIR. The corresponding AIR values are modest but sufficient, indicating efficient transmission of injected solutes through the aquifer. These results confirm that in short-path configurations, minimal injection achieves the target concentrations because advective transport dominates and dispersion losses are negligible. Computationally, this regime is the most energy-efficient, with high r-rates reflecting strong abatement efficiency.

Table 3.10 presents the numerical optimization results for different injected locations by the parallel DE-PDE algorithm for the multicomponent PDE-constrained optimal control model for groundwater contamination with four interacting pollutants CO_3^{2-}, Mg^{2+}, Ca^{2+} and Cl^- ions in a two-injection configuration. We use 5 processors to produce Table 3.10. The objective function considered here is solely f_1, which minimizes the deviation between simulated and

permissible concentrations at observation points. We consider the noise $\zeta = 0.2$. The table reports the optimal injection rates (Opt) for each species at two injection locations and the corresponding reduction rates (r-rate %), which represent the achieved fractional reduction relative to maximum permissible injection levels. We consider the injection rates range at two different injection locations P_{γ_1} [0.1 0.9] and [0.05 0.5] for Mg^{2+}, [0.1 0.9], and [0.1 0.9] for Ca^{2+} and [0.1 0.9], and [0.09 0.9] for Cl^{-} as well as P_{γ_2} [0.1 0.9], and [0.08 0.8] for Mg^{2+}, [0.1 0.9], and [0.09 0.9] for Ca^{2+} and [0.1 0.9], and [0.06 0.6] for Cl^{-}. We consider the pollutions are injected for 360 days. Then, we find the optimal injection rates at two different injection locations and find the r-rates. The injection locations and observation locations for three different cases are given below in Table 3.9. The comparison among Case I, Case II, and Case III illustrates how the DE-PDE algorithm balances pollutant control, physical transport, and constraint satisfaction.

Table 3.10: Numerical simulations-optimization results of Mg^{2+}, Ca^{2+} and Cl^{-} injection rates for the objective function f_1 evaluated with 10 parallel processors.

	P_{γ_l}	IR range	AIR	*Case I*		*Case II*		*Case III*	
				Opt	r-rate (%)	Opt	r-rate (%)	Opt	r-rate (%)
Mg^{2+}	P_{γ_1}	[0.1 0.9]	0.10	0.240	73.33	0.189	79.00	0.242	73.11
		[0.05 0.5]	0.07	0.105	79.00	0.109	78.20	0.103	79.40
	P_{γ_2}	[0.1 0.9]	0.10	0.100	88.89	0.231	74.33	0.212	76.44
		[0.08 0.8]	0.09	0.117	85.38	0.124	84.50	0.138	82.75
Ca^{2+}	P_{γ_1}	[0.1 0.9]	0.10	0.224	75.11	0.232	74.35	0.242	73.11
		[0.1 0.9]	0.20	0.299	66.78	0.279	69.00	0.300	66.67
	P_{γ_2}	[0.1 0.9]	0.10	0.121	86.56	0.232	74.22	0.204	77.33
		[0.09 0.9]	0.10	0.090	90.00	0.168	81.33	0.107	88.11
Cl^{-}	P_{γ_1}	[0.1 0.9]	0.10	0.225	75.00	0.246	72.67	0.226	74.89
		[0.09 0.9]	0.10	0.179	80.11	0.177	80.33	0.180	80.00
	P_{γ_2}	[0.1 0.9]	0.10	0.265	70.56	0.220	75.56	0.359	60.11
		[0.06 0.6]	0.07	0.119	80.17	0.098	83.67	0.116	80.67
Time:				$20h\ 56m$		$20h\ 55m$		$20h\ 54m$	

We consider intermediate separation in Case II, i.e. when injection and observation wells are farther apart, the optimizer compensates by increasing Opt values within each IR

range of [0.1 0.9]—for instance, Mg^{2+} ($P_{Mg_1^{2+}} = 0.189$; $P_{Mg_2^{2+}} = 0.231$), Ca^{2+} ($P_{Ca_1^{2+}} = 0.232$; $P_{Ca_2^{2+}} = 0.168$), and Cl^- ($P_{Cl_1^-} = 0.246$; $P_{Cl_2^-} = 0.220$) while r-rates drop to 70˘80 %. On the other hand, the optimal values for different IR ranges in different injected locations show little fluctuation, which follow the same trajectory with a fixed IR range. The opt values in this case are slightly lower than in Case I, despite the higher Opt, showing that dispersion and partial attenuation limit how much of the injected concentration reaches the observation points. This behaviour illustrates the optimizer's ability to adjust control intensity to offset transport inefficiencies. The shift of Opt toward the mid-range of IR demonstrates that the algorithm is not saturating the control limits but rather finding balanced, physically meaningful injection profiles.

In Case III, the most complex configuration, with widely separated wells and anisotropic flow paths, Table 3.10 shows a mixture of high and low Opt values. The reduction rates vary between 60% and 80%, and opt values at observation points remain moderate, indicating partial breakthrough at the injected locations. These variations suggest that one injection zone operates more effectively than the other. The DE-PDE optimizer dynamically adapts each control variable, pushing some Opt values closer to the upper IR limit to sustain influence in hydraulically distant regions while keeping others near the lower limit to avoid over-injection downstream.

Table 3.11: Numerical simulations-optimization results of Mg^{2+}, Ca^{2+} and Cl^- injection rates for the objective function $f_1 + f_3$ evaluated with 10 parallel processors.

			$6^{th}Month$		$8^{th}Month$		$12^{th}Month$	
γ	P_{γ_l}	AIR	Opt	r-rate (%)	Opt	r-rate (%)		r-rate (%)
Mg^{2+}	P_{γ_1}	0.10	0.648	19.00	0.156	82.67	0.150	81.25
	P_{γ_2}	0.25	0.373	58.56	0.368	59.11	0.756	16.00
Ca^{2+}	P_{γ_1}	0.08	0.573	18.14	0.119	83.00	0.119	83.00
	P_{γ_2}	0.10	0.225	75.00	0.219	68.10	0.628	30.22
Cl^-	P_{γ_1}	0.09	0.638	20.25	0.132	83.50	0.137	82.88
	P_{γ_2}	0.10	0.225	75.00	0.224	75.11	0.621	31.00
Time:			$7h\ 42m$		$9h\ 11m$		$15h\ 1m$	

Table 3.11 presents the numerical optimization results of three different time periods of $P_{Mg_l^{2+}}$, $P_{Ca_l^{2+}}$, and $P_{Cl_l^-}$. The optimization considers the combined objective function $f_1 + f_2'$, incorporating both concentration minimization and abatement cost terms, with a noise level of $\zeta = 0.2$ to simulate environmental variability. We consider the two injection locations which are located between [$30m$ $130m$] at $50m$ and [$260m$ $360m$] at $80m$. The table reports the optimal injection rates (Opt) for each pollutant at two injection locations, along with the corresponding reduction rates (r-rate %), representing the fractional reduction relative to the maximum permissible injection levels defined by the injection rate (IR) range. The specified IR bounds are [0.09 0.9] for Mg^{2+}, [0.07 0.7] for Ca^{2+}, and [0.08 0.8] for Cl^- at the first injection location P_{γ_1}, where the pollutant concentrations at the observation points $C_{\gamma_l}^{ob}$ are measure for IR rates 0.10, 0.08, and 0.09, respectively. For the second injection location P_{γ_2}, the corresponding IR bounds are [0.2 0.9] for Mg^{2+}, [0.1 0.9] for Ca^{2+}, and [0.1 0.9] for Cl^-, with observed concentrations at the observation points $C_{\gamma_l}^{ob}$ are measure for IR rates 0.25, 0.10, and 0.10, respectively. We consider the four observation points are ($450m$, $50m$), ($450m$, $45m$), ($480m$, $50m$) and ($480m$, $45m$). The contamination injection period is 180 days, followed by another 180 days of no injection to assess post-injection evolution. The DE optimization is performed with a population size of 50, a maximum of 120 generations, a tolerance of 10^{+2} and 10 processors run in parallel, ensuring sufficient exploration and convergence of the solution space. The resulting optimal injection rates and reduction rates at both injection locations quantitatively demonstrate the effectiveness of the algorithm in achieving substantial pollutant reduction under realistic operational constraints. This table illustrates how the optimal injection rates (Opt) and reduction rates (r-rate %) evolve for each contaminant species at two injection locations over the 6th, 8th, and 12th months of simulation under a moderate noise level.

At the first injection location $P_{Mg_1^{2+}}$, the optimal injection decreases from 0.648 at month 6 to 0.156 at month 8 and 0.150 at month 12. This monotonic decline shows that the optimizer

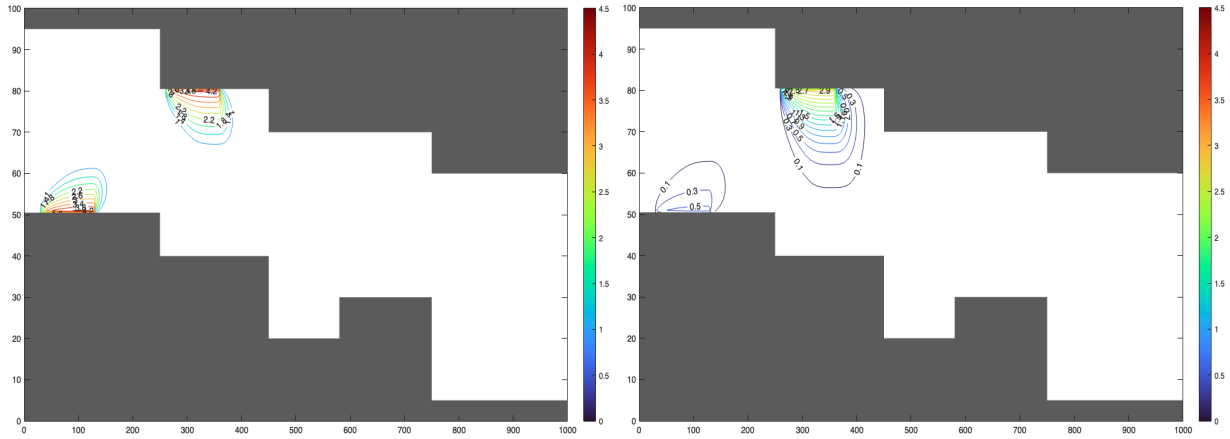

(a) $t = 60$ days

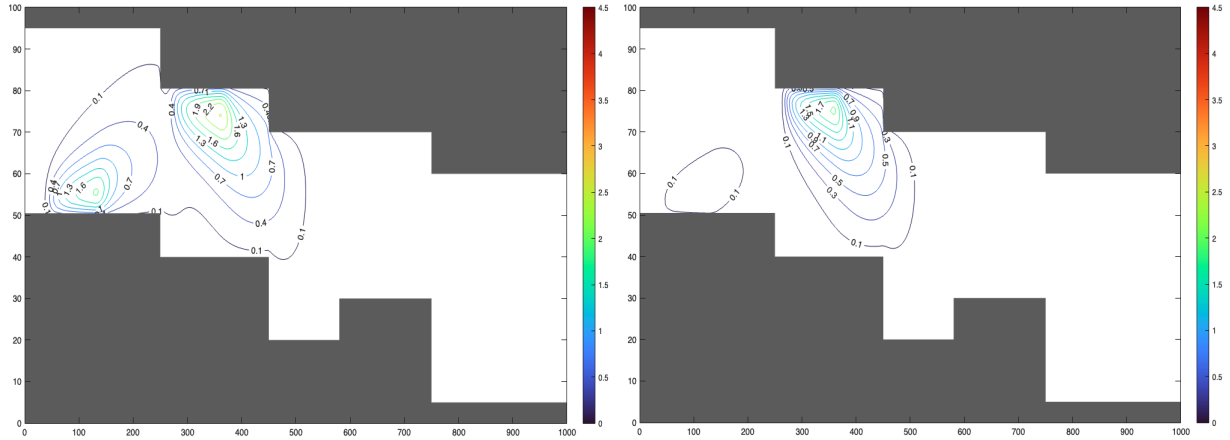

(b) $t = 190$ days

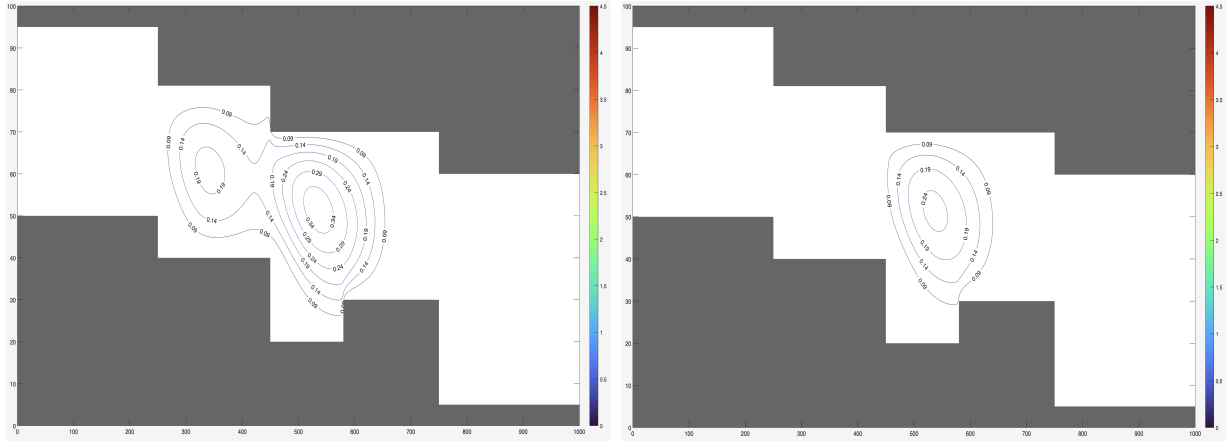

(c) $t = 360$ days

Figure 3.5: Concentration distributions of Cl^- at different time: Left column with maximum injection rates; Right column with optimal injection rates .

progressively lowers $P_{Mg_1^{2+}}$ input as the injection stabilizes and the concentration constraint is satisfied. The very high r-rates after month 8 indicate a transition from active to maintenance control, where less injection is sufficient to sustain pollutant attenuation due to dispersion and reactive retardation. At the second well, the optimal injection starts much lower and remains nearly constant at month 8, before slightly increasing to 0.756 by month 12. This mild rebound in the final phase suggests that P_{γ_2} lies in a region of slower transport or weaker connectivity, where the optimizer increase injection later to compensate for residual concentration buildup.

For $P_{Ca_1^{2+}}$, the optimized rate sharply decreases from 0.573 at month 6 to 0.119 at month 8 and 0.119 at month 12. This pattern is nearly identical to $P_{Mg_1^{2+}}$ but with slightly lower injection magnitudes, reflecting calcium's lower diffusivity and stronger chemical reactivity with carbonate ions. At P_{γ_2}, $P_{Ca_2^{2+}}$ exhibits non-monotonic behaviour. The injection remains steady between months 6 and 8, but then increases drastically at month 12. This significant jump implies that the second injected location becomes more influential during later simulation stages, likely due to reduced reactivity downstream.

Chloride (Cl^- ion behaves differently from the divalent species because of its high mobility and lack of reactivity. At P_{γ_1}, the optimal rate $P_{Cl_1^-}$ falls from 0.638 at month 6 to 0.132 at month 8 and 0.137 at month 12. This outcome highlights chloride's conservative nature; once the target concentration distribution is achieved, the system sustains it largely through advection and dispersion without active control. At P_{γ_2}, the optimized $P_{Cl_2^-}$ rate remains very low at month 6 and month 8, but then surges to 0.621 at month 12. This late-stage injection spike mirrors the behaviour of $P_{Ca_1^{2+}}$ at the same injected location and reveals an underlying hydraulic delay or breakthrough event: as the upstream region clears, residual contaminants likely migrate toward the downstream area, prompting the optimizer to increase $P_{Cl_2^-}$ injection there to rebalance concentration targets.

Across all species and wells, the data exhibit a general decline in optimal injection rates

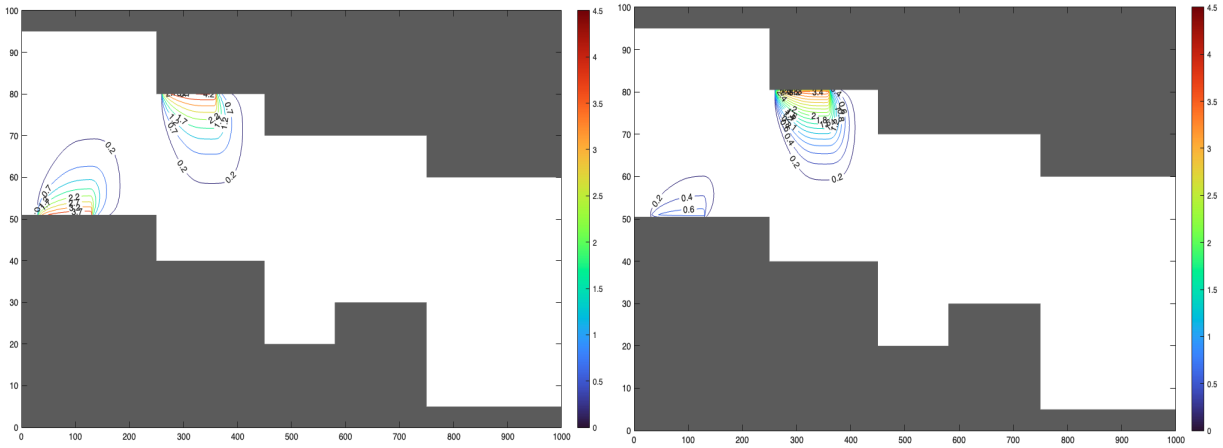

(a) $t = 60$ days

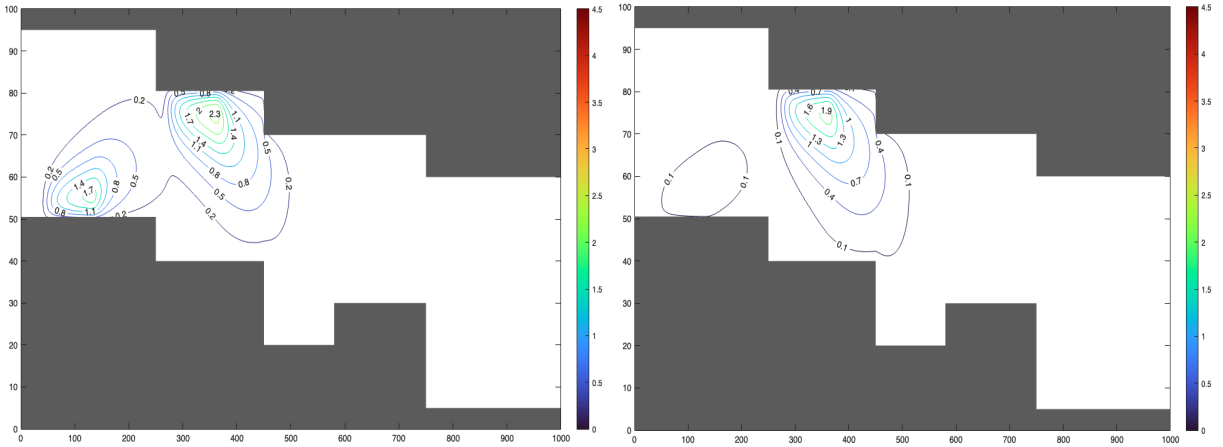

(b) $t = 190$ days

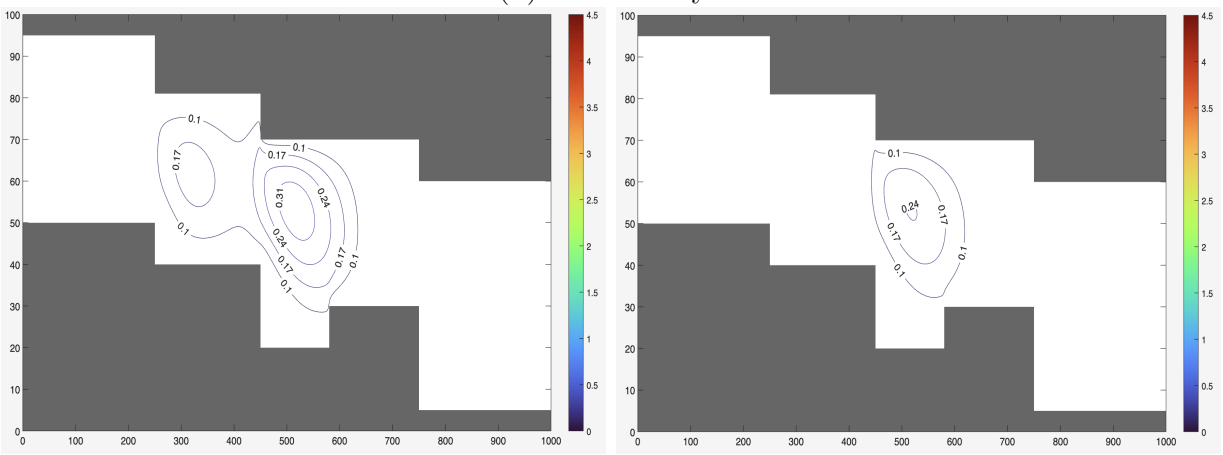

(c) $t = 360$ days

Figure 3.6: Concentration distributions of Mg^{2+} at different time: Left column with maximum injection rates; Right column with optimal injection rates .

with time, except for selective increases at P_{γ_2} during the 12th month. The overall trend of rising r-rates indicates progressively reduced need for control as natural dispersion and chemical interactions take effect. The spatial distinction between the two wells—where P_{γ_1} shows monotonic decline and P_{γ_2} shows mixed or delayed response—clearly demonstrates the spatiotemporal adaptivity of the DE algorithm in handling heterogeneous flow conditions.

The recorded CPU times for 6th month $7h\ 42m$, 8th month $9h\ 11m$, and 12th months $15h\ 1m$, increase with simulation time, consistent with the growing computational complexity of evaluating longer temporal windows and tighter convergence criteria as the optimization proceeds.

Finally, we compare the concentration distributions of the pollutants without optimization injection rates and with optimal injection rates from the optimal control process. We take the maximum injection rates for Cl^-, Mg^{2+} and Ca^{2+} at $P_{\gamma_1} = P_{\gamma_2} = 0.9$. On the other hand, We take the optimal injection rates of $P_{Cl_1^-} = 0.137$, $P_{Cl_2^-} = 0.621$; $P_{Mg_1^{2+}} = 0.150$, $P_{Mg_2^{2+}} = 0.756$; and $P_{Ca_1^{2+}} = 0.119$, $P_{Ca_2^{2+}} = 0.628$. To compute optimal injection rates, we simulated the multicomponent optimal control model. All linked-simulation model descriptions are given in Table 3.11.

Numerical results in Figures 3.5, 3.6 and 3.7 collectively show that the application of optimal injection rates substantially improves contamination control outcomes compared with maximum injection conditions across the three contaminants— Cl^-, Mg^{2+} and Ca^{2+} as well as over the simulated time horizon of 60, 190, and 360 days. For chloride, whose high mobility and non-reactive behaviour allow rapid plume expansion, optimal control effectively suppresses downstream transport and limits unnecessary dispersion after early-stage propagation. Magnesium and Calcium display a more moderate response because it participates in precipitation reactions, and the optimal injections noticeably limit its buildup and spatial expansion by taking advantage of natural attenuation processes. Across all contaminants, the differences between maximum and optimal injection conditions become

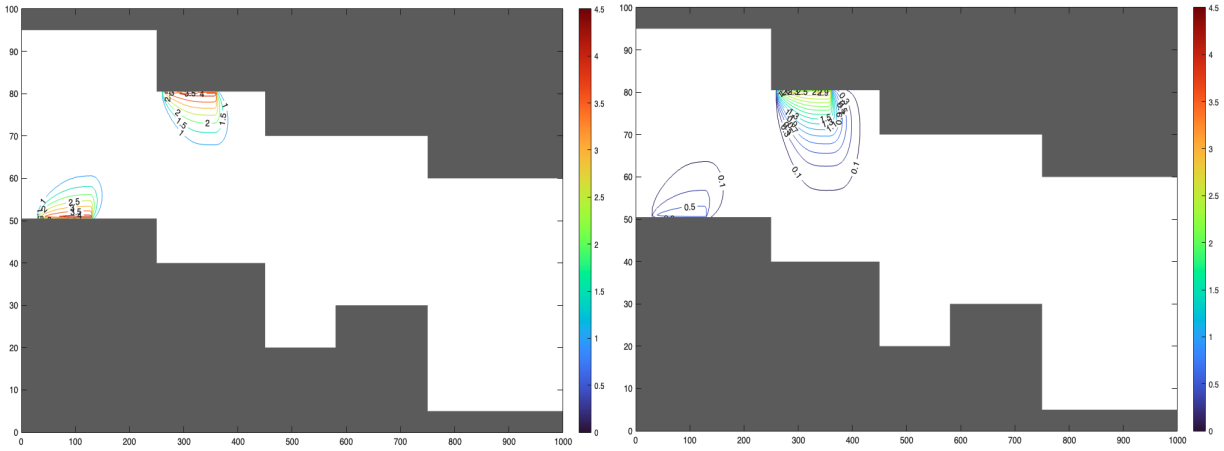

(a) $t = 60$ days

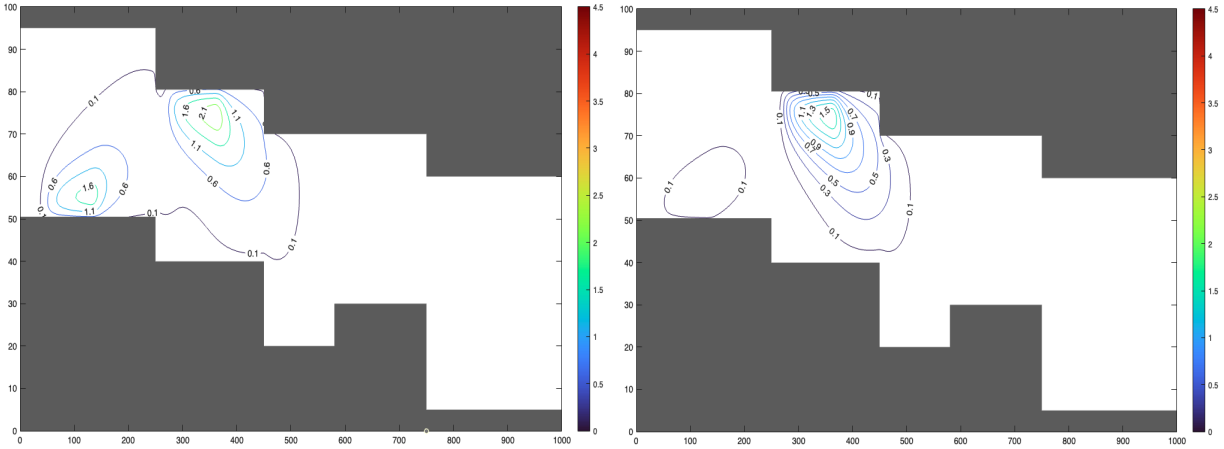

(b) $t = 190$ days

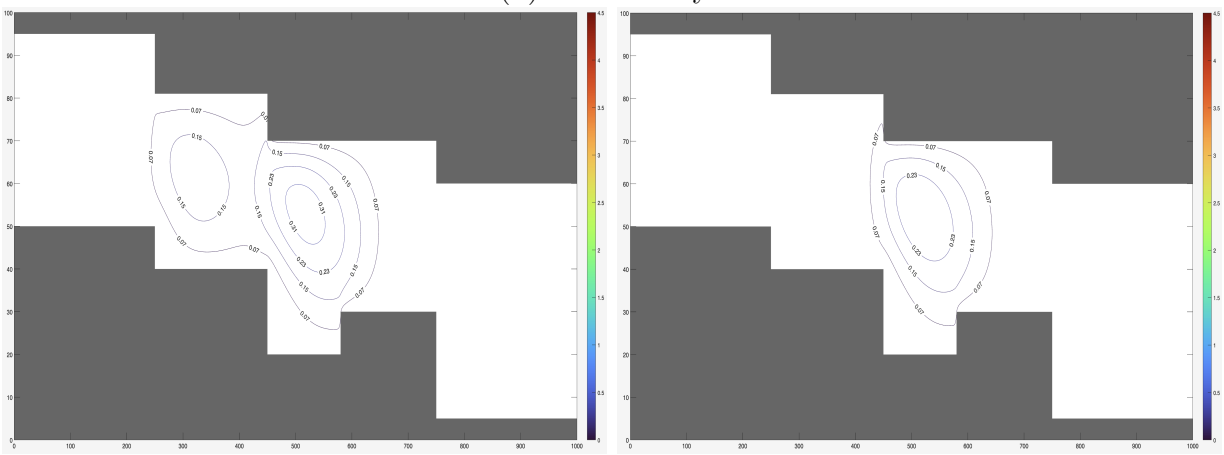

(c) $t = 360$ days

Figure 3.7: Concentration distributions of Ca^{2+} at different time: Left column with maximum injection rates; Right column with optimal injection rates .

even more pronounced at later simulation times, demonstrating that less injection is required as dispersion, chemical reactions, and flow redistribution gradually stabilize the system. Overall, the figures illustrate that optimized injection scheduling reduces contaminant propagation, adapts to the distinct transport and reaction behaviours of each pollutant.

Chapter 4

A Multi-Control Strategy Optimization Framework for Reactive Groundwater Contamination in Porous Media

4.1 Introduction

An effective groundwater management requires optimization strategies that not only control contaminant concentrations but also account for multiple economic and operational constraints, particularly pumping costs [74, 51, 83]. This leads to PDE-constrained optimal control frameworks, where injection and extraction decisions are optimized to achieve environmental targets while maintaining cost efficiency [93, 122, 126].

In this chapter, we develop a multi-control strategy optimal framework for groundwater contamination management. The multi-control objective function integrates concentration least squares error f_1, piecewise abatement cost f_2', and pumping cost f_3, to balance contaminant

reduction with treatment and energy costs while preventing excessive pumping. A boundary injection treatment strategy is considered in terms of reduction rates at injection locations, where the objective function f_2' is proposed in terms of reduction rates to directly reflect remediation effort. A pumping cost function f_3 is incorporated into the optimization to determine optimal pumping rates while accounting for energy and operational costs. This ensures interpretable and bounded control variables. The optimization model is subject to PDE system of multicomponent flow and transport simulation. The developed parallel DE–PDE optimization algorithm is applied to solve the high-dimensional optimization model. We present different numerical experiments. Initially, the influence of reduction rates is investigated in a four-contaminant system under f_1 and f_2', with emphasis on injection locations and well placements. Subsequently, a six-component contamination optimization problem is considered to analyze optimal reduction rates strategies across varying protected zone sizes and depths, along with pumping effects. Finally, the coupled impact of reduction and pumping rates is examined and numerically investigated in an L-shaped aquifer under multi-control of f_1, f_2', and f_3, with performance evaluated through comparisons between worst-case and optimal contamination patterns.

4.2 Mathematical Model of Multicomponent Pollution Control

4.2.1 Multicomponent Mathematical Model

We consider horizontal groundwater flow in a porous aquifer with extraction wells represented by the well term q_w. Contaminant injection is imposed through Neumann boundary conditions along selected segments of the top boundary. The hydraulic head governs the flow field, and the corresponding Darcy velocity defines the advective transport of dissolved species. The transport of each contaminant component is influenced by advection, diffusion, and

well effects associated with pumping, while nonlinear reaction terms account for kinetically controlled chemical interactions among multiple species. These processes are fully coupled and the flow field controls transport and the evolving concentrations are affected by reaction dynamics and well operations. The resulting system forms a time-dependent, multicomponent reactive transport model combining with the well operation affection,

$$S_s \frac{\partial h}{\partial t} = \nabla.(K\nabla h) - q_w, \qquad w = 1,\, 2,\, \ldots,\, n_w \tag{4.1}$$

$$\mathbf{u} = -K\nabla h, \tag{4.2}$$

$$\frac{\partial(\phi c_\alpha)}{\partial t} + \nabla.(\mathbf{u}c_\alpha - D\nabla c_\alpha) = -q_w c_\alpha + \mathbf{R}_\alpha(\mathbf{c}), \quad \alpha = 1, 2, \ldots, n_c,\ w = 1,\, 2,\, \ldots,\, n_w \tag{4.3}$$

where c_α is the concentration $[ML^{-3}]$ for α species, $\alpha = 1, 2, \ldots, n_c$, n_c is the number of species and $\mathbf{c} = (c_1, c_2, \ldots, c_{n_c})$. The diffusion is D, and q_w is the net volumetric flow rate per unit volume of aquifer $[T^{-1}]$ at wells, $w = 1,\, 2,\, \ldots,\, n_w$. n_w is the number of extraction wells. $\mathbf{R}_\alpha(\mathbf{c})$ is the chemical reaction $[ML^{-3}T]$ that describes the mineral precipitation-dissolution reactions and the intra-aqueous reactions.

The initial conditions are

$$h(x, y, 0) = h_0(x, y, 0), \quad (x, y) \in \Omega, \tag{4.4a}$$

$$c_\alpha(x, y, 0) = c_{\alpha_0}(x, y, 0), \quad \alpha = 1, 2, \ldots, n_c, \quad (x, y) \in \Omega. \tag{4.4b}$$

The Dirichlet and Neumann boundary conditions for the water head of the flow are given as

$$h(a_x, y, t) = h_{left}(y, t), \quad h(b_x, y, t) = h_{right}(y, t), \tag{4.5a}$$

$$\frac{\partial h}{\partial y}(x, t) = 0, \quad (x, y) \in \text{the top and bottom boundaries of } \Omega. \tag{4.5b}$$

Let the first group of concentrations, c_β, $\beta = 1, 2, ..., n_e$, represents the concentrations of the existing components, and let the second group of concentrations, c_γ, $\gamma = n_e + 1, n_e + 2, ..., n_c$,

represents the concentrations of the injected components. The boundary conditions of concentrations are given as

$$\frac{\partial c_\beta}{\partial x}(y,t)=0, \quad \frac{\partial c_\beta}{\partial y}(x,t)=0, \quad (x,y)\in\partial\Omega, \quad \beta=1,2,...,n_e, \tag{4.6a}$$

$$\frac{\partial c_\gamma}{\partial y}(x,t)=-J_l c^*_{\gamma,l}(1-\mathbf{r}_{\gamma,l}),\ on\ \Gamma_l\in\partial\Omega, \quad \frac{\partial c_\gamma}{\partial x}=0, \frac{\partial c_\gamma}{\partial y}=0, \quad \text{on} \quad \partial\Omega\backslash\cup\Gamma_l, \tag{4.6b}$$

where, $\gamma=n_e+1,n_e+2,...,n_c$. The Γ_l, where $l=1,2,...,n_s$, represent the segments located on the upper boundary of the domain where the pollutions are injected into the aquifer. $J_l[m/day]$ is the flux normal to the boundary at location l and $c^*_{\gamma,l}$ is the boundary influent concentration of the species γ at the location l. $\partial\Omega\backslash\cup\Gamma_l$ represents the rest boundary except $\cup\Gamma_l$.

4.2.2 Multi-control Strategy Optimal Control Model

The multicomponent optimal control model is formulated as a PDE-constrained optimization problem in which the objective is to determine the optimal reduction rates $r_{\gamma,l}$ at the injection locations and the pumping rates Q_w at the extraction wells. The control variables are selected such that the discrepancy between simulated and target contaminant concentrations is minimized, while simultaneously accounting for treatment and pumping costs. The optimization is subject to the governing groundwater flow and multicomponent reactive transport equations, ensuring that the control strategy remains consistent with the underlying physical processes. In addition, constraints are imposed on the admissible concentration levels at observation points, as well as on the feasible ranges of the reduction rates and pumping rates, reflecting environmental regulations and operational limitations. Under these conditions, the multicomponent multi-control strategy optimization problem can be described as follows:

$$\min_{\{\{\mathbf{r}_{\gamma,\mathbf{l}}\},\mathbf{Q_w}\}} \mathbf{f}(\mathbf{r}_{\gamma,\mathbf{l}},\mathbf{Q_w}); \tag{4.7}$$

subject to

$$\text{The governing system of PDEs:} \quad (4.1) - (4.6b), \tag{4.8}$$

$$c_{\gamma_s}^{min} \leq c_{\gamma_s} \leq c_{\gamma_s}^{max}, \quad s = 1,\, 2,\, \ldots,\, n_{ob},\ \gamma = n_e + 1,\, n_e + 2,\, \ldots,\, n_c, \tag{4.9}$$

$$r_{\gamma,l}^{min} \leq r_{\gamma,l} \leq r_{\gamma,l}^{max}, \quad l = 1,\, 2,\, \ldots,\, n_s,\ \gamma = n_e + 1,\, n_e + 2,\, \ldots,\, n_c, \tag{4.10}$$

$$Q_w^{min} \leq Q_w \leq Q_w^{max}, \quad w = 1,\, 2, \ldots,\, n_w \tag{4.11}$$

$$\sum_{w=1}^{n_w} Q_w \leq Q_{tot} \tag{4.12}$$

where $\mathbf{r}_{\gamma,l} = \{r_{\gamma,l};\ l = 1, 2, ..., n_s,\ \gamma = n_e + 1, n_e + 2, ..., n_c\}$.

The constraints in Equations (4.8)-(4.13) define the admissible bounds for concentrations, reduction rates, and pumping rates in the optimization problem. Equation (4.8) be the system of groundwater mathematical model. Equation (4.9) imposes limits on the simulated concentration $c_{\gamma s}$ of species γ at each observation location s, where $c_{\gamma s}^{\min}$ and $c_{\gamma s}^{\max}$ represent the minimum and maximum allowable concentration levels, ensuring compliance with environmental standards. Equation (4.10) specifies bounds on the reduction rate $r_{\gamma,l}$ of species γ at injection location l, where $r_{\gamma,l}^{\min}$ and $r_{\gamma,l}^{\max}$ denote the minimum and maximum achievable treatment efficiencies, reflecting practical and technological limitations. Equation (4.11) constrains the pumping rate Q_w at each extraction well w within the interval $[Q_w^{\min}, Q_w^{\max}]$, ensuring that the pumping operation remains within feasible operational capacity. The total pumping rate from all extraction wells is constrained by the treatment plant capacity, as expressed in Equation (4.12), where Q_{tot} represents the maximum allowable processing capacity. Together, these constraints guarantee that the optimal control solution is physically realistic, operationally feasible, and environmentally acceptable.

The multi-control strategy objective function is proposed as

$$\mathbf{f}(\mathbf{r}_{\gamma,\mathbf{l}},\ \mathbf{Q_w}) = \mathbf{f_1}(\mathbf{r}_{\gamma,\mathbf{l}}) + \mathbf{f_2}(\mathbf{r}_{\gamma,\mathbf{l}}) + \mathbf{f_3}(\mathbf{Q_w}) \tag{4.13}$$

where, the objective function $f_1(\mathbf{r}_{\gamma,l})$ contains the overall fitness between the simulated concentration c_{γ_s} and the observed concentration $c_{\gamma_s}^{obs}$, the abatement cost and maintenance cost as follows

$$f_1(\mathbf{r}_{\gamma,l}) = \sum_{s=1}^{n_{ob}} \sum_{\gamma=n_e+1}^{n_c} \int_0^T \omega_{\gamma_s} \left[c_{\gamma_s}(\mathbf{r}_{\gamma,l}, t) - c_{\gamma_s}^{ob}(t) \right]^2 dt \tag{4.14}$$

The allowable environmental concentrations $c_{\gamma_s}^{ob}(t)$ are perturbed from the ideal concentration at minimum injection rates. The weight functions ω_{γ_s} are designed to normalize the component affection in the objective function which has defined in chapter two equation (2.16).

The objective function $f_2(r_{\gamma,l})$ represents the abatement or treatment cost associated with reducing contaminant concentrations at the injection locations [90, 124]. It quantifies the cost required to achieve a specified reduction rate $r_{\gamma,l}$ for each species γ at location l over the simulation period. The formulation incorporates both fixed and variable cost components, where the fixed term represents infrastructure-related expenses and the variable term reflects the operational cost that increases with treatment intensity. The cost function is nonlinear and may include a piecewise structure, allowing different cost regimes before and after a threshold reduction level. This captures the practical reality that moderate treatment is relatively economical, whereas achieving high reduction levels requires significantly higher cost due to advanced technologies or stricter regulatory requirements. Therefore, $f_2(\mathbf{r}_{\gamma,l})$ plays a crucial role in balancing contaminant reduction with economic efficiency in the optimization framework. The cost function $f_2(\mathbf{r}_{\gamma,l})$ defines as follow:

$$f_2(\mathbf{r}_{\gamma,l}) = \sum_{l=1}^{n_s} \sum_{\gamma=n_e+1}^{n_c} \int_0^T \omega_2 z_l A_{\gamma,l}(\mathbf{r}_{\gamma,l}) dt \tag{4.15}$$

where,

$$A_{\gamma,l}(r_{\gamma,l}) = \left(b_{1,l}(c_{\gamma,l}^*)^{b_{2,l}} + b_{3,l}(c_{\gamma,l}^*)^{b_{2,l}} \mathbf{r}_{eff,l}^{b_{4,l}} \right).$$

Let z_l be the binary decision parameter given by

$$z_l = \begin{cases} 1, & for \quad \text{the treatment unit exist on location } l, \\ 0, & for \quad \text{the treatment unit does not exist (no treatment) on location } l. \end{cases}$$

The reduction rate (treatment efficiency), $\mathbf{r}_{eff,l} = \dfrac{\sum_{\gamma=n_e+1}^{n_c} C^*_{\gamma,l}\mathbf{r}_{\gamma,l}}{\sum_{\gamma=n_e+1}^{n_c} C^*_{\gamma,l}}$

The modified objective function $f_2'(r_{\gamma,l})$ represents a piecewise abatement cost formulation that incorporates a threshold reduction rate r_c to distinguish between standard and advanced treatment regimes. For reduction levels below the threshold ($r_{\text{eff},l} < r_c$), the cost increases smoothly according to a baseline nonlinear function, reflecting conventional treatment operations. However, when the effective reduction rate exceeds the threshold ($r_{\text{eff},l} \geq r_c$), an additional penalty term is introduced, leading to a steeper increase in cost. This penalty captures the significantly higher expenses associated with achieving high removal efficiencies, such as the use of advanced technologies or compliance with stricter environmental standards. The resulting piecewise structure ensures continuity of the cost function while introducing nonlinearity that reflects realistic economic behaviour, thereby encouraging the optimization to avoid unnecessarily high reduction levels unless they are essential for meeting concentration constraints. The modified objective function $f_2'(r_{\gamma,l})$ defines as follow:

$$f_2'(\mathbf{r}_{\gamma_l}) = \sum_{l=1}^{n_s} \sum_{\gamma=n_e+1}^{n_c} \int_0^T \omega_3 A'_{\gamma_l}(\mathbf{r}_{\gamma_1}) dt \tag{4.16}$$

where,

$$A'_{\gamma_l}(r_{\gamma_l}) = \begin{cases} \left(b_{1,l}(C^*_{\gamma,l})^{b_{2,l}} + b_{3,l}(C^*_{\gamma,l})^{b_{2,l}} r_{eff,l}^{b_{4,l}}\right), & for \quad r < r_c, \\ \left(b_{1,l}(C^*_{\gamma,l})^{b_{2,l}} + b_{3,l}(C^*_{\gamma,l})^{b_{2,l}} r_{eff,l}^{b_{4,l}} + b_{5,l}(C^*_{\gamma,l})^{b_{2,l}} \left((r_{eff,l} - r_c)^{b_{6,l}}\right)\right), & r \geq r_c. \end{cases}$$

In the piecewise abatement cost function, each parameter plays a critical role in capturing the economic and technical complexity of groundwater pollution remediation. The threshold reduction rate r_c defines the point at which the cost structure changes, representing regulatory limits or technological boundaries, where basic treatment transitions to advanced methods. The parameter b_1 represents fixed setup costs such as infrastructure and installation, independent of reduction effort, and usually derived from engineering estimates. The exponent b_2, models economies of scale, determining how cost scales with treated volume W; values less than 1 (typically 0.6–0.9) reflect decreasing per-unit costs for larger systems. Before reaching the threshold, the variable abatement cost is controlled by b_3, which is the base multiplier for operational cost per unit reduction, and b_4 which is an exponent that determines how steeply the cost rises as reduction efforts increase (e.g., linear for $b_4 = 1$, quadratic for $b_4 = 2$). Beyond the threshold, an additional penalty term is applied using b_5, which scales the post-threshold cost component and is typically set significantly higher than b_3 to reflect the cost of deploying more advanced treatment technologies or complying with stricter regulations. The steepness of this penalty is governed by b_6, an exponent often ranging from 2 to 5, which models how aggressively cost escalates beyond the threshold. Together, these parameters allow the model to reflect both the gradual rise in costs during initial treatment and the sharp cost escalation encountered in achieving high reduction rates. Choosing parameter values should be based on real-world data from engineering designs, regulatory benchmarks, and empirical studies. This piecewise approach makes the cost function continuous but nonlinear, enabling realistic representation of technical limits, compliance constraints, and cost optimization trade-offs over time.

Finally, the objective function $f_3(Q_w)$ represents the total energy-based cost associated with groundwater extraction through pumping wells, and it plays a crucial role in ensuring that the optimization framework remains physically and economically realistic [6]. In groundwater remediation problems, pumping is one of the primary mechanisms for controlling contaminant

transport, as it induces hydraulic gradients that can capture and remove dissolved pollutants. However, excessive pumping is not feasible in practice due to significant energy consumption and operational costs. Therefore, f_3 is introduced to penalize unnecessary or inefficient pumping within the optimization process.

Mathematically, the pumping cost function $f_3(Q_w)$ is formulated as a time-integrated energy expenditure over all extraction wells:

$$f_3(Q_w) = \sum_{w=1}^{n_w} \int_0^T \omega_3 \, a_1 \, z_w \, \frac{Q_w(t) \, \rho_w g H_w}{\eta} \, dt, \tag{4.17}$$

where $Q_w(t) \, [m^2/day]$ denotes the pumping rate at well w, ρ_w is the fluid density, g is gravitational acceleration, η is the pump efficiency. The parameters a_1, z_w, and ω_3 are scaling and weighting coefficients that convert physical energy consumption into economic cost and allow flexibility in emphasizing pumping penalties within the overall objective function.

The quantity H_w denotes the hydraulic lift (or head difference) associated with extraction well w. It is defined as,

$$H_w = h_{\text{surface}} - h(t, x_w, y_w),$$

where h_{surface} represents the ground surface elevation and $h(x_w, y_w)$ is the hydraulic head at the location of well w. Physically, H_w corresponds to the vertical distance that groundwater must be lifted during pumping. This term directly influences the energy required for extraction, as larger lift heights result in higher energy consumption and, consequently, increased pumping cost.

From a physical perspective, the term $\rho_w g H_w$ represents the energy required per unit volume of water lifted, while $Q_w(t)$ defines the volumetric flow rate. Their product gives the instantaneous power required for pumping, and integration over time yields the total energy consumption. Dividing by efficiency $\eta \in [0 \quad 1]$ accounts for real-world energy losses in pumping systems. Thus, f_3 is fundamentally an energy-based cost model grounded in fluid

mechanics and hydraulic engineering principles.

The pumping rates Q_w directly influence the velocity field through Darcy's law, thereby affecting advective transport and plume migration. As a result, the optimization must balance two competing effects: increasing Q_w enhances contaminant capture and reduces concentrations at observation locations, but it also increases the cost captured by f_3. This creates a trade-off between environmental effectiveness and economic efficiency, which is central to realistic groundwater remediation design.

4.3 Discrete Multicomponent Pollution Optimal Control Model

We construct a discrete optimal control model for multicomponent contamination flows by discretizing the governing PDE system in both space and time. The resulting formulation transforms the continuous PDE-constrained optimization problem into a high-dimensional problem, where the interactions between flow, transport, and reaction processes are preserved. This discrete framework provides the foundation for efficient numerical simulation and enables the application of the optimization algorithm to determine optimal control strategies.

4.3.1 Numerical Scheme For Multicomponent Contamination Equations

The domain $\Omega = (a_x, b_x) \times (a_y, b_y)$ is discretized on a structured mesh $\Omega_h = I_h \times J_h$, where

$$I_h = \{x_i = a_x + i\Delta x,\ i = 0, 1, \ldots, n_x\}, \quad J_h = \{y_j = a_y + j\Delta y,\ j = 0, 1, \ldots, n_y\}.$$

The time interval $[0, T]$ is partitioned as $t^n = n\Delta t$, $n = 0, 1, \ldots, N_t$.

The numerical scheme for the multicomponent contamination system with well operation is

For $n = 0, 1, \ldots, N_t$, do

Step 1. To solve the water-head along the x-direction, for $j = 1, 2, \ldots, n_y$,

$$S_s \frac{H_{i,j}^{n+\frac{1}{2}} - H_{i,j}^{n}}{\Delta t} - \frac{1}{\Delta x}\left[K_{x_{i+\frac{1}{2},j}} \frac{H_{i+1,j}^{n+\frac{1}{2}} - H_{i,j}^{n+\frac{1}{2}}}{\Delta x} - K_{x_{i-\frac{1}{2},j}} \frac{H_{i,j}^{n+\frac{1}{2}} - H_{i-1,j}^{n+\frac{1}{2}}}{\Delta x}\right] + q_{w_{i,\ j}}^{n+1} = 0,$$
$$i = 1, 2, \ldots, n_x - 1, \tag{4.18}$$

To solve the water-head along the y-direction, for $i = 1, 2, \ldots, n_x - 1$,

$$S_s \frac{H_{i,j}^{n+1} - H_{i,j}^{n+\frac{1}{2}}}{\Delta t} - \frac{1}{\Delta y}\left[K_{y_{i,j+\frac{1}{2}}} \frac{H_{i,j+1}^{n+1} - H_{i,j}^{n+1}}{\Delta y} - K_{y_{i,j-\frac{1}{2}}} \frac{H_{i,j}^{n+1} - H_{i,j-1}^{n+1}}{\Delta y}\right] = 0,$$
$$j = 1, 2, \ldots, n_y, \tag{4.19}$$

Step 2. To compute the Darcy's velocity along the x-direction by, for $j = 1, 2, \ldots, n_y$

$$U_{x_{i+1,j}}^{n+1} = -K_{x_{i+1,j}} \frac{H_{i+2,j}^{n+1} - H_{i,j}^{n+1}}{2\Delta x}, \quad i = 0, 1, \ldots, n_x - 2, \tag{4.20}$$

and at the end points

$$U_{x_{0,j}}^{n+1} = -K_{x_{0,j}} \frac{H_{1,j}^{n+1} - H_{0,j}^{n+1}}{\Delta x}, \qquad U_{x_{n_x,j}}^{n+1} = -K_{x_{n_x,j}} \frac{H_{n_x,j}^{n+1} - H_{n_x-1,j}^{n+1}}{\Delta x}. \tag{4.21}$$

To compute the Darcy's velocity along the y-direction by, for $i = 0, 1, \ldots, n_x - 1$

$$U_{y_{i+\frac{1}{2},j+\frac{1}{2}}}^{n+1} = -K_{y_{i+\frac{1}{2},j+\frac{1}{2}}} \frac{H_{i+\frac{1}{2},j+1}^{n+1} - H_{i+\frac{1}{2},j}^{n+1}}{\Delta y}, \quad j = 1, 2, \ldots, n_y - 1, \tag{4.22}$$

and at the end points

$$U_{y_{i+\frac{1}{2},\frac{1}{2}}}^{n+1} = -K_{y_{i+\frac{1}{2},\frac{1}{2}}} \frac{H_{i+\frac{1}{2},1}^{n+1} - H_{i+\frac{1}{2},0}^{n+1}}{\Delta y}, \tag{4.23}$$

$$U_{y_{i+\frac{1}{2},n_y+\frac{1}{2}}}^{n+1} = -K_{y_{i+\frac{1}{2},n_y+\frac{1}{2}}} \frac{H_{i+\frac{1}{2},n_y+1}^{n+1} - H_{i+\frac{1}{2},n_y}^{n+1}}{\Delta y}. \tag{4.24}$$

Step 3. To solve the multicomponent concentrations along the x-direction by, for $j = 1, 2, \ldots, n_y$, and $\alpha = 1, 2, \ldots, n_c$

$$\phi\frac{C^{n+\frac{1}{2}}_{\alpha_{i+\frac{1}{2},j}} - C^{n}_{\alpha_{i+\frac{1}{2},j}}}{\Delta t} + \frac{Z^{x,n+\frac{1}{2}}_{\alpha_{i+1,j}} - Z^{x,n+\frac{1}{2}}_{\alpha_{i,j}}}{\Delta x} + q^{n+1}_{w_{i,\ j}} C^{n}_{\alpha_{w_{i+\frac{1}{2},j}}} = 0, \quad i = 0, 1, \ldots, n_x - 1, \tag{4.25}$$

$$\begin{aligned} Z^{x,n+\frac{1}{2}}_{\alpha_{i+1,j}} &= U^{n+1}_{x_{i+1,j}} \left[s\left(U^{n+1}_{x_{i+1,j}}\right) C^{n+\frac{1}{2}}_{\alpha_{i+\frac{1}{2},j}} + \left(1 - s\left(U^{n+1}_{x_{i+1,j}}\right)\right) C^{n+\frac{1}{2}}_{\alpha_{i+\frac{3}{2},j}} \right] \\ &\quad - D^{*}_{x_{i+\frac{1}{2},j}} \frac{C^{n+\frac{1}{2}}_{\alpha_{i+\frac{3}{2},j}} - C^{n+\frac{1}{2}}_{\alpha_{i+\frac{1}{2},j}}}{\Delta x}, \end{aligned} \tag{4.26}$$

To solve the multicomponet concentrations along the y-direction by, for $i = 0, 1, \ldots, n_x - 1$ and $\alpha = 1, 2, \ldots, n_c$

$$\phi\frac{C^{n+1}_{\alpha_{i+\frac{1}{2},j}} - C^{n+\frac{1}{2}}_{\alpha_{i+\frac{1}{2},j}}}{\Delta t} + \frac{Z^{y,n+1}_{\alpha_{i+\frac{1}{2},j+\frac{1}{2}}} - Z^{y,n+1}_{\alpha_{i+\frac{1}{2},j-\frac{1}{2}}}}{\Delta y} = R_{\alpha}\left(\mathbf{C}^{n+\frac{1}{2}}_{i+\frac{1}{2},j}\right), j = 1, 2, \ldots, n_y, \tag{4.27}$$

$$\begin{aligned} Z^{y,n+1}_{\alpha_{i+\frac{1}{2},j+\frac{1}{2}}} &= U^{n+1}_{y_{i+\frac{1}{2},j+\frac{1}{2}}} \left[s\left(U^{n+1}_{y_{i+\frac{1}{2},j+\frac{1}{2}}}\right) C^{n+1}_{\alpha_{i+\frac{1}{2},j}} + \left(1 - s\left(U^{n+1}_{y_{i+\frac{1}{2},j+\frac{1}{2}}}\right)\right) C^{n+1}_{\alpha_{i+\frac{1}{2},j+1}} \right] \\ &\quad - D^{*}_{y_{i+\frac{1}{2},j+\frac{1}{2}}} \frac{C^{n+1}_{\alpha_{i+\frac{1}{2},j+1}} - C^{n+1}_{\alpha_{i+\frac{1}{2},j}}}{\Delta y}, \end{aligned} \tag{4.28}$$

where

$$D^{*}_{x_{i+\frac{1}{2},j}} = \frac{D_{x_{i+\frac{1}{2},j}}}{1 + \frac{|U^{n+1}_{x_{i+1,j}}|\Delta x}{2D_{x_{i+\frac{1}{2},j}}}}, D^{*}_{y_{i+\frac{1}{2},j+\frac{1}{2}}} = \frac{D_{y_{i+\frac{1}{2},j+\frac{1}{2}}}}{1 + \frac{|U^{n+1}_{y_{i+\frac{1}{2},j+\frac{1}{2}}}|\Delta y}{2D_{y_{i+\frac{1}{2},j+\frac{1}{2}}}}}.$$

The boundary conditions are also provided, and the initial values are defined as

$$H^{0}_{i,j} = h_0(i,j), \quad i = 1, 2, \ldots, n_x - 1, \quad j = 1, 2, \ldots, n_y, \tag{4.29a}$$

$$C^{0}_{\alpha_{i,j}} = c_{\alpha_0}(i,j), \quad i = 1, 2, ...n_x, \quad j = 1, 2, \ldots, n_y, \alpha = 1, 2, \ldots, n_c. \tag{4.29b}$$

4.3.2 Discrete Multicomponent Pollution Optimal Control Model

To construct a discrete approximation of the objective function, the continuous integrals appearing in the objective functional are replaced by finite sums over the temporal grid, while the state variables are evaluated using the numerical solutions obtained from the discretized flow and contamination equations. This transformation converts the objective function into a discrete form, expressed in terms of concentrations, reduction rates, and pumping rates. The discrete multicontrol strategy objective function can be obtained as

$$\begin{aligned} F\left(\mathbf{r}_{\gamma_l} Q_w\right) &= \sum_{s=1}^{n_{ob}} \sum_{\gamma=n_e+1}^{n_c} \sum_{n=1}^{N_t} \omega_{\gamma_s} \left[C_{\gamma_s}\left(\mathbf{r}_{\gamma_l}, t^n\right) - C_{\gamma_s}^{ob}(t^n)\right]^2 \Delta t \\ &\quad + \sum_{l=1}^{n_s} \sum_{\gamma=n_e+1}^{n_c} \sum_{n=1}^{N_t} \omega_2 A_{\gamma_l}\left(r_{\gamma_l}(t^n)\right) \Delta t + \sum_{w=1}^{n_w} \sum_{n=1}^{N_t} a_1 z_w \frac{Q_w(t^n)\rho_w g H_w}{\eta} \Delta t \end{aligned} \tag{4.30}$$

Thus, the discrete multicomponent pollution multicontrol strategy model is defined as finding the optimal r_{γ_l} and Q_w, $\gamma = n_e + 1,\, n_e + 2,\, \ldots,\, n_c$, $l = 1,\, 2,\, \ldots,\, n_s$, $w = 1,\, 2,\, \ldots,\, n_w$ such that

$$\min_{\{\mathbf{r}_{\gamma_l}, Q_w\}} F\left(\mathbf{r}_{\gamma_l}, Q_w\right) \tag{4.31}$$

subject to

Satisfying the splitting improved upwind finite difference scheme of $(4.18) - (4.29)$, (4.32)

$$c_{\gamma_s}^{min} \le c_{\gamma_s}(t^n) \le c_{\gamma_s}^{max}, \quad s = 1,\, 2,\, \ldots,\, n_{ob},\ \gamma = n_e + 1,\, n_e + 2,\, \ldots,\, n_c, \tag{4.33}$$

$$r_{\gamma,l}^{min} \le r_{\gamma,l} \le r_{\gamma,l}^{max}, \quad l = 1,\, 2,\, \ldots,\, n_s,\ \gamma = n_e + 1,\, n_e + 2,\, \ldots,\, n_c, \tag{4.34}$$

$$Q_w^{min} \le Q_w(t^n) \le Q_w^{max}, \quad w = 1,\, 2, \ldots,\, n_w \tag{4.35}$$

$$\sum_{w=1}^{n_w} Q_w(t^n) \le Q_{tot} \tag{4.36}$$

where $\{C_{\gamma_s}(t^n)\}$ are the numerical concentrations solved at the observation locations. The

lower and upper bounds of concentrations at observation locations are denoted by $c_{\gamma_s}^{min}$ and $c_{\gamma_s}^{max}$. $Q_w(t^n)$ be the pumping rate at well w. $\{C_{\gamma_s}^{ob}(t^n)\}$ are the allowable concentrations at the observation sites that are simulated at the largest deduction rates $r_{\gamma_l} = r_{\gamma_l}^{max}$ or other expected injection rates.

4.3.3 Parallel DE-PDE Multicomponent Optinization Implementation

We solve the multi-control multicomponent optimization model by the developed MPI-based parallel DE-PDE system in the previous chapter, which distributes population evaluations across multiple processors. The master process manages the population and convergence, while worker processes independently perform mutation, crossover, and parallel DE-PDE fitness evaluation. Since each candidate solution is independent, the method exhibits natural coarse-grained parallelism, making it highly efficient and scalable. This parallelization significantly reduces wall-clock time without altering the underlying DE search dynamics. The developed parallel DE-PDE optimization algorithm is particularly well-suited for multicontrol large-scale, nonlinear groundwater models, where efficient and reliable optimization is critical for practical decision-making.

4.4 Numerical Experiments

In this section, we present numerical experiments to solve the multi-control optimization problems to the multicomponent PDE. The experiments are designed to investigate the effectiveness of the composite objective function, which integrates the concentration-matching term f_1, the abatement cost function f_2', and the pumping cost term f_3. These components collectively represent the trade-off between environmental objectives and operational costs, allowing for a comprehensive assessment of remediation strategies. By varying control

parameters such as reduction rates, pumping rates, and spatial configurations of injection and extraction wells, the numerical experiments illustrate how the multi-control objective function combines influence the optimal solutions. In addition, the parallel DE-PDE algorithm is employed to efficiently solve the resulting high-dimensional optimization problem.

Example 1: This experiment examines a multicomponent groundwater contamination problem in a two-dimensional aquifer, incorporating advection, diffusion, and kinetically controlled precipitation reactions. The optimization is performed using the objective function as the concentration-matching objective f_1 and the composite objective $f_1 + f_2$, combining environmental performance with abatement cost. This formulation enables a comparative analysis of how different objective functions influence the optimal reduction rates and the resulting contaminant distribution within the aquifer.

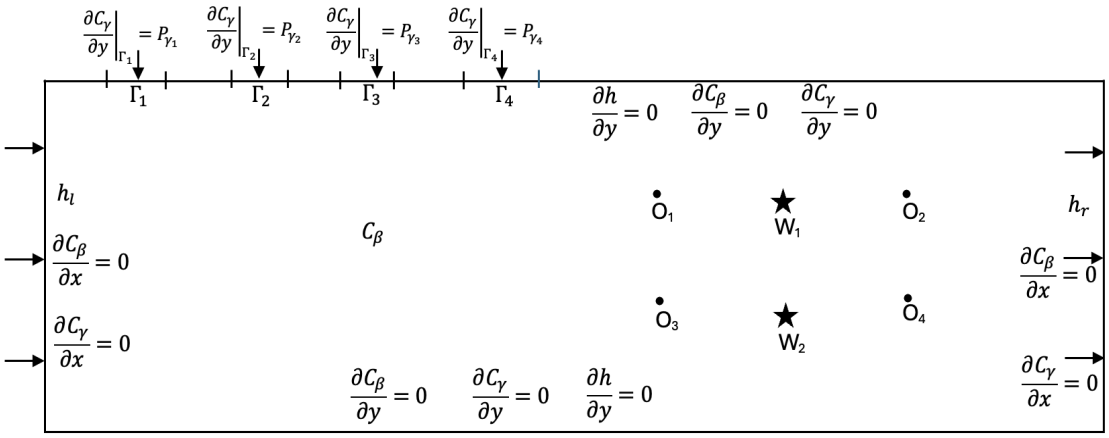

Figure 4.1: Hypothetical rectangular vertical aquifer.

We consider four pollution components $C_{CO_3^{2-}}$, and $C_{Mg^{2+}}$, $C_{Ca^{2+}}$, C_{Cl^-}, where the aquifer contains $C_{CO_3^{2-}}$ inside and the other three components are injected on the specific top of the aquifer. We consider the domain $\Omega = [0,\, 1000m] \times [0,\, 20m]$ and the total simulation time period of 1 years. The left boundary value of water head is $h_{left} = 200m$ and the right boundary value of water head is $h_{right} = 20m$. The initial condition for water head is $h_0 = 20m$ as well as the initial value for pollution concentrations $C_{Ca^{2+}}$, $C_{Mg^{2+}}$, and C_{Cl^-} are

zero and $C_{CO_3^{2-}} = 0.67 mol/m^2$. We consider four reduction rates r_{γ_l}, $l = 1, 2, 3, 4$, in the four injected pieces, and the four observation locations of $O_{n_{ob}}$, $n_{ob} = 1, 2, 3, 4$, are placed deep in the aquifer to track the spread of the contaminant, as shown in Figure 4.1. In the figure 4.1, $P_{\gamma\ l} = J_l c^*_{\gamma,l}(1 - \mathbf{r}_{\gamma,l})$, $l = 1,\ 2,\ 3,\ 4$.

The general kinetic chemical reaction term $\mathbf{R}_\alpha(\mathbf{c})$ is defined as [9, 105]

$$\mathbf{R}_\alpha(\mathbf{c}) = v_\alpha\, \sigma(c, T, pH, a_s),$$

where v_α denotes the stoichiometric coefficient of species α. A positive value of v_α indicates production, a negative value represents consumption, and $v_\alpha = 0$ implies that the species is not involved in the reaction. The function $\sigma(c, T, pH, a_s)$ represents the kinetic reaction rate, which depends on the concentration vector $\mathbf{c} = (c_1, c_2, \ldots, c_{n_s})$, temperature T, and reactive surface area a_s.

For mineral reactions, the kinetic rate is modelled using a nonlinear expression of the form

$$\sigma = k a_s \left(1 - \frac{K_w}{K_{eq}}\right)^n,$$

where k is the intrinsic rate constant, K_w is the ion activity product, K_{eq} is the equilibrium constant, and n is the reaction order. This formulation captures the deviation from thermodynamic equilibrium, allowing the model to represent both precipitation and dissolution processes depending on the saturation state of the system.

For intra-aqueous reactions, the kinetic rate is expressed as

$$\sigma = K_T \sum_{\alpha=1}^{n_s} c_\alpha^n,$$

where K_T is a temperature-dependent rate constant and c_α denotes the concentration of the aqueous species. This form accounts for homogeneous reactions occurring entirely within the

fluid phase without involving solid surfaces.

In this study, we simulate multicomponent reactive transport involving mineral precipitation processes. As a representative example, we consider the formation of magnesite through the reaction

$$Mg^{2+} + Ca^{2+} + 2CO_3^{2-} \rightarrow CaMg(CO_3)_2(s).$$

The rate of mineral formation is modeled as

$$G_r = k a_s \, C_{Mg^{2+}} \, C_{Ca^{2+}} \, C^2_{CO_3^{2-}},$$

where k is the reaction rate constant, a_s is the effective reactive surface area, and $C_{Mg^{2+}}$, $C_{Ca^{2+}}$, and $C_{CO_3^{2-}}$ are the concentrations of the corresponding species. The associated kinetic reaction terms are defined by

$$R_{Mg^{2+}} = -v_{Mg^{2+}} G_r, \quad R_{Ca^{2+}} = -v_{Ca^{2+}} G_r, \quad R_{CO_3^{2-}} = -v_{CO_3^{2-}} G_r,$$

indicating that these species are consumed during the precipitation process.

This formulation ensures that the reaction dynamics are consistently incorporated into the multicomponent transport model, allowing the simulation to capture the complex interactions between chemical reactions and contaminant transport in porous media. At a temperature of 25°C, the solubility constant of $MgCO_3$ is taken as 6.82×10^{-6}, which is used to characterize the equilibrium condition of the system.

The above kinetic reaction formulation is incorporated into the multicomponent transport equation through the reaction term $R_\alpha(\mathbf{c})$ in Equation (4.3). For each species α, this term represents the local rate of production or consumption caused by chemical interactions among dissolved and solid components. As a result, the transport equation accounts not only for advection and diffusion, but also for concentration changes induced by kinetically controlled reactions. In the case of mineral precipitation, such as the formation of $CaMg(CO_3)_2(s)$, the

reaction term becomes nonlinear and depends on the concentrations of the reactive species, the reaction rate constant, and the reactive surface area. Consequently, Equation (4.3) provides a fully coupled reactive transport model in which the spatial and temporal evolution of each component is governed by the combined effects of groundwater flow, dispersion, pumping, and chemical transformation.

The discretize overall fitness function is defined as follows

$$f_1(\mathbf{P}_{\gamma_l}) = \sum_{s=1}^{n_{ob}} \sum_{\gamma=n_e+1}^{n_c} \sum_{n=1}^{N_t} \omega_{\gamma_s} [C_{\gamma_s}(\mathbf{P}_{\gamma_l}, t^n) - C_{\gamma_s}^{ob}(t^n)]^2 \Delta t. \tag{4.37}$$

The $f_1(\mathbf{r}_{\gamma_l})$ function represents the concentration least squares error that defines the overall fitness between the simulated concentrations $c_{\gamma_s}(\mathbf{r}_{\gamma_l}, t)$ and the concentrations $c_{\gamma_s}^{ob}(t)$ at the observation sites with weight ω_{γ_s}. The allowable environmental concentrations $c_{\gamma_s}^{ob}(t)$ are perturbed from the ideal concentration at minimum injection rates.

Table 4.1: Physical and chemical parameters used in the numerical simulations.

Parameter	**Symbol**	**Value**	**Unit**
Storage coefficient	S_s	3×10^{-5}	–
Effective porosity	ϕ	0.35	–
Hydraulic conductivity (x)	K_x	5.2	m/day
Hydraulic conductivity (y)	K_y	4.2	m/day
Diffusion coefficient (x)	D_x	5×10^{-2}	m^2/day
Diffusion coefficient (y)	D_y	3×10^{-2}	m^2/day
Reaction rate constant	k	100	mol m^{-2} day^{-1}
Effective surface area	S_e	50	m^{-1}

Table 4.3 presents the optimal reduction rates for the injected components under three spatial configurations of injection locations, denoted by G_1, G_2, and G_3, as described in Table 4.2. These configurations represent different geometric arrangements of pollution sources along the upstream boundary of the aquifer. The objective function first considered in this experiment is the concentration matching error f_1, which measures the deviation between simulated concentrations and the prescribed target concentrations at the observation wells.

Table 4.2: Injection locations case description.

Case	$l = 1$	$l = 2$	$l = 3$	$l = 4$
G_1	[250m 280m]	[310m 340m]	[370m 400m]	[430m 460m]
G_2	[20m 70m]	[250m 300m]	[310m 360m]	[370m 420m]
G_3	[20m 70m]	[90m 140m]	[400m 450m]	[460m 510m]

For Table 4.3, we consider the four injection locations on the top boundary of the left half domain. They are located between [250m 280m], [310m, 340m], [370m, 400m], and [430m, 460m] respectively. We consider the injection rates range at four different injection locations for Mg^{2+} ions, [0.1 0.8] and for Cl^{-} ions, [0.2 0.9]. We consider the pollutions are injected for 360 days. In Table 4.3, the column labeled $r_{\gamma,l}$ denotes the reduction-rate variable associated with pollutant species γ at injection location l. The column *range* specifies the allowable interval within which the reduction rate is optimized, representing the feasible treatment efficiency bounds for each injection location.

Table 4.3: Numerical simulations-optimization results of Mg^{2+}, Ca^{2+} and Cl^{-} reduction rates for different injection location for the objective function f_1 evaluated with 10 parallel processors.

	r_{γ_l}	RR range	ARR	Mg^{2+} *Opt r*	Ca^{2+} *Opt r*	Cl^{-} *Opt r*	Obj. Val.	CPU
G_1	r_{γ_1}	[0.07 0.7]	0.50	0.63	0.63	0.26	0.0239	10h 6m
	r_{γ_2}	[0.07 0.7]	0.50	0.56	0.58	0.38		
	r_{γ_3}	[0.09 0.9]	0.50	0.09	0.09	0.65		
	r_{γ_4}	[0.09 0.9]	0.50	0.81	0.81	0.61		
G_2	r_{γ_1}	[0.07 0.7]	0.50	0.63	0.63	0.57	0.1956	10h 8m
	r_{γ_2}	[0.07 0.7]	0.50	0.39	0.54	0.51		
	r_{γ_3}	[0.09 0.9]	0.50	0.19	0.09	0.30		
	r_{γ_4}	[0.09 0.9]	0.50	0.90	0.90	0.63		
G_3	r_{γ_1}	[0.07 0.7]	0.50	0.39	0.63	0.43	0.0373	10h 9m
	r_{γ_2}	[0.07 0.7]	0.50	0.53	0.29	0.52		
	r_{γ_3}	[0.09 0.9]	0.50	0.68	0.72	0.66		
	r_{γ_4}	[0.09 0.9]	0.50	0.39	0.35	0.39		

The column *ARR* represents the actual reduction rate associated with the observation concentrations used as targets in the optimization process. The column *Opt r* indicates the

optimal reduction rate obtained by the parallel Differential Evolution algorithm for each pollutant species. The column $Obj.\ Val.$ reports the final value of the objective function f_1, which measures the least-squares error between the simulated concentrations and the observed concentrations at the monitoring locations. Finally, the column CPU records the computational time required to complete the optimization process using 10 parallel processors, providing an indication of the computational efficiency of the proposed DE-PDE framework. We consider the four observation points are $O_1 = (700,\ 18.5)$, $O_2 = (700,\ 16)$, $O_3 = (800,\ 18.5)$ and $O_4 = (800,\ 16)$. We consider ARR at the observation location to find $C^*_{\gamma_s}$ with the noise $\zeta = 0.1$. The net volumetric flow rate $q_w = 2,\ w = 1,\ 2$. We use the spatial step sizes are $\Delta x = \Delta y = 1m$ and the time step size as $\Delta t = 1day$. The parameter values are given in Table 4.1. The injected locations case description is given in Table 4.2. In the DE algorithm, we consider a total population size of 100, a maximum of 250 generations, and a tolerance of 10^{-3}.

The results in Table 4.3 show that both the optimal reduction rates (Opt-r) and the corresponding objective function values (Obj. Val.) vary significantly under the three spatial configurations G_1, G_2, and G_3. For configuration G_1, the optimal reduction rates at the four injection locations are (0.63, 0.56, 0.09, 0.81) for Mg^{2+} and (0.63, 0.58, 0.09, 0.81) for Ca^{2+}, while the optimal reduction rates for Cl^- are (0.26, 0.38, 0.65, 0.61). This configuration produces the smallest objective function value of 0.0239, indicating that the optimized reduction rates provide the best agreement between the simulated and target concentrations at the observation wells.

For configuration G_2, the optimal reduction rates are (0.63, 0.39, 0.19, 0.90) for Mg^{2+} and (0.63, 0.54, 0.09, 0.90) for Ca^{2+}, while the values for Cl^- are (0.57, 0.51, 0.30, 0.63). Compared with G_1, these values show larger variability among the injection locations, and this configuration yields the largest objective function value of 0.1956, indicating that the optimized reduction rates are less effective in reproducing the prescribed concentration patterns.

In configuration G_3, the optimal reduction rates are (0.39, 0.53, 0.68, 0.39) for Mg^{2+} and (0.63, 0.29, 0.72, 0.35) for Ca^{2+}, while the values for Cl^- are (0.43, 0.52, 0.66, 0.39). The corresponding objective function value is 0.0373, which is slightly larger than that of G_1 but significantly smaller than that of G_2. These results indicate that configuration G_3 provides a moderate level of agreement between the simulated and observed concentrations. Overall, the comparison of the optimal reduction rates and objective function values demonstrates that the spatial configuration of injection locations strongly influences the effectiveness of the optimization process, with configuration G_1 providing the most accurate match to the observation data among the three cases.

We then consider the combined objective function of $f_1 + f_2$ in the next experiment.

The discrete cost function, $f_2(\mathbf{r}_{\gamma,l})$ refers to the reduction costs at all contaminated sites.

$$f_2(\mathbf{r}_{\gamma,l}) = \sum_{l=1}^{n_s} \sum_{\gamma=n_e+1}^{n_c} \sum_{t=0}^{T} \omega_2 z_l A_{\gamma,l}(\mathbf{r}_{\gamma,l}) dt \tag{4.38}$$

The reduction rate (treatment efficiency), $\mathbf{r}_{eff,l} = \dfrac{\sum_{\gamma=n_e+1}^{n_c} C^*_{\gamma,l} \mathbf{r}_{\gamma,l}}{\sum_{\gamma=n_e+1}^{n_c} C^*_{\gamma,l}}$

$$A_{\gamma,l}(r_{\gamma,l}) = \left(b_{1,l} (c^*_{\gamma,l})^{b_{2,l}} + b_{3,l} (c^*_{\gamma,l})^{b_{2,l}} \mathbf{r}_{eff,l}^{b_{4,l}} \right), \qquad \forall\, r.$$

and the coefficient values of the cost function listed in Table 4.4.

Table 4.4: The values of the cost function coefficients.

Coefficient:	b_1	b_2	b_3	b_4	b_5	b_6
Value:	0.7945	0.5733	2.500	4.000	10.000	2.000

Table 4.5 shows the influence of injection-well placement and reduction-rate ranges on the optimal pollutant reduction strategies when both the concentration matching error and the abatement cost are considered in the objective function $f_1 + f_2$. Three spatial scenarios

are examined to evaluate how the relative location of injection wells with respect to the observation points affects the optimization results. In Case I, the injection wells are located upstream of the observation points, allowing the injected pollutants to travel through the aquifer before reaching the monitoring locations. In Case II, no injection wells are present at the designated well locations, which serves as a reference scenario to evaluate the influence of injection activities. In Case III, the injection wells are located between the observation points, representing a configuration where contaminants may reach the monitoring locations more directly. In addition, two groups of reduction-rate ranges are considered to reflect different treatment efficiency limits and operational constraints.

Table 4.5 is generated using 10 parallel processors. A population size of 80, a maximum of 250 generations, and a tolerance level of 10^{-2} are employed. We consider same four injection locations are placed on the top boundary of the left half of the domain and four observation points inside the domain. At these four injection locations, denoted by r_{γ_1}, r_{γ_2}, r_{γ_3}, and r_{γ_4}, two groups of reduction-rate ranges are considered. For the first group, the reduction-rate interval [0.1, 0.9] is applied to all injected components at all injection locations, with the assumed initial reduction rate set to 0.1. For the second group, different reduction-rate intervals are specified for each pollutant species: [0.04, 0.4], [0.06, 0.6], and [0.08, 0.8] for Mg^{2+}, Ca^{2+}, and Cl^{-} ions, respectively. The corresponding actual reduction rates (ARR) are 0.80, 0.33, 0.70, and 0.50. The ARR values at the observation locations are used to generate the target concentrations $C^{ob}_{\gamma_s}$ with noise $\zeta = 0.1$. The pollutants are injected continuously for a period of 360 days. The net volumetric flow rate is taken as $q_w = 2$ for $w = 1, 2$.

The optimization results in table 4.5 illustrate that the optimal reduction rates (Opt r) vary across the three spatial configurations of injection wells, namely Case I, Case II, and Case III. For the wider reduction-rate range [0.1, 0.9], the optimal reduction rates for Mg^{2+} in Case I are (0.44, 0.52, 0.58, 0.59) at the four injection locations r_{γ_1}, r_{γ_2}, r_{γ_3}, and r_{γ_4}, respectively. In comparison, the corresponding values in Case II are (0.59, 0.48, 0.44, 0.53), while in Case III

Table 4.5: Numerical simulations-optimization results of Mg^{2+}, Ca^{2+} and Cl^{-} reduction rates for extraction well locations for the objective function $f_1 + f_2$ evaluated with 10 parallel processors.

γ	r_{γ_l}	RR range	AIR	*Case I* *Opt r*	*Case II* *Opt r*	*Case III* *Opt r*
Mg^{2+}	r_{γ_1}	[0.1 0.9]	0.80	0.44	0.59	0.45
		[0.04 0.4]	0.33	0.22	0.24	0.14
	r_{γ_2}	[0.1 0.9]	0.10	0.52	0.48	0.47
		[0.06 0.6]	0.50	0.31	0.34	0.31
	r_{γ_3}	[0.1 0.9]	0.80	0.58	0.44	55.00
		[0.08 0.8]	0.70	0.40	0.43	0.44
	r_{γ_4}	[0.1 0.9]	0.80	0.59	0.53	0.61
		[0.1 0.9]	0.50	0.55	0.48	0.53
Ca^{2+}	r_{γ_1}	[0.1 0.9]	0.80	0.52	0.60	0.51
		[0.04 0.4]	0.33	0.24	0.24	0.25
	r_{γ_2}	[0.1 0.9]	0.80	0.53	0.57	0.59
		[0.06 0.6]	0.50	0.23	0.15	0.39
	r_{γ_3}	[0.1 0.9]	0.80	0.48	0.50	0.52
		[0.08 0.8]	0.70	0.40	0.49	0.38
	r_{γ_4}	[0.1 0.9]	0.80	0.47	0.58	0.62
		[0.1 0.9]	0.50	0.49	0.52	0.53
Cl^{-}	r_{γ_1}	[0.1 0.9]	0.80	0.46	0.62	0.55
		[0.04 0.4]	0.30	0.10	0.19	0.23
	r_{γ_2}	[0.1 0.9]	0.80	0.58	0.55	0.34
		[0.06 0.6]	0.50	0.41	0.36	0.37
	r_{γ_3}	[0.1 0.9]	0.80	0.65	0.56	0.39
		[0.08 0.8]	0.70	0.47	0.47	0.37
	r_{γ_4}	[0.1 0.9]	0.80	0.61	0.62	0.53
		[0.1 0.9]	0.50	0.57	0.59	0.63
Time :				$7h\ 10m$	$7h\ 02m$	$7h\ 16m$

they are (0.45, 0.47, 0.55, 0.61). Similar variations are observed for Ca^{2+} and Cl^{-} ions, indicating that the optimal reduction rates depend strongly on the spatial configuration of the injection wells.

The differences in the optimal reduction rates among the three cases arise primarily from the relative positions of the injection wells and the observation points, which influence the contaminant transport pathways in the aquifer. In Case I, the injection wells are located

upstream of the monitoring locations, allowing the injected pollutants to travel through a longer portion of the aquifer before reaching the observation wells. This longer transport distance enhances advection, dispersion, and chemical reaction processes, which naturally attenuate contaminant concentrations and therefore require more moderate reduction rates. In contrast, in Case III the injection wells are located between the observation points, which shortens the transport distance and allows contaminants to reach the monitoring locations more directly. As a result, higher reduction rates may be required at certain injection locations to satisfy the concentration constraints. Case II serves as a reference configuration where injection activity is absent at the designated well locations, highlighting the influence of injection-well placement on the resulting optimal reduction strategies.

For the narrower reduction-rate ranges, the optimal values decrease but remain within the prescribed bounds. For example, in Case I the optimal reduction rates for Mg^{2+} become (0.22, 0.31, 0.40, 0.55) under the respective intervals [0.04, 0.4], [0.06, 0.6], [0.08, 0.8], and [0.1, 0.9]. Similar patterns are observed for Ca^{2+} and Cl^{-}, although the exact magnitudes differ due to species-specific transport and reaction behaviours. These results demonstrate that both the feasible reduction-rate intervals and the spatial placement of injection wells play important roles in determining the optimal remediation strategy and the resulting contaminant distribution in the aquifer.

Table 4.6 investigates the influence of hydraulic boundary conditions on the optimal pollutant reduction strategies. In this experiment, two different left boundary hydraulic heads, $h_{\text{left}} = 100\,\text{m}$ and $h_{\text{left}} = 300\,\text{m}$, are considered while the right boundary hydraulic head remains fixed at $h_{\text{right}} = 20\,\text{m}$. Changing the hydraulic head at the upstream boundary alters the hydraulic gradient within the aquifer and consequently affects the groundwater flow velocity and contaminant transport behaviour. Since the groundwater velocity is governed by Darcy's law, variations in the hydraulic gradient directly influence the rate at which pollutants migrate through the porous medium.

Table 4.6: Numerical simulations-optimization results of Mg^{2+}, Ca^{2+} and Cl^{-} reduction rates for different hydraulic heads for the objective function $f_1 + f_2$ evaluated with 10 parallel processors.

γ	r_{γ_l}	RR range	AIR	$h_{left} = 300m$ *Opt r*	$h_{left} = 100m$ *Opt r*
Mg^{2+}	r_{γ_1}	[0.1 0.9]	0.80	0.44	0.61
		[0.04 0.4]	0.30	0.22	0.17
	r_{γ_2}	[0.1 0.9]	0.80	0.52	0.62
		[0.06 0.6]	0.50	0.31	0.28
	r_{γ_3}	[0.1 0.9]	0.80	0.58	0.71
		[0.08 0.8]	0.70	0.40	0.58
	r_{γ_4}	[0.1 0.9]	0.80	0.59	0.68
		[0.1 0.9]	0.50	0.54	0.67
Ca^{2+}	r_{γ_1}	[0.1 0.9]	0.80	0.52	0.64
		[0.04 0.4]	0.30	0.24	0.24
	r_{γ_2}	[0.1 0.9]	0.80	0.53	0.64
		[0.06 0.6]	0.50	0.35	0.39
	r_{γ_3}	[0.1 0.9]	0.80	0.48	0.61
		[0.08 0.8]	0.70	0.45	0.52
	r_{γ_4}	[0.1 0.9]	0.80	0.47	0.64
		[0.1 0.9]	0.50	0.48	0.57
Cl^{-}	r_{γ_1}	[0.1 0.9]	0.80	0.46	0.68
		[0.04 0.4]	0.30	0.10	0.18
	r_{γ_2}	[0.1 0.9]	0.80	0.58	0.63
		[0.06 0.6]	0.50	0.41	0.43
	r_{γ_3}	[0.1 0.9]	0.80	0.65	0.68
		[0.08 0.8]	0.70	0.47	0.43
	r_{γ_4}	[0.1 0.9]	0.80	0.61	0.65
		[0.1 0.9]	0.50	0.57	0.62
Time :				$6h\ 30m$	$6h\ 27m$

Table 4.6 shows that the optimal reduction rates (Opt r) generally increase in the case $h_{\text{left}} = 100\,\text{m}$ compared with the case $h_{\text{left}} = 300\,\text{m}$ for most components and injection locations. For Mg^{2+}, the optimal reduction rates under $h_{\text{left}} = 300\,\text{m}$ are (0.44, 0.52, 0.58, 0.59) for the wider reduction-rate ranges and (0.22, 0.31, 0.40, 0.54) for the narrower ranges at the four injection locations r_{γ_1}, r_{γ_2}, r_{γ_3}, and r_{γ_4}. In contrast, under $h_{\text{left}} = 100\,\text{m}$ the corresponding values increase to (0.61, 0.62, 0.71, 0.68) and (0.17, 0.28, 0.58, 0.67), indicating that stronger

reduction is required at several injection locations.

A similar trend is observed for Ca^{2+}. Under $h_{\text{left}} = 300\,\text{m}$ the optimal reduction rates are (0.52, 0.53, 0.48, 0.47) for the wider ranges and (0.24, 0.35, 0.45, 0.48) for the narrower ranges, while for $h_{\text{left}} = 100\,\text{m}$ these values increase to (0.64, 0.64, 0.61, 0.64) and (0.24, 0.39, 0.52, 0.57). For the Cl^- component, which behaves more conservatively during transport, the optimal reduction rates are relatively large in both hydraulic conditions. In the case $h_{\text{left}} = 300\,\text{m}$, the optimal reduction rates are (0.46, 0.58, 0.65, 0.61) and (0.10, 0.41, 0.47, 0.57) for the two reduction-rate ranges. These values increase to (0.68, 0.63, 0.68, 0.65) and (0.18, 0.43, 0.43, 0.62) when $h_{\text{left}} = 100\,\text{m}$.

Overall, the case with $h_{\text{left}} = 100\,\text{m}$ requires generally higher optimal reduction rates for most components, indicating a more intensive remediation strategy compared with the case $h_{\text{left}} = 300\,\text{m}$. These differences highlight the influence of hydraulic boundary conditions on the contaminant transport dynamics and demonstrate that variations in the hydraulic gradient can significantly affect the optimal pollution control strategies.

Example 2: This experiment extends study to consider a more complex multicomponent reactive transport system by a multi-contour optimization problem. The optimization is performed using three objective function configurations: f_1, $f_1 + f_2$, and $f_1 + f_3$, representing concentration matching, abatement cost, and pumping cost, respectively. This setup allows for a systematic investigation of the trade-offs between environmental accuracy and operational efficiency, and demonstrates how different objective formulations affect the optimal control strategies and contaminant plume behaviour.

We consider a six components reactive groundwater system consisting of an existing aqueous species C_{H^+} and multiple injected contaminants $C_{SO_4^{2-}}$, C_{Na^+}, $C_{Ca^{2+}}$, $C_{Fe^{3+}}$ and C_{Cl^-}. Carbonate species associated with water (H_2O) are assumed to be initially distributed throughout the aquifer, whereas the remaining ions are continuously introduced through specified injection segments located along the upper boundary. The computational domain is

a two-dimensional vertical aquifer $\Omega = [0,\, 1000m] \times [0,\, 100m]$, and the simulation horizon is one year. Contaminant loading is applied as a sustained boundary flux along the designated top-boundary injection regions.

The simultaneous presence of multiple ionic species promotes coupled geochemical interactions that strongly influence contaminant migration and attenuation. In particular, precipitation reactions between selected ions alter concentration distributions and transport pathways within the aquifer. The present experiment therefore simulates multicomponent reactive transport dominated by precipitation processes, providing a realistic setting for evaluating the effectiveness of the proposed parallel optimization framework in controlling groundwater contamination.

The six-component reactive system considered in this experiment includes precipitation processes among selected ions. In particular, sulfate–calcium interaction leads to gypsum formation, while ferric iron undergoes hydrolysis and precipitation according to the following stoichiometric relations [114]

$$Ca^{2+} + SO_4^{2-} \rightarrow CaSO_4;$$

$$Fe^{3+} + 3H_2O \rightarrow Fe(OH)_3 + 3H^+.$$

These reactions govern the coupling among species and influence the spatial evolution of contaminant concentrations within the aquifer.

Table 4.8 summarizes the optimal pollutant reduction rates obtained for two protected-zone configurations. Two injection segments are prescribed along the upper boundary of the left half of the domain, located over the intervals $[30m\, 130m]$, and $[150m,\, 250m]$. The imposed boundary concentrations for the injected species are $C^*_{SO_4^{2-}} = 0.9$, $C^*_{Na^+} = 0.2$, $C^*_{Ca^{2+}} = 0.9$, $C^*_{Fe^{3+}} = 0.9$ and $C^*_{Cl^-} = 0.15$. Two pumping wells are positioned at $(600m\, 95m)$, and $(600m,\, 40m)$, each operating at a fixed extraction rate $q_w = 10$, $w = 1,\, 2$. Continuous pollutant injection is applied for a period of 360 days.

ARR denotes the prescribed (actual) reduction rate used to generate the synthetic obser-

vation concentrations, whereas Opt r denotes the optimal reduction rate estimated by the optimization procedure. The observation data $C_{\gamma_s}^{obs}$ are constructed from ARR solutions with an added noise level $\zeta = 0.5$. The numerical discretization employs uniform spatial steps $\Delta x = \Delta y = 1m$ and time step $\Delta t = 1day$, with hydro-chemical parameters given in Table 4.1. The parallel DE-PDE algorithm uses a population size of 100, a maximum of 150 generations, and a convergence tolerance of 10^{-4}. Each simulation is executed on 10 processors, and the objective function considered in this experiment is solely f_1.

Table 4.8 present the optimized reduction rates of the injected ions SO_4^{2-}, Na^+, Ca^{2+}, Fe^{3+} and Cl^- at two injection locations under two spatial configurations, denoted as $Case\ I$ and $Case\ II$.

Table 4.7: Observation locations description.

$Case\ I$	$Case\ II$
$O_1 : (700m,\ 95m)$	$O_1 : (450m,\ 95m)$, $O_3 : (700m,\ 95m)$, $O_5 : (850m,\ 95m)$
$O_2 : (700m,\ 40m)$	$O_2 : (450m,\ 40m)$, $O_4 : (700m,\ 40m)$, $O_6 : (850m,\ 40m)$

The fitness objective function f_1 is considered in Table 4.8,. A convergence tolerance of 0.2 is approximately achieved after 60 generations for $Case\ I$ and 133 generations for $Case\ II$, indicating that the larger protected-zone configuration imposes a more restrictive and computationally demanding optimization problem.

Table 4.8: Numerical optimization results of reduction rates for SO_4^{2-}, Na^-, Ca^{2+}, Fe^{3+} and Cl^- under different protected-zone configurations for the objective function f_1 evaluated with 10 parallel processors.

		$Opt\ r$ of Components (γ)					Obs.		CPU
	$r_{\gamma,l}$	Na^+	SO_4^{2-}	Ca^{2+}	Fe^{3+}	Cl^-	Val.	iter.	
	range(%)	[10 90]	[10 95]	[10 95]	[10 99]	[10 99]			
	ARR (%)	50.0	50.0	50.0	50.0	50.0			
$Case\ I$	$r_{\gamma,1}(\%)$	90.0	94.7	94.1	17.7	88.2	0.377	60	$11\,hr$
	$r_{\gamma,2}(\%)$	21.1	36.7	36.8	65.9	23.1			$43\,m$
$Case\ II$	$r_{\gamma,1}(\%)$	49.5	95.0	95.0	52.6	48.8	0.383	133	$26\,hr$
	$r_{\gamma,2}(\%)$	50.4	33.1	33.0	48.4	51.4			$20\,m$

For the Na^+ ion, the optimized reduction rates across both configurations remain close to the prescribed actual reduction rate (ARR = 50 %), indicating that moderate intensity control is sufficient to satisfy concentration constraints. For $Case\ I$, the optimal reduction is highly asymmetric between injection locations, reaching about 90 % at the downstream segment and only 21 % upstream. This reflects stronger suppression near observation wells due to the shorter transport distance to monitoring points. In $Case\ II$, the optimized reductions become nearly uniform (49.5 % downstream and 50.4 % upstream), showing that the expanded protected zone enforces balanced control over the plume footprint.

A similar spatial trend is observed for the reactive pair SO_4^{2-} and Ca^{2+}. For $Case\ I$, both species exhibit very high downstream reductions (94–95 %) and substantially lower upstream reductions (33–37 %), indicating strong localized suppression near observation wells. In $Case\ II$, the downstream reductions remain high (95 %), while upstream values remain moderate (33 %). The close agreement between sulfate and calcium reduction rates across both locations confirms the chemical coupling imposed by their precipitation reaction, which constrains their optimal control to evolve synchronously.

For the Fe^{3+} ion, the optimized reduction rates across configurations $case\ I$ to $case\ II$ generally remain around the actual reduction rate, implying effective control through reduced intensity. In configuration $Case\ I$, the r rates are relatively lower, ranging from approximately 17.7 % at the downstream location and lower at the upstream location, 65.9 %, suggesting stronger injection suppression due to shorter pollutant travel distances between the injection locations and observation wells. In configuration $Case\ II$, the r rates are relatively mid—ranging from approximately 52.6 % at the downstream location and at the upstream location 48.4 %, suggesting a stronger connection with the observation location due to intense and large protected zones.

For Fe^{3+}, the optimized reductions show a distinct spatial pattern compared with sulfate and calcium. In $Case\ I$, the downstream reduction is relatively low (17.7 %), whereas the

upstream reduction is higher (65.9 %). This reversal indicates that ferric transport and hydrolysis are less sensitive to downstream observation constraints and more influenced by upstream plume evolution. In $Case\ II$, both locations converge to intermediate values (52.6 % downstream and 48.4 % upstream), reflecting the homogenizing effect of the larger protected zone on ferric control requirements.

For the Cl^- ion, the optimized reduction rates across configurations $Case\ I$, to $Case\ II$ generally remain around the actual reduction rate, implying effective control through reduced intensity. In configuration $Case\ I$, the r rates are relatively high, ranging from approximately 88.2 % at the downstream location and lower at the upstream location, 23.1 %, suggesting stronger injection suppression due to shorter pollutant travel distances between the injection locations and observation wells. In configuration $Case\ II$, the r rates are relatively mid—ranging from approximately 48.8 % at the downstream location and at the upstream location 51.4 %, suggesting a stronger connection with the observation location due to intense and large protected zones. The conservative ion Cl^- exhibits behaviour similar to Na^+, with strong downstream suppression in Case I (88.2 %) and weak upstream control (23.1 %), followed by nearly symmetric reductions in Case II (48.8 % and 51.4 %). This pattern is consistent with non-reactive transport, where spatial proximity to observation wells primarily governs the optimal reduction distribution.

Numerical results in Table 4.8 show that the spatial configuration of protected zones strongly influences optimal injection-reduction strategies. A localized monitoring layout ($Case\ I$) leads to highly non-uniform reduction rates dominated by downstream control, whereas an expanded protected zone ($Case\ II$) promotes more balanced reductions across injection locations. These results confirm that both hydro-transport geometry and geochemical coupling play critical roles in determining optimal contaminant-reduction strategies within the proposed PDE-constrained optimal control model.

Next, Table 4.10 presents the optimized reduction rates of the injected ions SO_4^{2-}, Na^+, Ca^{2+},

Fe^{3+} and Cl^- at two injection locations for two observation-well configurations: shallow and deep in Table 4.9. The pumping intensity is taken to $q_w = 30$, and optimization is performed using five parallel processors. This experiment isolates the influence of observation depth and stronger hydraulic capture on the optimal multicomponent control strategy.

Table 4.9: Observation locations description.

	Shallow	*Deep*
Locations	O_1 : (700m, 95m), O_2 : (850m, 95m)	O_1 : (700m, 40m), O_2 : (850m, 40m)

Table 4.10: Optimal reduction rates of multicomponent ions SO_4^{2-}, Na^-, Ca^{2+}, Fe^{3+} and Cl^- for shallow and deep observation locations based on objective f_1 with 5 parallel processors.

		$Opt - r$ of Components (γ)					Obs.		CPU
	$r_{\gamma,l}$	Na^+	SO_4^{2-}	Ca^{2+}	Fe^{3+}	Cl^-	Val.	iter.	
	range(%)	[10 95]	[10 95]	[10 95]	[10 99]	[10 99]			
	ARR(%)	75.0	75.0	75.0	75.0	75.0			
Shallow	$r_{\gamma,1}$(%)	77.1	95.0	95.0	82.5	49.8	22.828	100	52 h
	$r_{\gamma,2}$(%)	51.6	50.4	41.7	74.8	99.0			4 m
Deep	$r_{\gamma,1}$(%)	90.0	49.2	35.4	99.0	99.0	5.4e−4	15	7 h
	$r_{\gamma,2}$(%)	34.7	14.2	17.1	12.4	10.0			48 m

For the shallow observation, the optimized reduction rates at the downstream injection segment ($\mathbf{r}_{\gamma,1}$) are generally high for the reactive species SO_4^{2-} and Ca^{2+} (95 %) and moderately high for Na^+ andFe^{3+} (77–83 %), while Cl^- remains moderate (50 %). At the upstream segment ($\mathbf{r}_{\gamma,2}$) reductions decrease substantially. This pattern indicates that shallow monitoring primarily constrains the near-surface plume region, where downstream injection has a stronger and more immediate influence on observed concentrations. Consequently, control remains distributed but biased toward the downstream source.

In contrast, the deep observation case exhibits a markedly different behaviour. The downstream reduction rates shift to extreme values: Na^+, Fe^{3+}, and Cl^- approach nearly complete suppression (90–99 %), whereas the reactive pair SO_4^{2-} and Ca^{2+} drop to much lower values (35–49 %). Upstream reductions simultaneously collapse toward minimal levels (10–35 % for

most species). This asymmetric pattern reflects the increased hydraulic capture imposed by $q_w = 30$, which drives contaminants downward toward deep observation wells. Under this stronger vertical transport regime, downstream injections dominate plume delivery to depth, forcing severe suppression at that location while upstream injections become less influential due to longer travel paths and dilution before reaching the monitoring depth. The coupled species SO_4^{2-} and Ca^{2+} again display closely matched optimal reductions across both configurations, confirming that their precipitation reaction constrains their control behaviour. From a computational perspective, the deep observation scenario achieves a significantly lower objective value and converges in fewer generations than the shallow case. This suggests that stronger hydraulic capture and deeper monitoring impose more deterministic plume pathways, simplifying the inverse control problem despite the more extreme optimal reductions.

Table 4.11: Observation locations description.

	$Pre.\,PW$	$Mid.\,PW$	$Post\,PW$
$Pumping\,well\,location$	$w_1 : (450m,\, 95m)$	$w_1 : (550m,\, 95m)$	$w_1 : (800m,\, 95m)$
$location$	$w_2 : (450m,\, 50m)$	$w_2 : (550m,\, 50m)$	$w_2 : (800m,\, 50m)$

Table 4.12: Optimal reduction rates of multicomponent ions SO_4^{2-}, Na^-, Ca^{2+}, Fe^{3+} and Cl^- under different pumping-well configurations based on objective f_1 evaluated with 10 parallel processors.

		$Opt - r$ of Components (γ)					Obs.		CPU
	$r_{\gamma,l}$	Na^+	SO_4^{2-}	Ca^{2+}	Fe^{3+}	Cl^-	Val.	iter.	
	range(%)	[10 90]	[10 95]	[10 95]	[10 99]	[10 99]			
	ARR(%)	50.0	50.0	50.0	50.0	50.0			
$Pre\,PW$	$r_{\gamma,1}(\%)$	90.0	18.5	23.7	66.7	77.9	0.157	36	$6\,hr$
	$r_{\gamma,2}(\%)$	47.0	42.7	42.5	49.3	48.2			$58\,m$
$Mid.\,PW$	$r_{\gamma,1}(\%)$	50.1	95.0	95.0	50.1	50.2	0.225	250	$49\,hr$
	$r_{\gamma,2}(\%)$	49.9	34.1	34.0	49.9	49.8			$14\,m$
$Post\,PW$	$r_{\gamma,1}(\%)$	52.9	40.4	40.9	44.0	52.9	0.172	170	$33\,hr$
	$r_{\gamma,2}(\%)$	47.7	49.3	48.8	52.8	48.0			$40\,m$

Table 4.8 and Table 4.10 illustrate how spatial monitoring design and hydraulic forcing jointly influence optimal contaminant-reduction strategies by the proposed PDE-constrained control

model. In Table 4.8, where observation wells are distributed horizontally within shallow regions and pumping is moderate ($q_w = 10$). The optimal reductions primarily reflect downstream proximity to monitoring points: $Case\ I$ yields highly asymmetric reductions dominated by the downstream injection segment, whereas $Case\ II$ produces more balanced reductions due to the expanded protected zone. In contrast, Table 4.10 introduces deeper observation wells and stronger hydraulic capture ($q_w = 30$), fundamentally altering plume transport pathways. Under shallow monitoring in Table 4.10, reduction patterns remain broadly similar to Table 4.8 but with generally higher magnitudes due to increased pumping. However, under deep monitoring, the optimal control becomes strongly localized at the downstream injection segment, with near-complete suppression for mobile species and reduced sensitivity for reactive species whose precipitation limits vertical migration. Thus, while Table 4.8 demonstrates the influence of horizontal protected-zone extent on reduction symmetry, Table 4.10 reveals that observation depth and hydraulic capture dominate vertical plume control, shifting optimal strategies from distributed regulation toward localized downstream suppression.

Further, Table 4.12 investigates the influence of pumping-well placement relative to fixed observation locations on the optimal multicomponent reduction strategy. The three pumping-well placement scenarios: pre-observation wells ($Pre.PW$), mid-observation wells ($Mid.PW$), and post-observation wells ($PostPW$) as defined in Table 4.11. The observation concentrations are generated using the prescribed actual reduction rate (ARR = 50 %) and are used as targets in the optimization. All other physical, chemical, and numerical conditions remain identical to the previous experiments, including pumping intensity $q_w = 10$ and the objective function f_1.

In the Pre-PW configuration, the downstream injection segment ($\mathbf{r}_{\gamma,1}$) shows highly uneven reductions across species. Conservative ions Na^+ and Cl^- require strong suppression (78–90 %), while the reactive pair SO_4^{2-} and Ca^{2+} xhibit very low reductions (10 %). This contrast indicates that upstream pumping captures mobile species before reaching observation points,

reducing the need to suppress reactive species whose precipitation already limits transport. At the upstream segment ($\mathbf{r}_{\gamma,2}$) reduction rates converge to moderate values (42–49 %) for all species, reflecting weaker influence on the monitored plume.

In the Mid-PW configuration, where pumping wells lie between injection and observation locations, hydraulic capture directly intercepts the plume before reaching monitoring points. As a result, both injection segments exhibit nearly symmetric reductions close to the ARR value (50 % for most species). This balanced pattern indicates that mid-domain pumping reduces spatial bias between injection locations, distributing control more uniformly across species. The coupled species SO_4^{2-} and Ca^{2+} are closely matched reductions due to precipitation coupling.

In the Post-PW configuration, with wells located downstream of the observation region, pumping no longer prevents plume arrival at monitoring points. Consequently, both injection segments must contribute to concentration control before contaminants reach the observation locations. The optimized reductions therefore become moderate and relatively uniform across species (40–53 %). Compared with Mid-PW, slightly lower downstream suppression is sufficient because post-observation pumping partially removes contaminants after they pass the monitoring zone.

From a computational perspective, Mid-PW requires the largest number of generations and CPU time, indicating that balanced plume interception produces a more complex optimization landscape than strongly upstream or downstream capture. Pre-PW and Post-PW converge faster because plume pathways and control requirements are more spatially deterministic.

Table 4.12 showss that pumping-well placement relative to observation locations is a dominant factor in determining optimal reduction strategies. Upstream wells favour selective suppression of mobile species, mid-domain wells produce balanced reductions across injection segments, and downstream wells require distributed control before plume arrival.

The discretized piecewise objective function $f_2'(r_{\gamma,l})$ is presented below,

$$f_2'(\mathbf{P}_{\gamma l}) = \sum_{l=1}^{n_s} \sum_{\gamma=n_e+1}^{n_c} \sum_{t=0}^{T} \omega_3 A'_{\gamma l}(r_{\gamma l}) dt \tag{4.39}$$

with,

$$A'_{\gamma_l}(r_{\gamma_l}) = \begin{cases} \left(b_{1,l} W_{\gamma l}^{b_{2,l}} + b_{3,l} W_{\gamma l}^{b_{2,l}} r_{\gamma l}^{b_{4,l}}\right), & for \quad r < r_c, \\ \left(b_{1,l} W_{\gamma l}^{b_{2,l}} + b_{3,l} W_{\gamma l}^{b_{2,l}} r_{\gamma l}^{b_{4,l}} + b_{5,l} W_{\gamma l}^{b_{2,l}} \left((r - r_c)_{\gamma l}^{b_{6,l}}\right)\right), & for \quad r \geq r_c. \end{cases}$$

Table 4.13 examines the effect of objective function selection on optimal multicomponent groundwater remediation. The control variables for the cases f_1 and $f_1 + f_2'$ are the reduction rates at injection locations, whereas for $f_1 + f_3$ both the reduction rates and pumping rates are optimized simultaneously. All hydro-chemical parameters and boundary conditions remain unchanged across the experiments. By comparing the objective functions f_1, $f_1 + f_2'$, and $f_1 + f_3$, this setup isolates the impact of treatment and pumping costs on the optimal remediation strategy while maintaining identical physical conditions.

The discrete pumping cost f_3 is given below,

$$f_3(Q_w) = \sum_{w=1}^{n_w} \sum_{t=0}^{T} \omega_3 a_1 z_w \frac{Q_w(t) \rho_w g H_w}{\eta} dt \tag{4.40}$$

The table 4.13 reports optimal reduction rates for two injection segments, $r_{\gamma,1}$ and $r_{\gamma,2}$, for five ions, and for the $f_1 + f_3$ case it also reports optimal pumping rates Q_1 and Q_2. The admissible reduction-rate ranges are species-dependent, the pumping range is $[1, 40]$, the prescribed ARR is mostly 75% for the ions shown, and the APR is $Q_1 = Q_2 = 20$.

Under f_1, the optimizer only attempts to match target concentrations, so the solution is driven almost entirely by plume reproduction rather than cost considerations. Consequently, several optimal reduction rates move to values that best fit the observation data, even if they are not economically moderate. For example, at the first injection segment, SO_4^{2-}

Table 4.13: Optimized injection rates of Na^+,SO_4^{2-}, Ca^-,Fe^{3+} and Cl^- for different objective functions f_1, $f_1 + f_2'$, and $f_1 + f_3$ evaluated with 10 parallel processors.

			ARR	f_1	$f_1 + f_2'$	$f_1 + f_3$
γ		range		*Opt r*	*Opt r*	*Opt r*
Na^+	$r_{\gamma_1}(\%)$	[10.0 90.0]	75.0	49.5	75.2	68.8
	$r_{\gamma_2}(\%)$	[10.0 90.0]	75.0	50.4	74.7	76.8
SO_4^{2-}	$r_{\gamma_1}(\%)$	[10.0 95.0]	75.0	95.0	58.3	85.3
	$r_{\gamma_2}(\%)$	[10.0 95.0]	75.0	33.1	51.7	21.1
Ca^{2+}	$r_{\gamma_1}(\%)$	[10.0 95.0]	75.0	95.0	64.8	81.4
	$r_{\gamma_2}(\%)$	[10.0 95.0]	75.0	33.0	54.3	43.6
Fe^{3+}	$r_{\gamma_1}(\%)$	[10.0 99.0]	75.0	52.6	48.7	72.1
	$r_{\gamma_2}(\%)$	[10.0 99.0]	50.0	48.4	88.3	75.5
Cl^-	$r_{\gamma_1}(\%)$	[10.0 99.0]	75.0	48.8	75.3	68.7
	$r_{\gamma_2}(\%)$	[10.0 99.0]	75.0	51.4	74.7	76.9
			APR	*Opt Q*	*Opt Q*	*Opt Q*
	Q_1	[1.0 40.0]	20.0	20.0	20.0	36.0
	Q_2	[1.0 40.0]	20.0	20.0	20.0	10.0
CPU:				$37h\ 09m$	$37h\ 25m$	$37h\ 57m$

and Ca^{2+} both reach 85.0%, their upper bound, while at the second segment both drop to approximately 33%. Meanwhile, Na^+ and Cl^- remain near 50% at both segments, and Fe^{3+} stays around 49%–53%. This pattern suggests that, for concentration matching alone, the first segment must strongly suppress the reactive sulfate-calcium pair, whereas the second segment can tolerate lower reductions due to attenuation by transport and reaction. Since pumping is not optimized in this case, Q_1 and Q_2 remain at the APR baseline values of $20, 20$.

By $f_1 + f_2'$, the inclusion of treatment cost penalizes high reduction rates, leading the optimizer to move away from the aggressive pattern observed under f_1. A notable change is that SO_4^{2-} and Ca^{2+} collapse to the lower bound of 50.0% at both injection segments, indicating that the model avoids costly chemical reduction for these ions. At the same time, Na^+ and Cl^- move close to the ARR target, around 74.7%–75.3%, while Fe^{3+} becomes asymmetric, with 48.7% at the first segment and 88.3% at the second. This behaviour indicates that the

optimizer reallocates treatment effort toward species and locations where reduction is more cost-effective for achieving concentration targets. Since f_2' does not include pumping as a control variable, Q_1 and Q_2 remain at $20, 20$.

In case of $f_1 + f_3$, the control strategy expands to include both reduction rates and pumping rates. The optimized pumping values are $Q_1 = 36.0$ and $Q_2 = 10.0$, indicating that the optimizer significantly increases pumping at the first well while decreasing it at the second. This asymmetry reflects that the first pumping location is more effective for plume interception, allowing the optimizer to rely more on hydraulic capture rather than chemical reduction. Consequently, the optimal reduction rates exhibit a hybrid pattern: SO_4^{2-} and Ca^{2+} remain very high at the first segment (85.0%) but drop to 50.0% at the second; Na^+ and Cl^- remain relatively high at both segments, around 68.7%–76.9%; and Fe^{3+} takes intermediate-high values of 72.1% and 75.5%. This indicates that, once pumping becomes available as an active control, the optimizer shifts part of the remediation effort from chemical reduction to hydraulic extraction, but only where pumping is most effective.

The impact of the three objective functions can be clearly observed. With f_1, the optimizer selects reduction patterns solely to match concentrations, often leading to extreme values. With $f_1 + f_2'$, costly treatment is discouraged, resulting in reduced reduction levels for certain ions and a redistribution of effort toward more cost-effective controls. With $f_1 + f_3$, the optimizer gains an additional control mechanism through pumping, enabling a coupled strategy that balances chemical reduction and hydraulic removal. This explains the significant differences observed in the optimal reduction rates ($Opt\ r$) and pumping rates ($Opt\ Q$) across the three objective formulations.

Example 3: This experiment presents a realistic groundwater contamination problem involving complex aquifer geometry and heterogeneous conditions. The multicomponent reactive transport model includes advection, diffusion, and kinetic reactions, providing a detailed representation of subsurface processes. The optimization is carried out using the

multi-control objective function $f_1 + f_2' + f_3$, incorporating concentration matching, abatement cost, and pumping cost.

We consider a conceptual L-shape aquifer whose shape closely resembles to the real aquifer that is presented in Fig. 4.2. The computational domain is defined as a two-dimensional rectangular aquifer extending 1000 m in the horizontal direction and 100 m in the vertical direction. Groundwater flow is confined to a heterogeneous, piecewise-connected corridor composed of three subregions with different vertical extents: an upstream section occupying the upper layer ($1 \leq x \leq 200m$, $65 \leq y \leq 90\,m$), a central section with a greater thickness ($200 \leq x \leq 400m$, $30 \leq y \leq 90\,m$), and a downstream section shifted to a lower layer ($400 \leq x \leq 1000m$, $30 \leq y \leq 65\,m$). Outside these regions, the medium is assumed impermeable and treated as a no-flow zone.

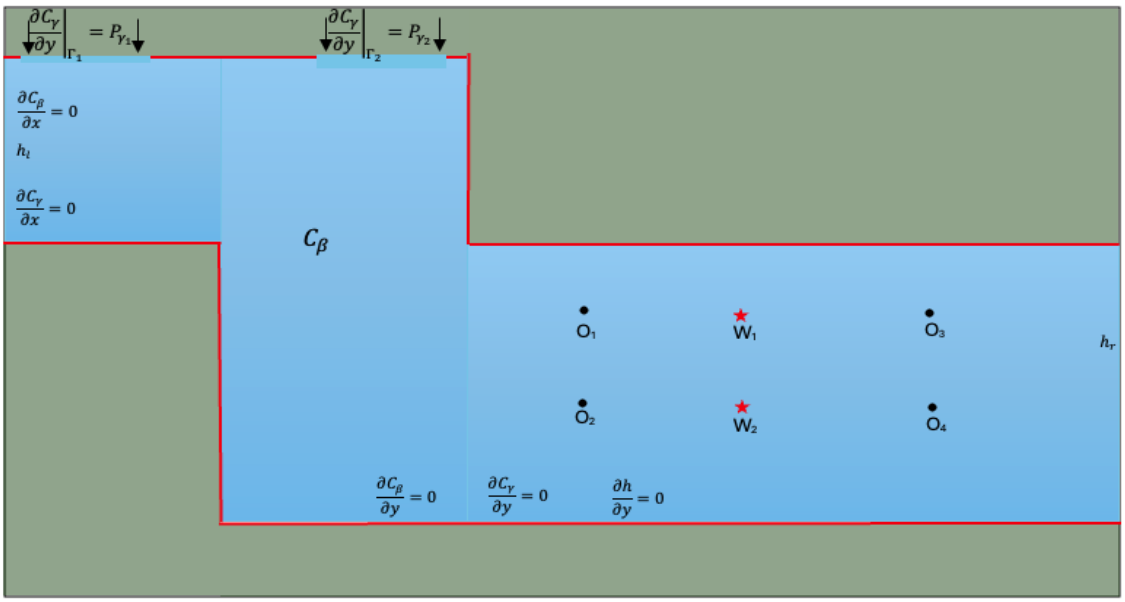

Figure 4.2: Hypothetical L-Shape vertical aquifer.

This stepped, vertically offset configuration represents a stratified aquifer with laterally varying thickness and connectivity, analogous to natural systems in which permeable layers are discontinuous and separated by low-permeability formations. The resulting geometry produces a non-uniform flow pathway with abrupt changes in vertical extent, which strongly

influences hydraulic gradients, advective transport, and reactive plume evolution within the domain. We consider the six components contamination control problem of SO_4^{2-}, Na^-, Ca^{2+}, Fe^{3+} and Cl^-. The initial condition for water head is $h_0 = 20m$ as well as the initial value for pollution concentrations C_{Na^+},$C_{SO_4^{2-}}$,$C_{Ca^{2+}}$, $C_{Fe^{3+}}$, C_{Cl^-} are zero.

Table 4.14 presents optimal reduction rates for two left-boundary hydraulic heads in the L-shaped aquifer. Contaminants are injected through two upper-boundary segments at the domain: the interval $[30, 130]$ m at $y = 65$ m, and the interval $[30, 130]$ m at $y = 90$ m with prescribed concentrations $C^*_{SO_4^{2-}} = 0.8$, $C^*_{Na^+} = 0.7$, $C^*_{Ca^{2+}} = 0.9$, $C^*_{Fe^{3+}} = 0.9$ and $C^*_{Cl^-} = 0.7$. Two pumping wells at $(500m\, 60m)$, and $(500m,\ 40m)$, each operating at a fixed extraction rate $q_w = 10$, $w = 1,\ 2$. Six protected observation points are defined at $(400m,\ 60m)$, $(400m,\ 40m)$, $(600m,\ 60m)$, $(600m,\ 40m)$, $(700m,\ 60m)$, and $(700m,\ 40m)$, with observations generated from ARR solutions with noise $\zeta = 0.5$. The DE–PDE optimization uses $\Delta x = \Delta y = 1m$ and time step $\Delta t = 1day$, total injection period 360 days, population 100, 150 generations, tolerance 10^{-4} and 10 processors. The table reports optimized reductions for SO_4^{2-}, Na^+, Ca^{2+}, Fe^{3+} and Cl^- at both injection locations for left-boundary heads of $200m$ and $400m$.

Table 4.14: Optimal reduction rates of multicomponent ions Na^+,SO_4^{2-}, Ca^-,Fe^{3+} and Cl^- for varying left-boundary hydraulic heads based on objective f_1 evaluated with 10 parallel processors.

			ARR	*Opt r* of Components (γ)					Obs.	iter.	CPU
	$r_{\gamma,l}$	range		Na^+	SO_4^{2-}	Ca^{2+}	Fe^{3+}	Cl^-	Val.		
$h_l = 200$	$r_{\gamma,1}(\%)$	[10 90]	50.0	44.3	20.1	17.1	25.3	51.1	1.24	50	$6h$
	$r_{\gamma,2}(\%)$	[10 99]	50.0	52.5	66.9	62.7	61.6	49.4			$41m$
$h_l = 400$	$r_{\gamma,1}(\%)$	[10 90]	50.0	51.2	52.9	53.3	37.9	46.3	0.46	50	$6h$
	$r_{\gamma,2}(\%)$	[10 99]	50.0	47.4	53.9	51.8	64.3	53.6			$38m$

Table 4.14 compares the optimal reduction rates of the injected ions Na^+, SO_4^{2-}, Ca^{2+}, Fe^{3+}, and Cl^- in the L-shaped aquifer under two left-boundary hydraulic head conditions, $h_{\text{left}} = 200\, m$ and $h_{\text{left}} = 400\, m$. Under the moderate-gradient scenario ($h_{\text{left}} = 200\, m$), the optimized reductions remain generally moderate and spatially asymmetric between the two

injection segments. For the conservative ion Na^+, the optimal reductions are approximately 49.5% and 50.4% at the two locations, remaining close to the prescribed ARR value. The reactive pair SO_4^{2-}-Ca^{2+} exhibits strongly coupled behaviour, with very high downstream reductions of about 95.0% and substantially lower upstream reductions of about 33.1%-33.0%, reflecting precipitation-controlled attenuation and shorter transport distance to the observation zones. The Fe^{3+} ion shows intermediate reductions of about 52.6% downstream and 48.4% upstream, indicating combined effects of hydrolysis reactions and transport. The conservative ion Cl^- displays moderate symmetric reductions of approximately 48.8% and 51.4%.

When the hydraulic head increases to $h_{\text{left}} = 400\,m$, plume migration through the confined L-shaped corridor accelerates, and the optimal control strategy shifts toward stronger downstream suppression. The reduction rates of Na^+ increase markedly to about 75.2% and 74.8% at the two injection locations. For the coupled ions SO_4^{2-} and Ca^{2+}, the downstream reduction is about 45.1%-45.0%, while the upstream reduction increases dramatically to about 92.9%, indicating redistribution of control under stronger advection. The Fe^{3+} ion exhibits reductions of approximately 43.5% and 95.5%, again showing intermediate sensitivity. The conservative ion Cl^- shows the strongest response to the increased hydraulic gradient, with reductions rising to about 42.9% and 98.3%. It shows that increasing hydraulic head significantly alters the spatial distribution and magnitude of optimal reduction rates in the heterogeneous L-shaped aquifer, with the largest sensitivity observed for conservative species and coupled reactive ions.

Then, consider the three pumping-well placement configurations defined in Table 4.15, namely pre-observation wells (Pre-PW), mid-observation wells (Mid-PW), and post-observation wells (Post-PW). These scenarios correspond to pumping wells located upstream of, within, and downstream of the protected observation region along the primary groundwater flow direction. Table 4.16 summarizes the results of the optimal pollutant reduction rates and optimal pump-

ing rates obtained under these three pumping-well placement scenarios. Three contaminant injection segments are prescribed along the upper boundary of the left portion of the domain: the interval $[30, 130]$ m at $y = 65$ m, the interval $[30, 130]$ m at $y = 90$ m, and the interval $[150, 250]$ m at $y = 90$ m. The imposed boundary concentrations for the injected species are $C^*_{SO_4^{2-}} = 0.8$, $C^*_{Na^+} = 0.7$, $C^*_{Ca^{2+}} = 0.9$, $C^*_{Fe^{3+}} = 0.9$, and $C^*_{Cl^-} = 0.7$. Component-specific admissible reduction ranges are provided in Table 4.16, and continuous contaminant injection is applied over a period of 360 days.

Four protected observation zones are considered at $(500, 60)$ m, $(500, 40)$ m, $(700, 60)$ m, and $(700, 40)$ m. Observation concentrations $C^{obs}_{\gamma,s}$ are generated from ARR-based simulations with an added noise level $\zeta = 0.5$. The optimization is performed using the parallel Differential Evolution algorithm with a population size of 100, a maximum of 150 generations, and a convergence tolerance of 10^{-2}, with each simulation executed on 10 processors. The objective function for this experiment is the combined criterion $f_1 + f_3$, incorporating both concentration fitting and pumping cost.

Table 4.15: Pumping well locations description.

Case I	*Case II*	*Case III*
$w_1 : (400m, 60m)$	$w_1 : (600m, 60m)$	$w_1 : (800m, 60m)$
$w_2 : (400m, 40m)$	$w_2 : (600m, 40m)$	$w_2 : (800m, 40m)$

In table 4.16, the pumping wells in Case I (Pre-PW) are placed before the plume reaches the observation region, so hydraulic capture can remove part of the mobile contaminant mass early. Because of that, the optimizer does not need uniform chemical suppression across all ions and all injection segments. The optimal pumping rates increase from the APR values to $Q_1 = 12.1$ and $Q_2 = 11.3$, which shows that stronger upstream extraction is beneficial despite the pumping-cost penalty. At the same time, the optimal reduction rates become highly selective: for Na^+, the values are 11.8, 49.1, and 33.6; for SO_4^{2-}, 94.1, 10.0, and 10.0; for Ca^{2+}, 36.9, 86.1, and 17.4; for Fe^{3+}, 69.3, 20.9, and 10.0; and for Cl^-, 27.4, 25.3, and 31.6. This uneven pattern means the optimizer uses upstream pumping to intercept the

plume early, then applies higher chemical reduction only where species-specific transport or reaction still makes it necessary. In particular, the strong suppression of SO_4^{2-} at the first segment suggests that this component has a strong influence on the monitored plume there, while other components can be partly controlled hydraulically.

Table 4.16: Numerical simulations-optimization results of ion reduction rates Na^+,SO_4^{2-}, Ca^-,Fe^{3+} and Cl^- for varying pumping-well locations using objective function $f_1 + f_3$ with 5 parallel processors.

				Case I	*Case II*	*Case III*
γ		range	ARR	*Opt r*	*Opt r*	*Opt r*
Na^+	$r_{\gamma_1}(\%)$	[10.0 90.0]	50.0	11.8	89.7	10.0
	$r_{\gamma_2}(\%)$	[10.0 90.0]	50.0	49.1	26.2	89.7
	$r_{\gamma_3}(\%)$	[10.0 90.0]	50.0	33.6	10.3	86.8
SO_4^{2-}	$r_{\gamma_1}(\%)$	[10.0 95.0]	50.0	94.1	83.9	10.0
	$r_{\gamma_2}(\%)$	[10.0 95.0]	50.0	10.0	15.2	14.1
	$r_{\gamma_3}(\%)$	[10.0 95.0]	50.0	10.0	37.6	73.3
Ca^{2+}	$r_{\gamma_1}(\%)$	[10.0 95.0]	50.0	36.9	68.1	10.0
	$r_{\gamma_2}(\%)$	[10.0 95.0]	50.0	86.1	84.5	20.6
	$r_{\gamma_3}(\%)$	[10.0 95.0]	50.0	17.4	19.7	75.9
Fe^{3+}	$r_{\gamma_1}(\%)$	[10.0 99.0]	50.0	69.3	95.9	64.2
	$r_{\gamma_2}(\%)$	[10.0 99.0]	50.0	20.9	22.1	98.7
	$r_{\gamma_3}(\%)$	[10.0 99.0]	50.0	10.0	11.7	17.6
Cl^-	$r_{\gamma_1}(\%)$	[10.0 99.0]	50.0	27.4	86.6	10.0
	$r_{\gamma_2}(\%)$	[10.0 99.0]	50.0	25.3	25.6	94.7
	$r_{\gamma_3}(\%)$	[10.0 99.0]	50.0	31.6	13.9	17.6
			APR	*Opt Q*	*Opt Q*	*Opt Q*
	Q_1	[2.0 20.0]	8.0	12.1	07.7	02.0
	Q_2	[2.0 20.0]	8.0	11.3	14.3	02.0
CPU:				$43h\,47m$	$43h\,46m$	$43h\,49m$

In Case II (Mid-PW), the pumping wells lie inside the monitored region, so hydraulic capture directly intercepts the plume near the protected observation points. This creates the most balanced control setting. The optimal pumping rates are $Q_1 = 7.7$ and $Q_2 = 14.3$, so the optimizer keeps one well slightly below APR and pushes the other well above APR. That asymmetry suggests the lower well or second well is more effective for the actual plume pathway in this geometry. The corresponding optimal reduction rates are more mixed than

in Case I but still reflect direct plume interception: Na^+ takes 89.7, 26.2, and 10.3; SO_4^{2-} takes 83.9, 15.2, and 37.6; Ca^{2+} takes 68.1, 84.5, and 19.7; Fe^{3+} takes 95.9, 22.1, and 11.7; and Cl^- takes 86.6, 25.6, and 13.9. Here, the optimizer still uses strong reduction at selected segments, but because pumping acts near the target zone, the burden is distributed differently than in Case I. It also notes that the Mid-PW case is computationally the most complex, which is consistent with the idea that direct plume interception creates a more balanced but harder optimization landscape.

In Case III (Post-PW), the pumping wells are located downstream of the observation region, so they cannot prevent the plume from affecting the monitored concentrations before it arrives. Because of that, pumping becomes much less useful for meeting the concentration targets, and the optimizer drives both pumping rates to their lower bounds, $Q_1 = 2.0$ and $Q_2 = 2.0$. This is a very important result: once pumping is downstream of the protected zone, spending energy on extraction gives little benefit for the objective $f_1 + f_3$, so the optimizer avoids pumping cost almost entirely. The control burden therefore shifts back to source reduction. The optimal reduction rates become: Na^+: 10.0, 89.7, 86.8; SO_4^{2-}: 10.0, 14.1, 73.3; Ca^{2+}: 10.0, 20.6, 75.9; Fe^{3+}: 64.2, 98.7, 17.6; and Cl^-: 10.0, 94.7, 17.6. These values show that when pumping cannot protect the observation zone directly, the optimizer compensates by aggressively reducing key species at the injection segments that most influence the monitored plume before it reaches the downstream wells.

So the effect of the cases on *Opt r* and *Opt Q* can be summarized clearly. In Case I, upstream pumping is useful, so *Opt Q* increases above APR and *Opt r* becomes selective because early hydraulic capture reduces the need for uniform treatment. In Case II, pumping acts closest to the monitored plume, so *Opt Q* becomes spatially imbalanced and *Opt r* reflects a coupled balance between direct hydraulic interception and species-specific chemical suppression. In Case III, downstream pumping contributes little to satisfying concentration targets before plume arrival, so both *Opt Q* values drop to the minimum and *Opt r* must do most of the

remediation work. In other words, the objective $f_1 + f_3$ does not merely penalize pumping; it chooses pumping only where well placement makes hydraulic capture effective enough to justify its cost. That is exactly why the optimal pumping and reduction patterns differ so strongly across the three cases.

Finally, we show the comparison of contamination concentration distribution with optimal reduction and pumping rates to those under minimum reduction and pumping rates in Figure 4.3, 4.4. Specifically, the injection locations are defined over the intervals $(30\,\text{m}, 130\,\text{m})$ at $y = 65\,\text{m}$, $(30\,\text{m}, 130\,\text{m})$ at $y = 90\,\text{m}$, and $(150\,\text{m}, 250\,\text{m})$ at $y = 90\,\text{m}$. This configuration creates both mid-depth and upper-layer contaminant sources, with two distinct source regions concentrated near the top boundary. Four observation points, $O_1 = (600, 60)$, $O_2 = (600, 40)$, $O_3 = (700, 60)$, and $O_4 = (700, 40)$, define the protected monitoring zone, while two pumping wells located at $w_1 = (400, 60)$ and $w_2 = (400, 40)$ provide hydraulic control upstream of the observation region.

In Figure 4.3(a), SO_4^{2-}, the left graph shows high source concentrations of 900, 630, and 630 mol/m^2 at r_1, r_2, and r_3, respectively, under minimum reduction and pumping. In the optimized right graph, these become 205, 650, and 440 mol/m^2. The strongest change occurs at r_1, where the concentration drops from 900 to 205, which is consistent with the very high optimal reduction at the first segment. The smaller reduction at r_2 explains why the concentration there stays relatively high, while the moderate decrease at r_3 reflects partial source suppression. This result shows that sulfate transport is governed by advection and dispersion, while also being coupled with reactive behaviour. Therefore, strong source reduction at the hydraulically important upstream segment reduces the mass entering the aquifer and allows the pumping wells to intercept more of the plume before it reaches the observation region.

In Figure 4.3(b), Na^+, the left graph has very high source concentrations of 1463, 640, and 640 mol/m^2, while the optimized right graph reduces them to 185, 550, and 625 mol/m^2.

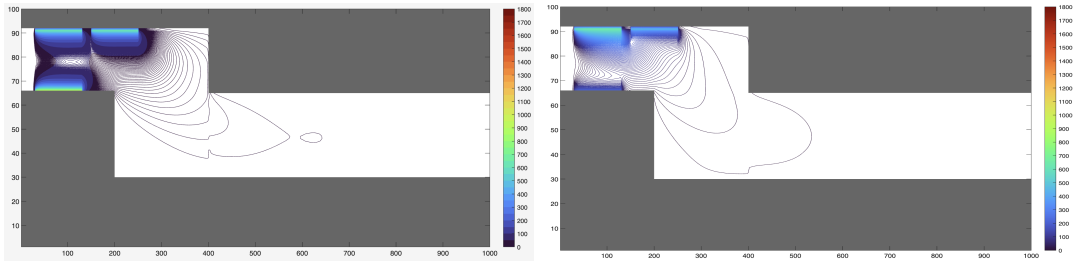

(a) $C_{SO_4^{2-}}$

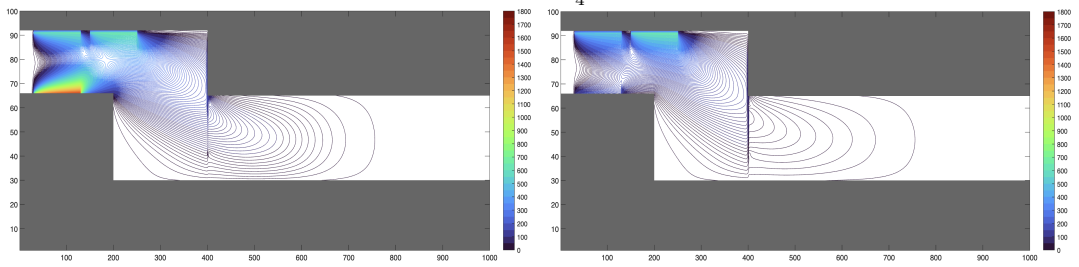

(b) C_{Na^+}

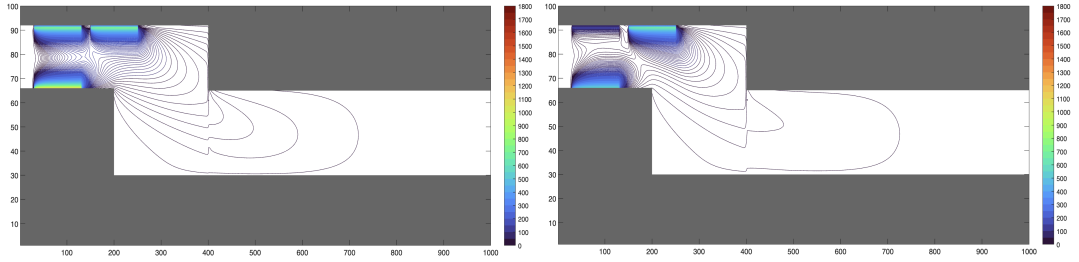

(c) $C_{Ca^{2+}}$

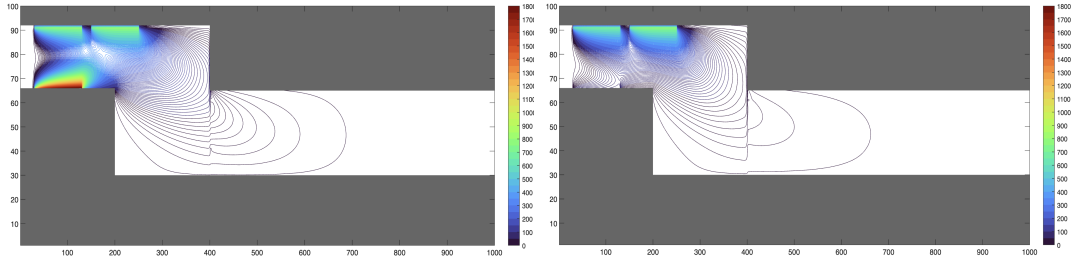

(d) $C_{Fe^{3+}}$

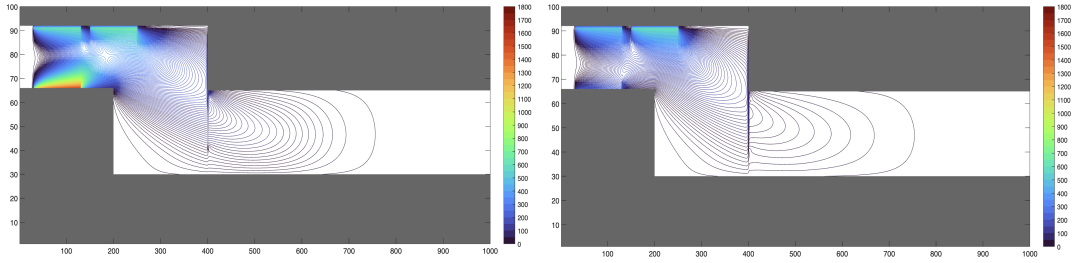

(e) C_{Cl^-}

Figure 4.3: Concentration distributions: Left column with minimum reduction rates and minimum pumping rate; Right column with optimal reduction rates and optimal pumping rate.

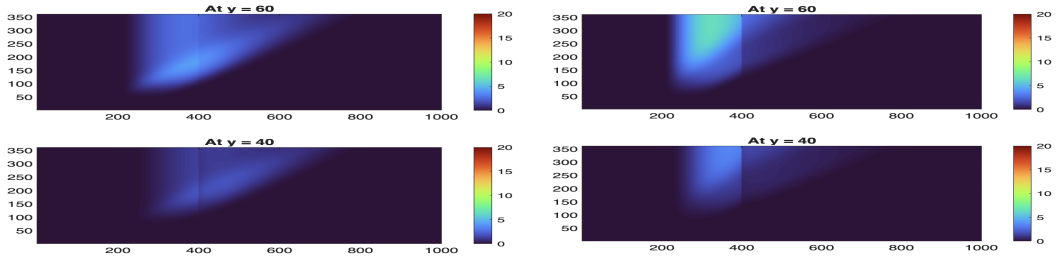

(a) $C_{SO_4^{2-}}$

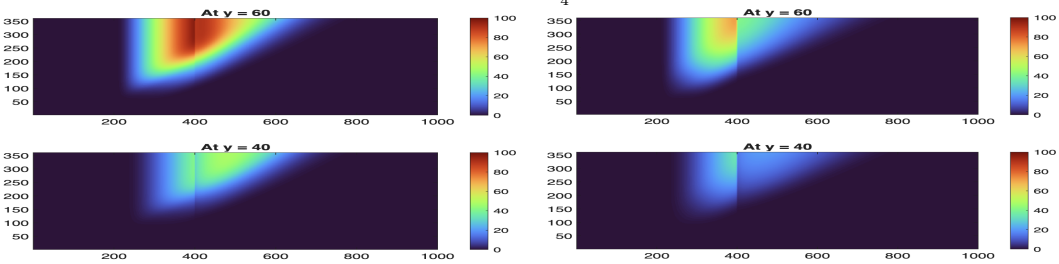

(b) C_{Na^+}

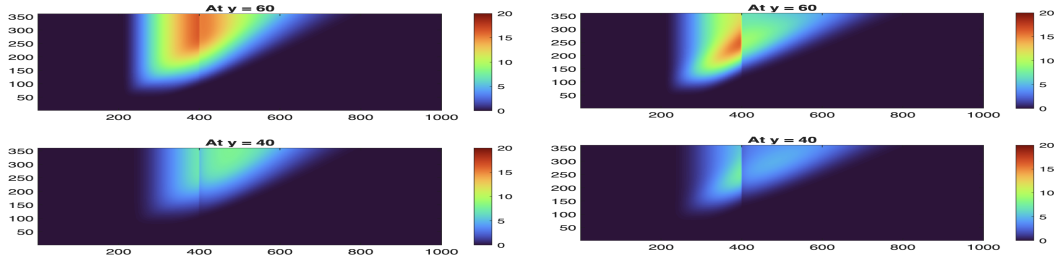

(c) $C_{Ca^{2+}}$

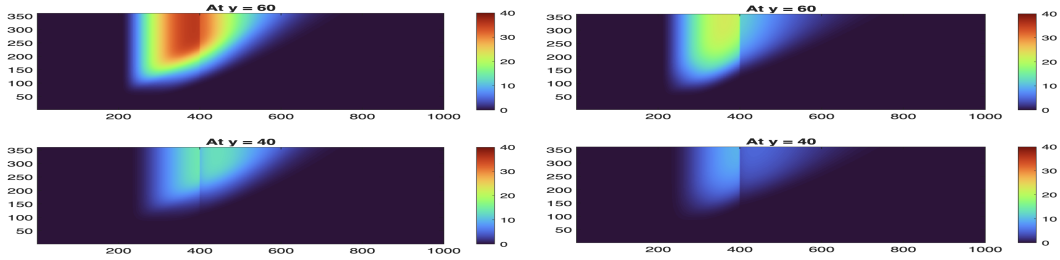

(d) $C_{Fe^{3+}}$

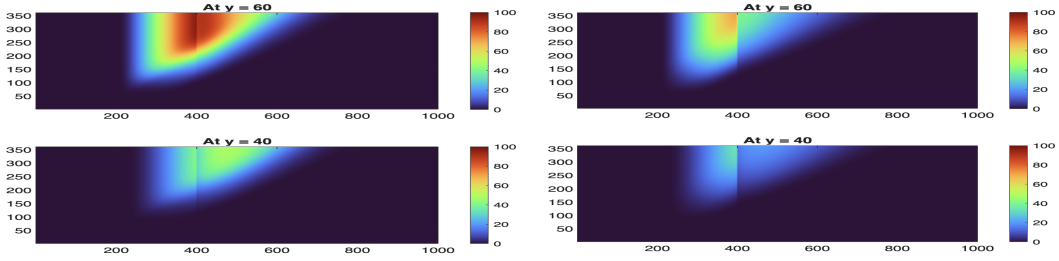

(e) C_{Cl^-}

Figure 4.4: Concentration distributions at well locations: Left column with minimum reduction rates and minimum pumping rate; Right column with optimal reduction rates and optimal pumping rate. Horizontal part of graphs show the space in x-direction and vertical part represent time.

The largest drop is again at r_1, from 1463 to 185, while the second and third segments remain fairly large. This is reasonable because the optimal reductions for sodium are not uniformly high across all segments. Since Na^+ behaves more conservatively in the groundwater flow PDE model, its transport is dominated mainly by advection and dispersion rather than strong precipitation loss. As a result, reducing sodium concentrations effectively requires either stronger source control or stronger hydraulic capture. The increase in pumping rates in the optimized case helps pull part of the dissolved sodium plume toward the wells, while the segmentwise reduction rates explain why the remaining source concentrations are still moderate at r_2 and r_3.

In Figure 4.3(c), Ca^{2+}, the left graph gives 1100, 715, and 715 mol/m^2, and the optimized case gives 550, 125, and 650 mol/m^2. The most important feature here is the drastic drop at r_2, from 715 to 125, while r_1 and r_3 remain much larger. This pattern matches the nonuniform optimal reductions and is physically meaningful in the PDE model because calcium is part of a reactive ion pair. Its spatial distribution is influenced not only by transport but also by geochemical coupling, which applying very strong reduction at one segment can substantially suppress local source loading and therefore reduce downstream calcium availability for transport and reaction. The remaining larger concentrations at r_1 and r_3 indicate that the optimizer did not need equally strong suppression there once the combined effect of pumping and spatially selective source reduction was taken into account.

In Figure 4.3(d), Fe^{3+}, the left graph shows the highest uncontrolled concentrations among the five species: 1800, 790, and 790 mol/m^2. In the optimized case, these become 90, 680, and 775 mol/m^2. The drop at r_1 is extremely large, from 1800 to 90, which indicates that the first segment is the dominant control point for iron under Case I. Meanwhile, r_2 and r_3 remain close to the uncontrolled values, which is consistent with much weaker reduction there. This result is plausible in the groundwater PDE setting because ferric iron is affected by both transport and hydrolysis/precipitation-type attenuation. If the optimizer identifies

that early upstream suppression at one key segment is enough to protect the observation region, then it becomes unnecessary to impose costly strong reductions everywhere. The enhanced pumping further supports this by intercepting the dissolved mass before it migrates farther downstream.

In Figure 4.3(e), Cl^-, the left graph shows 1485, 650, and 650 mol/m^2, while the optimized graph gives 210, 510, and 600 mol/m^2. The optimized reductions are visible but more moderate than for some reactive species. This is also physically correct. Chloride is typically conservative, so it does not benefit from reaction-based attenuation the way sulfate, calcium, or ferric iron may. Therefore, its concentration reduction depends mainly on direct source suppression and hydraulic removal. The drop at r_1 from 1485 to 210 shows that the optimizer identified the first segment as hydraulically influential, while the smaller changes at r_2 and r_3 indicate that moderate source control combined with pumping was sufficient to reduce plume impact without requiring extreme reductions at every segment.

Moreover, SO_4^{2-} in Figure 4.4 (a), under minimum reduction ($r = 10$) and low pumping ($Q = 2$), the concentrations remain relatively high both before and after the wells, indicating that neither source control nor hydraulic capture is sufficient to remove the plume effectively. In contrast, the optimized case shows a strong reduction after the wells, especially from 10 to 2 mol/m^2 at $y = 60$ and from 7 to 1.2 mol/m^2 at $y = 40$, which reflects the combined effect of strong upstream source reduction and increased pumping that enhances plume interception.

For Na^+ in Figure 4.4 (b), the minimum reduction and pumping case results in very high concentrations both upstream and downstream of the wells (e.g., 110 to 90 mol/m^2), demonstrating that conservative species are poorly controlled when both chemical and hydraulic mechanisms are weak. In the optimized case, although concentrations remain relatively high, they are significantly reduced after the wells, showing that increased pumping plays a major role in removing dissolved sodium that is not strongly affected by reactions.

For Ca^{2+} in Figure 4.4 (c), the minimum control case leads to only slight reduction after

the wells (e.g., 20 to 18 mol/m^2), indicating weak attenuation. In the optimized case, the after-well concentration decreases more noticeably (e.g., from 20 to 10 mol/m^2), reflecting the combined influence of stronger source reduction and enhanced hydraulic capture, along with geochemical interactions.

For Fe^{3+} in Figure 4.4 (d), the minimum reduction and pumping scenario produces high concentrations before and after the wells, showing limited plume control. Under optimal conditions, the concentrations decrease substantially after the wells (e.g., from 25 to 12 mol/m^2), which is consistent with both stronger source suppression and effective removal through pumping, as well as additional attenuation due to reactive processes.

For Cl^- in Figure 4.4 (e), the minimum control case yields large concentrations both upstream and downstream (e.g., 100 to 90 mol/m^2), confirming that weak pumping cannot effectively capture conservative ions. In the optimized case, the concentrations decrease significantly after the wells (e.g., from 80 to 42 mol/m^2), primarily due to increased pumping, since chloride does not benefit from reaction-based attenuation.

The distributions in Figure 4.3(a-e) and Figure 4.4(a-e) show that the optimized Case I solution is effective because it reduces contaminant loading in a segment-specific and species-specific way rather than uniformly. The increased pumping rates in Case I improve upstream plume interception, while the optimized reduction rates decrease the injected mass where it matters most. The numerical results are therefore both numerically reasonable and physically consistent with groundwater transport dynamics.

Chapter 5

Summery & Future work

This thesis developed efficient optimal control approaches for multicomponent contamination flows in porous media. In the second chapter of this thesis, we proposed a simulation-optimization model designed for managing groundwater contamination, with a primary focus on determining optimal injection rates. The utilization of splitting improved upwind scheme in numerical computation allowed the breakdown of a multi-dimensional convection-diffusion issue into one-dimensional problems, significantly expediting computation. The numerical results indicated that precipitation reactions reduce groundwater contamination. Furthermore, the numerical results provided us with quantified optimal injection and abatement rates. Analysis of the results leaded us to conclude that establishing factories downstream, as opposed to upstream, is more cost-effective and efficient. In the third chapter of this thesis, we focus on a robust and computationally powerful framework for the optimal control of multicomponent groundwater contamination. We dvelop a problem-specific parallel DE-PDE optimization system for multicomponent contamination control, the proposed approach bridges the gap between accurate physical modelling and practical decision-making for contamination control. The numerical experiments span multiple cost-function structures, hydraulic gradients, and injection configurations, which further confirm that the parallel DE–PDE solver for multicomponent contamination contour is capable of handling large-scale

optimization tasks with high computational efficiency, achieving substantial reductions in runtime without sacrificing solution accuracy. These capabilities position the framework as a robust and versatile tool for environmental management, capable of supporting real-world groundwater remediation planning under complex operational and regulatory constraints. In the fourth chapter of this thesis, we develop a multi-control optimization model for multicomponent groundwater contamination control. The concentration-matching term f_1 ensures that simulated contaminant levels closely follow prescribed targets, providing a baseline measure of environmental performance. However, numerical results show that using f_1 alone often leads to overly aggressive reduction strategies, resulting in high operational demands. The incorporation of the piecewise abatement cost term f_2' which significantly reduces excessive treatment effort by penalizing high reduction rates, leading to smoother and more economically feasible control strategies. Similarly, the inclusion of the pumping cost term f_3 reduces unnecessary extraction rates, thereby lowering energy consumption while maintaining acceptable concentration levels. Comparative results from the numerical experiments demonstrate that the combined objective $f_1 + f_2'$ produces balanced reduction strategies with moderate cost and acceptable accuracy, whereas $f_1 + f_3$ shifts the optimization toward efficient hydraulic control, often redistributing pumping locations and magnitudes. In the multi-control strategy, these objective function combinations noticeably alter the spatial distribution of contaminant plumes, indicating that cost terms influence not only magnitudes but also plume geometry. Furthermore, the full combination leads to more stable and realistic solutions, particularly in complex aquifer settings, where both treatment and pumping must be optimized simultaneously. Finally, the findings confirm that the structure of the linked-simulation optimization model has a significant impact on groundwater remediation strategies.

Despite the significant progress achieved in this thesis, managing groundwater contamination in real-world settings remains challenging due to complex geometries, heterogeneous aquifer

properties, and large spatial and temporal scales. In future work, we will extend the present two-dimensional model to a fully three-dimensional and multi-layer groundwater system. This extension will allow a more realistic representation of vertical transport, layer heterogeneity, and inter-layer exchange processes, which are important in practical aquifers. The model will incorporate different hydraulic properties across layers, such as permeability and porosity variations, to better describe stratified geological formations. We will also consider irregular domain geometries and more complex boundary conditions to reflect realistic field scenarios. In addition, we will develop efficient domain decomposition methods for solving large-scale multicomponent groundwater flow and transport equations. In this approach, the computational domain will be divided into multiple subdomains, and each subdomain will be solved independently in parallel. This will significantly reduce computational cost and memory requirements, especially for three-dimensional problems. The domain decomposition framework will be integrated with parallel optimization strategies, allowing simultaneous evaluation of multiple candidate solutions and improving the scalability of the overall simulation–optimization process. Another important direction is to incorporate more realistic and complex chemical reaction mechanisms into the model. This includes kinetically controlled reactions, multi-species interactions, and nonlinear reaction pathways that better represent geochemical processes in natural aquifers. The interaction between transport and reactions will be carefully modeled to maintain numerical stability and accuracy. We will also investigate adaptive numerical schemes to efficiently handle stiff reaction terms and highly nonlinear systems. Furthermore, we will extend the optimization framework to include source location identification. In this case, both the location and strength of contamination sources will be treated as unknown variables. This will transform the problem into a more challenging inverse optimization problem, where the model must simultaneously identify unknown sources and determine optimal control strategies. This extension will be particularly useful for real-world applications where contamination sources

are not clearly known. In addition, we will study more advanced and nonlinear pumping objective functions that account for realistic operational conditions. These may include energy-based cost models, time-dependent pumping schedules, and constraints related to infrastructure and environmental regulations. Nonlinear cost formulations will allow a more accurate representation of the trade-off between remediation efficiency and operational cost. Finally, we will explore the integration of all these components into a unified and scalable computational framework. The goal is to develop a robust, efficient, and practically applicable tool for groundwater contamination management that can handle large-scale, complex, and realistic problems.

Bibliography

[1] S. Afrifa, T. Zhang, P. Appiahene, and V. Varadarajan. Mathematical and machine learning models for groundwater level changes: a systematic review and bibliographic analysis. *Future Internet* 14 (9) (2022), 259.

[2] D.P. Ahlfeld and A.E. Mulligan. *Optimal management of flow in groundwater systems: an introduction to combining simulation models and optimization methods*. Academic Press, 2000.

[3] M.F. Ahmad, N.A.M. Isa, W.H. Lim, and K.M. Ang. Differential evolution: A recent review based on state-of-the-art works. *Alexandria Engineering Journal* 61 (5) (2022), 3831–3872.

[4] O. Al-Hashimi, K. Hashim, E. Loffill, T. Marolt Tina, I. Nakouti, A. Faisal, and N. Al-Ansari. A comprehensive review for groundwater contamination and remediation: occurrence, migration and adsorption modelling. *Molecules* 26 (19) (2021), 5913.

[5] E. Alba and M. Tomassini. Parallelism and evolutionary algorithms. *IEEE transactions on evolutionary computation* 6 (5) (2002), 443–462.

[6] A.C. Alexander and J.M. Ndambuki. Optimal design of groundwater pollution management systems for a decanting contaminated site: A simulation-optimization approach. *Groundwater for Sustainable Development* 15 (2021), 100664.

[7] W.M. Alley, L. Beutler, M.E. Campana, S.B. Megdal, and J.C. Tracy. Groundwater visibility: The missing link (2016).

[8] L.J. Alvarez-Vazquez, A. Martinez, R. Munoz-Sola, C. Rodriguez, and M.E. Vazquez-Mendez. Numerical optimization for the purification of polluted shallow waters. *Journal of computational and applied mathematics* 189 (1-2) (2006), 191–206.

[9] J. Ancheyta. *Chemical reaction kinetics: concepts, methods and case studies*. John Wiley & Sons, 2017.

[10] E. Augeraud-Véron, C. Choquet, and E. Comte. Optimal control for a groundwater pollution ruled by a convection–diffusion–reaction problem. *Journal of Optimization Theory and Applications* 173 (3) (2017), 941–966.

[11] J. Bear and A.H.D. Cheng. *Modeling groundwater flow and contaminant transport*. Vol. 23. Springer, 2010.

[12] A. Bermúdez, C. Rodríguez, M.E. Vázquez-Méndez, and A. Martínez. Mathematical modelling and optimal control methods in waste water discharges (2004), 3–15.

[13] I. Bortone, A. Erto, D.N. Armando, G.F. Santonastaso, S. Chianese, and D. Musmarra. Pump-and-treat configurations with vertical and horizontal wells to remediate an aquifer contaminated by hexavalent chromium. *Journal of Contaminant Hydrology* 235 (2020), 103725.

[14] J. Brest, S. Greiner, B. Boskovic, M. Mernik, and V. Zumer. Self-adapting control parameters in differential evolution: A comparative study on numerical benchmark problems. *IEEE transactions on evolutionary computation* 10 (6) (2006), 646–657.

[15] M.L. Brusseau and Z. Guo. Assessing contaminant-removal conditions and plume persistence through analysis of data from long-term pump-and-treat operations. *Journal of contaminant hydrology* 164 (2014), 16–24.

[16] G. Carrier, D. Destarac, A. Dumont, M. Meheut, E.D.I. Salah, J. Peter, K.S. Ben, J. Brezillon, and M. Pestana. Gradient-based aerodynamic optimization with the elsA software (2014), 0568.

[17] G. Cembrano, J. Quevedo, M. Salamero, V. Puig, J. Figueras, and J. Martı. Optimal control of urban drainage systems. A case study. *Control engineering practice* 12 (1) (2004), 1–9.

[18] G. Chandnani, P. Gandhi, D. Kanpariya, D. Parikh, and M. Shah. A comprehensive analysis of contaminated groundwater: Special emphasis on nature-ecosystem and socio-economic impacts. *Groundwater for Sustainable Development* 19 (2022), 100813.

[19] L.C. Chang, H.J. Chu, and C.T. Hsiao. Optimal planning of a dynamic pump-treat-inject groundwater remediation system. *Journal of Hydrology* 342 (3-4) (2007), 295–304.

[20] P.C. Chang, S.H. Chen, and K.L. Lin. Two-phase sub population genetic algorithm for parallel machine-scheduling problem. *Expert Systems with Applications* 29 (3) (2005), 705–712.

[21] S. Chowdhury, P.K. Das, and S.B. Faruque. *Numerical solutions of boundary value problems with finite difference method*. Morgan & Claypool Publishers, 2018.

[22] F.A. Coutelieris and J.M. Delgado. *Transport processes in porous media*. Vol. 20. Springer Science & Business Media, 2012.

[23] B. Datta, D. Chakrabarty, and A. Dhar. Identification of unknown groundwater pollution sources using classical optimization with linked simulation. *Journal of Hydro-Environment Research* 5 (1) (2011), 25–36.

[24] M. De Simoni, J. Carrera, X. Sanchez-Vila, and A. Guadagnini. A procedure for the solution of multicomponent reactive transport problems. *Water resources research* 41 (11) (2005).

[25] H.G. Diersch. *FEFLOW: finite element modeling of flow, mass and heat transport in porous and fractured media*. Springer Science & Business Media, 2013.

[26] M. Duan, H. Yang, S. Wang, and Y. Liu. Self-adaptive dual-strategy differential evolution algorithm. *Plos one* 14 (10) (2019), e0222706.

[27] A.S. Elshall, M. Ye, and M. Finkel. Evaluating two multi-model simulation–optimization approaches for managing groundwater contaminant plumes. *Journal of Hydrology* 590 (2020), 125427.

[28] Y. Fang, G.T. Yeh, and W.D. Burgos. A general paradigm to model reaction-based biogeochemical processes in batch systems. *Water Resources Research* 39 (4) (2003).

[29] R.C Feiock and C. Stream. Environmental protection versus economic development: A false trade-off? *Public administration review* 61 (3) (2001), 313–321.

[30] R.M. Felder, R.W. Rousseau, and L.G. Bullard. *Elementary principles of chemical processes*. John Wiley & Sons, 2020.

[31] G. Ferguson, M.O. Cuthbert, K. Befus, T. Gleeson, and J.C. McIntosh. Rethinking groundwater age. *Nature Geoscience* 13 (9) (2020), 592–594.

[32] C.R. Fitts. *Groundwater science*. Elsevier, 2002.

[33] G.C. Fox, R.D. Williams, and G..C Messina. *Parallel computing works!* Elsevier, 2014.

[34] T. Gleeson, K.M. Befus, S. Jasechko, E. Luijendijk, and M.B. Cardenas. The global volume and distribution of modern groundwater. *Nature geoscience* 9 (2) (2016), 161–167.

[35] G.H. Golub and J.M. Ortega. *Scientific computing: an introduction with parallel computing*. Elsevier, 2014.

[36] W. Gong, Z. Cai, C.X. Ling, and H. Li. Enhanced differential evolution with adaptive strategies for numerical optimization. *IEEE Transactions on Systems, Man, and Cybernetics, Part B (Cybernetics)* 41 (2) (2010), 397–413.

[37] S.M. Gorelick and C. Zheng. Global change and the groundwater management challenge. *Water Resources Research* 51 (5) (2015), 3031–3051.

[38] T. Graf and R. Therrien. Variable-density groundwater flow and solute transport in porous media containing nonuniform discrete fractures. *Advances in water resources* 28 (12) (2005), 1351–1367.

[39] T.V. Ha, Q.H. Nguyen, and T.T. Nguyen. A parallel differential evolution with cooperative multi-search strategy for sizing truss optimization. *Applied Soft Computing* 131 (2022), 109762.

[40] M. Hayek, G. Kosakowski, A. Jakob, and S.V. Churakov. A class of analytical solutions for multidimensional multispecies diffusive transport coupled with precipitation-dissolution reactions and porosity changes. *Water Resources Research* 48 (3) (2012).

[41] L. He, G.H. Huang, and H.W. Lu. A stochastic optimization model under modeling uncertainty and parameter certainty for groundwater remediation design—Part I. Model development. *Journal of Hazardous Materials* 176 (1-3) (2010), 521–526.

[42] Y.C. He and X.Z. Wang. Solution of hard constrained optimization problem based on modified differential evolution algorithm. *Computer Engineering* 34 (2008), 193–217.

[43] T.H. Henderson, K.U. Mayer, B.L. Parker, and T.A. Al. Three-dimensional density-dependent flow and multicomponent reactive transport modeling of chlorinated solvent oxidation by potassium permanganate. *Journal of contaminant hydrology* 106 (3-4) (2009), 195–211.

[44] D.M. Himmelblau and J.B. Riggs. *Basic principles and calculations in chemical engineering*. FT press, 2012.

[45] K.E. Hossain, D. Liang, and H. Zhu. Developing PDE-constrained optimal control of multicomponent contamination flows in porous media. *Computers & Mathematics with Applications* 176 (2024), 224–243.

[46] S.M. Hosseini, T. Tosco, B. Ataie-Ashtiani, and C.T. Simmons. Non-pumping reactive wells filled with mixing nano and micro zero-valent iron for nitrate removal from groundwater: Vertical, horizontal, and slanted wells. *Journal of contaminant hydrology* 210 (2018), 50–64.

[47] O. Hrstka and A. Kuvcerova. Improvements of real coded genetic algorithms based on differential operators preventing premature convergence. *Advances in Engineering software* 35 (3-4) (2004), 237–246.

[48] A. Hussen. *Principles of environmental economics and sustainability: an integrated economic and ecological approach*. Routledge, 2012.

[49] D.B. Ingham and I. Pop. *Transport phenomena in porous media III*. Vol. 3. Elsevier, 2005.

[50] J.F. Kanney, C.T. Miller, and D.A. Barry. Comparison of fully coupled approaches for approximating nonlinear transport and reaction problems. *Advances in Water Resources* 26 (4) (2003), 353–372.

[51] C.Y. Kao, S.L. Hung, and B. Setiawan. Two strategies to improve the differential evolution algorithm for optimizing design of truss structures. *Advances in Civil Engineering* 2020 (1) (2020), 8741862.

[52] M.J. Kazemzadeh-Parsi, F. Daneshmand, M.A. Ahmadfard, J. Adamowski, and R. Martel. Optimal groundwater remediation design of pump and treat systems via a simulation–optimization approach and firefly algorithm. *Engineering Optimization* 47 (1) (2015), 1–17.

[53] A.K. Keshari and B. Datta. A combined use of direct search algorithms and exterior penalty function method for groundwater pollution management. *Journal of Porous Media* 4 (3) (2001).

[54] N.Y. Ko, K.K. Lee, and Y. Hyun. Optimal groundwater remediation design of a pump and treat system considering clean-up time. *Geosciences Journal* 9 (1) (2005), 23–31.

[55] Y. N Kontos. A Simulation–Optimization Model for Optimal Aquifer Remediation, Using Genetic Algorithms and MODFLOW. *Hydrology* 11 (5) (2024), 60.

[56] K. Kozlov and A. Samsonov. DEEP—differential evolution entirely parallel method for gene regulatory networks. *The Journal of supercomputing* 57 (2) (2011), 172–178.

[57] J. Lampinen. *A constraint handling approach for the differential evolution algorithm*. Vol. 2. IEEE, 2002, pp. 1468–1473.

[58] R.J. Lazarov, I.D. Mishev, and P.S. Vassilevski. Finite volume methods for convection-diffusion problems. *SIAM Journal on Numerical Analysis* 33 (1) (1996), 31–55.

[59] R. J. Lezeque. *Finite difference methods for ordinary and partial differential equations: steady-state and time-dependent problems*. SIAM, 2007.

[60] J. Li, C. Sun, W. Chen, Q. Zhang, S. Zhou, R. Lin, and Y. Wang. Groundwater quality and associated human health risk in a typical basin of the Eastern Chinese Loess Plateau. *Water* 11 (14) (2022), 1371.

[61] P. Li, D. Karunanidhi, T. Subramani, and K. Srinivasamoorthy. Sources and consequences of groundwater contamination. *Archives of environmental contamination and toxicology* 80 (1) (2021), 1–10.

[62] T. Li, Y. Li, F. Wang, C. Gong, J. Zhang, and H. Ma. Improved parallel differential evolution algorithm with small population for multi-period optimal dispatch problem of microgrids. *Energies* 18 (14) (2025), 3852.

[63] Y.P. Li, G.H. Huang, S.L. Nie, and D.W. Mo. Interval-parameter robust quadratic programming for water quality management under uncertainty. *Engineering Optimization* 40 (7) (2008), 613–635.

[64] Z. Li, Z. Qiao, and T. Tang. *Numerical solution of differential equations: introduction to finite difference and finite element methods*. Cambridge University Press, 2017.

[65] D. Liang and Z. Zhou. The conservative splitting domain decomposition method for multicomponent contamination flows in porous media. *Journal of Computational Physics* 400 (2020), 108974.

[66] G. Liu, Y. Li, X. Nie, and H. Zheng. A novel clustering-based differential evolution with 2 multi-parent crossovers for global optimization. *Applied Soft Computing* 12 (2) (2012), 663–681.

[67] J. Liu. On setting the control parameter of the differential evolution method (2002), 11–18.

[68] M. Liu, G. Nie, M. Hu, R. Liao, and Y. Shen. An interval-parameter fuzzy robust nonlinear programming model for water quality management. *Journal of Water Resource and Protection* 5 (01) (2013), 12–16.

[69] B. Lu, S. Huang, and I.E. Grossmann. Optimal synthesis and operation of wastewater treatment process with dynamic influent. *Industrial & Engineering Chemistry Research* 56 (30) (2017), 8663–8676.

[70] G. Luque and E. Alba. *Parallel genetic algorithms: Theory and real world applications*. Vol. 367. Springer, 2011.

[71] R. Mallipeddi, P.N. Suganthan, Q. Pan, and M.F. Tasgetiren. Differential evolution algorithm with ensemble of parameters and mutation strategies. *Applied soft computing* 11 (2) (2011), 1679–1696.

[72] X. Mao, H.B. Prommer, C.D. Langevin, B. Panteleit, and L. Li. Three-dimensional model for multi-component reactive transport with variable density groundwater flow. *Environmental Modelling & Software* 21 (5) (2006), 615–628.

[73] A. Martinez, C. Rodriguez, and M.E. Vazquez-Mandez. Theoretical and numerical analysis of an optimal control problem related to wastewater treatment. *SIAM Journal on Control and Optimization* 38 (5) (2000), 1534–1553.

[74] D.E. Matthieu III, M.L. Brusseau, Z. Guo, M. Plaschke, K.C. Carroll, and F. Brinker. Persistence of a groundwater contaminant plume after hydraulic source containment at a chlorinated-solvent contaminated site. *Groundwater Monitoring & Remediation* 34 (4) (2014), 23–32.

[75] K.U. Mayer, E.O. Frind, and D.W. Blowes. Multicomponent reactive transport modeling in variably saturated porous media using a generalized formulation for kinetically controlled reactions. *Water Resources Research* 38 (9) (2002), 13–1.

[76] S. Molins, D. Svyatsky, Z. Xu, E.T. Coon, and J.D. Moulton. A multicomponent reactive transport model for integrated surface-subsurface hydrology problems. *Water Resources Research* 58 (8) (2022), e2022WR032074.

[77] A. Mondal, T.I. Eldho, and V.G. Rao. Multiobjective groundwater remediation system design using coupled finite-element model and nondominated sorting genetic algorithm II. *Journal of Hydrologic Engineering* 15 (5) (2010), 350–359.

[78] M.I.C. Morakaladi and A. Atangana. Mathematical model for conversion of groundwater flow from confined to unconfined aquifers with power law processes. *Open Geosciences* 15 (1) (2023), 20220446.

[79] M. Muniruzzaman and M. Rolle. Modeling multicomponent ionic transport in groundwater with IPhreeqc coupling: Electrostatic interactions and geochemical reactions in homogeneous and heterogeneous domains. *Advances in Water Resources* 98 (2016), 1–15.

[80] J.S. Mustafa and D.K. Mawlood. Mathematical modelling for groundwater management for multilayers aquifers (Erbil basin). *Ain Shams Engineering Journal* 15 (7) (2024), 102781.

[81] S. Orr and A.M. Meystel. Approaches to optimal aquifer management and intelligent control in a multiresolutional decision support system. *Hydrogeology Journal* 13 (1) (2005), 223–246.

[82] Z.B. Pan, L. Yang, Z.X. Xu, and D.Y. Wang. A NEC-based parallel differential evolution algorithm with MKL/CUDA. *J. Netw. Intell* 7 (2022), 114–128.

[83] Y.C. Park. Cost-effective optimal design of a pump-and-treat system for remediating groundwater contaminant at an industrial complex. *Geosciences Journal* 20 (6) (2016), 891–901.

[84] Y.C. Park, J.M. Jeong, S. Eom, and U.P. Jeong. Optimal management design of a pump and treat system at the industrial complex in Wonju, Korea. *Geosciences J.* 15 (2) (2011), 207–223.

[85] S. Paul, B. Waldron, F. Jazaei, D. Larsen, and S. Schoefernacker. Groundwater well optimization to minimize contaminant movement from a surficial shallow aquifer to a lower water supply aquifer using stochastic simulation-optimization modeling techniques: Strategy formulation. *MethodsX* 9 (2022), 101765.

[86] D.R. Penas, J.R. Banga, P. Gonzalez, and R. Doallo. Enhanced parallel differential evolution algorithm for problems in computational systems biology. *Applied Soft Computing* 33 (2015), 86–99.

[87] J.L. Plawsky. *Transport phenomena fundamentals*. CRC press, 2020.

[88] K.V. Price, R.M. Storn, and J.A. Lampinen. *Differential evolution: a practical approach to global optimization*. Springer, 2005.

[89] H. Prommer, D.A. Barry, and C. Zheng. MODFLOW/MT3DMS-based reactive multicomponent transport modeling. *Groundwater* 41 (2) (2003), 247–257.

[90] X.S. Qin and G.H. Huang. An inexact chance-constrained quadratic programming model for stream water quality management. *Water resources management* 23 (4) (2009), 661–695.

[91] P.A. Ramachandran. *Mass transfer processes: modeling, computations, and design*. Prentice Hall, 2018.

[92] J.C. Refsgaard, A.L. Hojberg, I. Moller, M. Hansen, and V. Sondergaard. Groundwater modeling in integrated water resources management—Visions for 2020. *Groundwater* 48 (5) (2010), 633–648.

[93] N. Sakovich, D. Aksenov, E. Pleshakova, and S. Gataullin. MAMGD: Gradient-based optimization method using exponential decay. *Technologies* 12 (9) (2024), 154.

[94] X. Sanchez-Vila, L.D. Donado, A. Guadagnini, and J. Carrera. A solution for multicomponent reactive transport under equilibrium and kinetic reactions. *Water Resources Research* 46 (7) (2010).

[95] M.A. Sbai. Well rate and placement for optimal groundwater remediation design with a surrogate model. *Water* 11 (11) (2019), 2233.

[96] S.M.V. Sharief, T.I. Eldho, A.K. Rastogi, and V.V.S. Gurunadha Rao. Optimal groundwater remediation by pump and treat using FEM-and EGA-based simulation-optimization model. *Journal of Hazardous, Toxic, and Radioactive Waste* 16 (2) (2012), 106–117.

[97] R. Storn and K. Price. Differential evolution–a simple and efficient heuristic for global optimization over continuous spaces. *Journal of global optimization* 11 (4) (1997), 341–359.

[98] J.C. Strikwerda. *Finite difference schemes and partial differential equations*. SIAM, 2004.

[99] X. Sui, S.C. Chu, J.S. Pan, and H. Luo. Parallel compact differential evolution for optimization applied to image segmentation. *Applied Sciences* 10 (6) (2020), 2195.

[100] R. Tanabe and A. Fukunaga. Success-history based parameter adaptation for differential evolution (2013), 71–78.

[101] D.K. Tasoulis, N.G. Pavlidis, V.P. Plagianakos, and M.N. Vrahatis. Parallel differential evolution. (2004), 2023–2029.

[102] A.K. Thakur, M. Vithanage, D.B. Das, and M. Kumar. A review on design, material selection, mechanism, and modelling of permeable reactive barrier for community-scale groundwater treatment. *Environmental Technology & Innovation* 19 (2020), 100917.

[103] K. Vafai. *Handbook of porous media*. Crc Press, 2015.

[104] D.V. Vargas, J. Murata, H. Takano, and A.C.B. Delbem. General subpopulation framework and taming the conflict inside populations. *Evolutionary computation* 23 (1) (2015), 1–36.

[105] J. Verrett, R. Qiao, R.A. Barghout, and B. Vancouver. Foundations of Chemical and Biological Engineering I. *BCcampus, Vancouver* (2020).

[106] J. Vesterstrom and R. Thomsen. A comparative study of differential evolution, particle swarm optimization, and evolutionary algorithms on numerical benchmark problems. 2 (2004), 1980–1987.

[107] T. Vivekanandan and S.N. Iyengar. Optimal feature selection using a modified differential evolution algorithm and its effectiveness for prediction of heart disease. *Computers in biology and medicine* 90 (2017), 125–136.

[108] M.N. Vrahatis, G.S. Androulakis, J.N. Lambrinos, and G.D. Magoulas. A class of gradient unconstrained minimization algorithms with adaptive stepsize. *Journal of Computational and Applied Mathematics* 114 (2) (2000), 367–386.

[109] A.L. Walter, E.O. Frind, D.W. Blowes, C.J. Ptacek, and J.W. Molson. Modeling of multicomponent reactive transport in groundwater: 1. Model development and evaluation. *Water resources research* 30 (11) (1994), 3137–3148.

[110] B.C. Wang, H.X. Li, J.P. Li, and Y. Wang. Composite differential evolution for constrained evolutionary optimization. *IEEE Transactions on Systems, Man, and Cybernetics: Systems* 49 (7) (2018), 1482–1495.

[111] D. Wang, P. Li, Y. Ji, and X. Ren. Insight into the impact of biogeochemical reactions of groundwater nitrogen on chemical weathering and carbon cycling. *Journal of Hydrology* 648 (2025), 132458.

[112] M. Wijnen, B. Augeard, B. Hiller, C. Ward, and P. Huntjens. Managing the invisible: Understanding and improving groundwater governance (2012).

[113] C.B. Winn and J.B. Moore. The application of optimal linear regulator theory to a problem in water pollution. *IEEE Transactions on Systems, Man, and Cybernetics* (5) (2007), 450–455.

[114] M. Xie, K.U. Mayer, F. Claret, P. Alt-Epping, D. Jacques, C. Steefel, C. Chiaberge, and J. Simunek. Implementation and evaluation of permeability-porosity and tortuosity-porosity relationships linked to mineral dissolution-precipitation. *Computational geosciences* 19 (3) (2015), 655–671.

[115] Q. Xu and Z. Meng. Differential Evolution with multi-stage parameter adaptation and diversity enhancement mechanism for numerical optimization. *Swarm and Evolutionary Computation* 92 (2025), 101829.

[116] Y. Yu, B. Yan, Y. Tuo, X. Zhan, and X. Xie. Chemical evolution characteristics and influencing factors of groundwater in the saline and fresh water funnel area in Hengshui City, North China. *Scientific Reports* 15 (1) (2025), 3276.

[117] Y. Yuan and D. Liang. Optimization of identifying point pollution sources for the convection-diffusion-reaction equations. *Advances in Applied Mathematics and Mechanics* 13 (1) (2021), 1–17.

[118] Y. Yuan, D. Liang, and H. Zhu. Optimal control of groundwater pollution combined with source abatement costs and taxes. *Journal of Computational Science* 20 (2017), 17–29.

[119] M.J. Zeynali, M.N. Tahroudi, and O. Mohammadrezapour. Optimizing Pump-and-Treat method by using optimization-simulation models. *Sustainable Earth Trends* 4 (3) (2024).

[120] Q. Zhang, X. Yang, Y. Zhang, and M. Zhong. Risk assessment of groundwater contamination: a multilevel fuzzy comprehensive evaluation approach based on DRASTIC model. *The Scientific World Journal* 2013 (1) (2013), 610390.

[121] C. Zheng and P.P. Wang. A field demonstration of the simulation optimization approach for remediation system design. *Groundwater* 40 (3) (2002), 258–266.

[122] X.G. Zhou, G.J. Zhang, X.H. Hao, L. Yu, and D.W. Xu. Differential evolution with multi-stage strategies for global optimization (2016), 2550–2557.

[123] Z. Zhou and D. Liang. The mass-preserving and modified-upwind splitting DDM scheme for time-dependent convection–diffusion equations. *Journal of Computational and Applied Mathematics* 317 (2017), 247–273.

[124] H. Zhu, G.H. Huang, P. Guo, and X.S. Qin. A fuzzy robust nonlinear programming model for stream water quality management. *Water Resources Management* 23 (14) (2009), 2913–2940.

[125] L. Zhu, G. Yuan, and Q. Du. An efficient explicit/implicit domain decomposition method for convection-diffusion equations. *Numerical Methods for Partial Differential Equations* 26 (4) (2010), 852–873.

[126] D.W. Zingg, M. Nemec, and T.H. Pulliam. A comparative evaluation of genetic and gradient-based algorithms applied to aerodynamic optimization. *European Journal of Computational Mechanics/Revue Europ* 17 (1-2) (2008), 103–126.

[127] D. Zou, H. Liu, L. Gao, and S. Li. A novel modified differential evolution algorithm for constrained optimization problems. *Computers & mathematics with applications* 61 (6) (2011), 1608–1623.